



Nouvelles Topologies des diviseurs de puissance, balun et déphaseurs en bandes RF et millimétriques, apport des lignes à ondes lentes

François Burdin

► To cite this version:

François Burdin. Nouvelles Topologies des diviseurs de puissance, balun et déphaseurs en bandes RF et millimétriques, apport des lignes à ondes lentes. Autre. Université de Grenoble, 2013. Français. NNT : 2013GRENT018 . tel-00903675

HAL Id: tel-00903675

<https://theses.hal.science/tel-00903675>

Submitted on 12 Nov 2013

HAL is a multi-disciplinary open access archive for the deposit and dissemination of scientific research documents, whether they are published or not. The documents may come from teaching and research institutions in France or abroad, or from public or private research centers.

L'archive ouverte pluridisciplinaire **HAL**, est destinée au dépôt et à la diffusion de documents scientifiques de niveau recherche, publiés ou non, émanant des établissements d'enseignement et de recherche français ou étrangers, des laboratoires publics ou privés.

THÈSE

Pour obtenir le grade de

DOCTEUR DE L'UNIVERSITÉ DE GRENOBLE

Spécialité : **Nano-Électronique et Nano-Technologies**

Arrêté ministériel : 7 août 2006

Présentée par

François BURDIN

Thèse dirigée par **Philippe FERRARI**
et codirigée par **Florence PODEVIN**

préparée au sein du **Laboratoire IMEP-LAHC**
dans l'**École Doctorale Électronique, Électrotechnique,**
Automatique et Traitement du Signal

Nouvelles topologies de diviseurs de puissance, baluns et déphaseurs en bandes RF et millimétriques, apport des lignes à ondes lentes

Thèse soutenue publiquement le **16 Juillet 2013**,
devant le jury composé de :

M. Christophe GAQUIERE

Professeur des universités, Lille, Président

M. Roberto SORRENTINO

Professeur des universités, Pérouse (Italie), Rapporteur

M. Eric KERHERVE

Professeur des universités, Bordeaux, Rapporteur

M. Daniel GLORIA

Ingénieur STMicroelectronics, Crolles, Membre

M. Tibor BERCELI

Professeur des universités, Budapest (Hongrie), Invité

M. Philippe FERRARI

Professeur des universités, Grenoble, Directeur de thèse

Mme. Florence PODEVIN

Maître de conférences, Grenoble, Co-encadrant de thèse



Résumé

L'objectif de cette thèse a été premièrement de réaliser des dispositifs passifs intégrés à base de lignes à onde lentes nommées S-CPW (pour « Slow-wave CoPlanar Waveguide ») aux fréquences millimétriques. Plusieurs technologies CMOS ou BiCMOS ont été utilisées: CMOS 65 nm et 28 nm ainsi que BiCMOS 55 nm.

Deux baluns, le premier basé sur une topologie de rat-race et le second basé sur un diviseur de puissance de Wilkinson modifié, ainsi qu'un inverseur de phase, ont été réalisés et mesurés dans la technologie CMOS 65 nm. Les résultats expérimentaux obtenus se situent à l'état de l'art en termes de performances électriques. Un coupler hybride et un diviseur de puissance avec des sorties en phase sans isolation ont été conçus en technologie CMOS 28 nm. Les simulations montrent de très bonnes performances pour des dispositifs compacts. Les circuits sont en cours de fabrication et pourront très bientôt être caractérisés. Ensuite, une nouvelle topologie de diviseurs de puissance, avec sorties en phase et isolé a été développée, offrant une grande flexibilité et compacité en comparaison des diviseurs de puissance traditionnels. Cette topologie est parfaitement adaptée pour les technologies silicium. Comme preuve de concept, deux diviseurs de puissance avec des caractéristiques différentes ont été réalisés en technologie PCB microruban à la fréquence de 2.45 GHz. Un composant a été conçu à 60 GHz en technologie BiCMOS 55 nm utilisant des lignes S-CPW. Les simulations prouvent que le dispositif est faibles pertes, adapté et isolé. Les circuits sont également en cours de fabrication. Enfin, deux topologies de « reflection type phase shifter » ont été développées, la première dans la bande RF et la seconde aux fréquences millimétrique. Pour la bande RF, le déphasage atteint plus de 360° avec une figure de mérite très élevée en comparaison avec l'état de l'art. En ce qui concerne le déphaseur dans la bande millimétrique, la simulation montre un déphasage de 341° avec également une figure de mérite élevée.

Mots-clés : Ligne à ondes lentes S-CPW, facteur de qualité, technologies CMOS, balun, rat-race, inverseur de phase, diviseur de puissance, coupleur hybride, déphaseur, bande millimétrique, bande RF, figure de mérite, miniaturisation.

Title

New topologies of power dividers, baluns and phase shifters in RF and millimetre-wave bands, based on microstrip lines and slow-wave coplanar waveguides technologies.

Abstract

The first purpose of this work was the use of slow-wave coplanar waveguides (S-CPW) to achieve various passive components with the aim to show their great potential and interest at millimetre-waves. Several CMOS or BiCMOS technologies were used: CMOS 65 nm and 28 nm, and BiCMOS 55 nm.

Two baluns, one based on a rat-race topology and the other based on a modified Wilkinson power divider, and a phase inverter, were achieved and measured in a 65 nm CMOS technology. State-of-the-art results were achieved. A branch-line coupler and an in phase power divider without isolation were designed in a 28 nm CMOS technology. Really good performances are expected for these compact devices being yet under fabrication. Then, a new topology of in phase and isolated power divider was developed, leading to more flexibility and compactness, well suited to millimetre-wave frequencies. Two power dividers with different characteristics were realized in a PCB technology at 2.45 GHz by using microstrip lines, as a proof-of-concept. After that, a power divider was designed at the working frequency of 60 GHz in the 55 nm BiCMOS technology with S-CPWs. The simulation results showed a low loss, full-matched and isolated component, which is also under fabrication and will be characterized as soon as possible. Finally, two new topologies of reflection type phase shifters were presented, one for the RF band and one for the millimetre-wave one. For the one in RF band, the phase shift can reach more than 360° with a great figure-of-merit as compared to the state-of-the-art. Concerning the phase shifter in the millimetre-wave band, the simulation results show a phase shift of 341° with also a high figure-of-merit.

Key words : Slow-wave CPW, quality factor, CMOS technologies, balun, rat-race, phase inverter, power divider, branch-line coupler, reflection type phase shifter, millimetre-wave band, RF band, figure-of-merit, miniaturization.

Remerciements

Je souhaite tout d'abord remercier Monsieur Christophe Gaquière, professeur à l'université de Lille, qui me fait l'honneur de présider le jury, ainsi que Messieurs Eric Kerhervé, professeur à l'université de Bordeaux et Roberto Sorrentino, professeur à l'université de Pérouse pour avoir accepté d'être rapporteurs de cette thèse.

Merci à Daniel GLORIA qui a accepté d'être examinateur au cours de la soutenance ainsi que pour la mise à disposition en toute confiance des technologies de STMicroelectronics. Sa collaboration a été essentielle pour mon travail de thèse. Un grand merci au Professeur Tibor BERCELI de l'université de Budapest, qui m'a fait l'honneur d'assister à cette thèse. Budapest... cette ville qui représente tant de choses pour moi.

Ma rencontre avec Philippe FERRARI à l'IUT en 2006 allait sans le savoir être déterminante pour ma carrière. Après m'avoir accepté en stage à l'IMEP-LAHC lors de ma deuxième année à l'ENSERG en 2009, une année après Philippe m'a très gentiment proposé cette thèse. Ses qualités professionnelles, sa pédagogie et son optimisme ont fait que l'idée de travailler avec lui a été le facteur dominant pour accepter ce projet. Florence PODEVIN a parfaitement complété mon encadrement, avec sa gentillesse et sa générosité. Malgré ses contraintes, Florence a toujours été disponible et m'a toujours aidé pour avancer au mieux dans mon travail. Philippe et Florence m'ont toujours fait confiance, j'avais donc une réelle volonté de ne pas les décevoir. Cette confiance était pour moi une source de motivation aussi importante que la réussite de ma thèse. Je pense avoir eu des encadrants exceptionnels, ceux que tout thésard rêve d'avoir, et j'en ai conscience. C'est pour cela que je leurs en suis extrêmement reconnaissant. Merci Philippe. Merci Florence.

Je suis également reconnaissant à Nicolas CORRAO pour les mesures des dispositifs intégrés et s'être déplacé à Chambéry avec moi, à Benjamin BLAMPEY pour toute la partie de-embedding, à Alejandro NIEMBRO pour la réalisation et mesure des antennes et à Alexandre CHAGOYA pour son aide sur les design Kits. Il y a aussi ceux que j'ai côtoyés ou avec lesquels j'ai travaillé pendant ces trois années, merci à Anne-Laure, Xiaolan, Jean-Michel, Estelle, Jean-Daniel, Farid, José, Pierre et bien sûr Manu le chambreur numéro un... Toutes ces personnes m'ont apporté bien plus qu'elles ne le pensent et je les remercie. Je pense également à Ziad, mon premier et unique stagiaire, toujours souriant et amical, qui a donc accepté d'être mon cobaye, à son insu... Je pense que nous avons fait une belle équipe et lui souhaite plein de bonheur pour la suite.

Un grand merci à tous les doctorants qui se sont succédés au bureau A440. J'ai pu y rencontrer Fabien, Zine, Florent et bien sûr Inès et Alex qui ont apportés une dimension

internationale très agréable. Une grande complicité s'était installée entre nous et c'est avec regret que je les quitte. Merci à notre voisin de bureau, Tan-Phu, qui pensait toujours à nous pour partager ses friandises.

Il m'est impossible de ne pas citer mes amis de l'ERG avec qui j'ai passé mes trois plus belles années d'études. Je pense à Armand, Nico, Tyty, Ousmane et Polo, notre groupe des admis sur titre, mais aussi à Minot, Youyou (dit « Binôme ») et Richard Président. Merci pour votre aide, pour toutes ces soirées, ces sorties, ces foots... et je m'excuse de n'avoir pu passer plus de temps avec vous ces trois dernières années. Il y a eu bien sûr cette coloc Magic, avec les Trois Mousquetaires, période qui restera inoubliable.

Il y a aussi des gens que j'ai rencontrés et qui sont devenus plus que des amis. Je tiens à remercier Vlad, avec qui j'ai passé tant de temps. C'était toujours un plaisir de faire du design pour me trouver dans la même salle que lui. Merci aussi à Francesco et Paolo, à leur année à l'IMEP-LAHC qui est passée beaucoup trop vite. Notre périple en Italie, les Châteaux de la Loire avec Ana et toutes ces sorties ensemble... que de souvenirs.

Un très grand merci à mes parents qui ont toujours acceptés mes choix, m'ont soutenus et m'ont fait confiance. Je n'oublie pas mon frère Nico à qui je souhaite la réussite et tout le bonheur du monde.

Enfin, je remercie la personne qui a partagé avec moi cette aventure et qui a toujours été à mes côtés depuis trois ans et demi. Merci Elena, pour ta gentillesse et ta compréhension, je ne te remercierai jamais assez pour les sacrifices que tu as faits en me suivant en France. Un grand merci à ta famille qui m'accueille toujours comme un Tsar lors de nos visites à Saint Pétersbourg.

TABLE OF CONTENTS

INTRODUCTION.....	13
CHAPTER I : POWER DIVIDERS/COMBINERS AND REFLECTION	
TYPE PHASE SHIFTER PRESENTATION.....	17
I.1 PLANAR DIVIDERS/COMBINERS	17
I.1.1 Overview.....	18
I.1.2 Wilkinson power divider/combiner.....	18
<i>I.1.2.1 Presentation.....</i>	<i>18</i>
<i>I.1.2.2 Evolution</i>	<i>19</i>
<i>I.1.2.3 Striking applications.....</i>	<i>20</i>
I.1.3 Branch-line coupler	21
<i>I.1.3.1 Presentation.....</i>	<i>21</i>
<i>I.1.3.2 Evolution</i>	<i>22</i>
<i>I.1.3.3 Striking applications.....</i>	<i>23</i>
I.1.4 Rat race coupler.....	24
<i>I.1.4.1 Presentation.....</i>	<i>24</i>
<i>I.1.4.2 Evolution</i>	<i>25</i>
<i>I.1.4.3 Application</i>	<i>26</i>
I.2 REFLECTION TYPE PHASE SHIFTER	27
I.2.1 Principle and theory	27
<i>I.2.1.1 Insertion loss</i>	<i>27</i>
<i>I.2.1.2 Relative phase shift.....</i>	<i>28</i>
<i>I.2.1.3 Practical example with non-ideal varactor</i>	<i>29</i>
<i>I.2.1.4 Conclusion.....</i>	<i>30</i>
I.2.2 Modified reflective load.....	30
<i>I.2.2.1 Serial inductance.....</i>	<i>30</i>
<i>I.2.2.2 State-of-the-art at RF frequencies</i>	<i>31</i>
I.2.3 Branch-line coupler substitution	34
I.2.4 Applications.....	35
I.2.5 State-of-the-art review	35
I.3 MINIATURIZATION TECHNIQUES	36
I.3.1 Shunt-stub-based artificial transmission lines	36
I.3.2 Meander and Fractals	37
I.3.3 Phase inverter	37

I.3.4 Capacitor loading	38
I.3.5 Stepped-impedance	38
I.3.6 Slow-wave transmissions lines.....	38
I.4 STATE-OF-THE-ART IN MILLIMETRE-WAVES	41
I.4.1 Power divider with in phase outputs.....	41
I.4.2 Power divider with quadrature outputs	42
I.4.3 Power divider with out-of-phase outputs	43
I.4.4 Phase shifter	44
I.5 CONCLUSION	45
CHAPTER II : S-CPW APPLICATIONS.....	47
II.1 SIMULATION TOOL.....	47
II.2 CALIBRATION & DE-EMBEDDING.....	48
II.2.1 Two port devices	48
<i>II.2.1.1 Transmission Line.....</i>	<i>48</i>
<i>II.2.1.2 Devices.....</i>	<i>49</i>
II.2.2 Four port devices	50
II.3 STACKS	54
II.4 SIMULATED AND MEASURED TRANSMISSIONS LINES.....	54
II.4.1 Study of the quality factor of the S-CPW in the 65 nm CMOS technology	55
II.4.2 Transmission lines in the 65 nm CMOS technology: measurement versus simulation results.....	57
<i>II.4.2.1 Microstrip</i>	<i>57</i>
<i>II.4.2.2 S-CPW</i>	<i>58</i>
<i>II.4.2.3 Results synthesis</i>	<i>59</i>
II.4.3 Transmission lines in the 28 nm CMOS technology: simulation results.....	59
II.4.4 Transmission lines in the 55 nm BiCMOS technology: simulation results	60
II.5 PHASE INVERTER.....	61
II.6 BALUNS	62
II.6.1 Rat-race coupler balun	62
<i>II.6.1.1 Design and layout</i>	<i>63</i>
<i>II.6.1.2 Simulation versus measurement results</i>	<i>64</i>
<i>II.6.1.3 Further improvements.....</i>	<i>66</i>
II.6.2 Power divider balun.....	66

II.6.2.1 Simulation versus measurement results.....	67
II.6.2.2 Further improvements.....	68
II.6.3 Comparison with the state-of-the-art	68
II.7 BRANCH-LINE COUPLER.....	69
II.8 POWER DIVIDER.....	70
II.9 CONCLUSION	72
CHAPTER III : NEW TYPE OF POWER DIVIDER BASED ON A WILKINSON POWER DIVIDER/COMBINER FOR MILLIMETRE-WAVE FREQUENCIES APPLICATIONS.....	74
III.1 ISSUES FOR WILKINSON POWER DIVIDERS IN SILICON TECHNOLOGY	75
III.1.1 Isolation resistance	75
III.1.2 Characteristic impedance flexibility	75
III.1.3 State-of-the-art of the solutions.....	76
III.2 STUDY OF A NEW SOLUTION	77
III.2.1 Topology presentation.....	77
III.2.2 Theory and design equations	77
III.2.2.1 Even-mode analysis	78
III.2.2.2 Odd-mode analysis	80
III.2.3 Design procedure	81
III.2.3.1 Demonstration of the good matching and isolation according to the value of S_{22}	82
III.2.3.2 Procedure for finding solutions	85
III.3 CIRCUITS DESIGN AND EXPERIMENTAL RESULTS	87
III.3.1 Power Divider with $R = 105 \Omega$.....	87
III.3.2 Power Divider with $R = 150 \Omega$.....	90
III.4 HARMONICS SUPPRESSION.....	92
III.5 ANTENNAS ARRAY FEEDING NETWORK APPLICATION	95
III.5.1 2.45 GHz working frequency	95
III.5.2 5.8 GHz working frequency.....	96
III.5.2.1 1:4 feeding network.....	96
III.5.2.2 1:4 feeding circuit with antennas.....	97
III.6 MILLIMETRE-WAVE APPLICATION.....	98
III.6.1 Design and simulation	99

III.6.2 Sensitivity to the resistance value.....	101
III.7 CONCLUSION	102
CHAPTER IV : NEW TOPOLOGIES OF REFLECTION TYPE PHASE SHIFTER FOR HIGH FIGURE OF MERIT	103
IV.1 STUDY OF THE TOPOLOGIES	104
IV.1.1 Reflection load with one varactor	104
IV.1.2 Reflection load with two varactors.....	108
IV.1.3 Reflection load with three varactors	109
IV.2 DESIGN PROCEDURE	111
IV.3 CIRCUITS DESIGN AND EXPERIMENTAL RESULTS IN PCB.....	112
IV.3.1 Reflection load with one varactor	113
IV.3.2 RTPS with reflection load with two varactors cascaded with a Π -type phase shifter	114
IV.3.2.1 Choice of the RTPS.....	115
IV.3.2.2 Optimization of the Π -type phase shifter	116
IV.3.2.3 Simulation of the RTPS with the Π -type phase shifter	117
IV.3.2.4 Measurement results	118
IV.3.3 Reflection load with three varactors.....	119
IV.3.4 Results synthesis	121
IV.4 RTPS IN INTEGRATED TECHNOLOGY	122
IV.4.1 Topology of the reflection load based on a distributed loaded line phase shifter	122
IV.4.2 Layout and simulation of the RTPS.....	124
IV.4.3 RTPS, loaded line phase shifter alone and state-of-the-art comparison	125
IV.5 PERSPECTIVES.....	126
IV.6 CONCLUSION	127
CONCLUSION.....	129
APPENDIX-A.....	131
APPENDIX-B.....	133
REFERENCES.....	135
PUBLICATIONS.....	143

Introduction

Nowadays, 21st century, progress and innovation in science and technology are jaw-dropping. Wave propagation is directly impacted by the technology developments in several domains and applications. More particularly, millimetre-waves have concentrated much and much interest since more than ten years. Two main advantages, as compared to radio frequencies (RF, a few GHz), make millimetre-waves attractive today, (i) the wide bandwidth and (ii) the antennas small size. In current systems, the bandwidth is more or less proportional to the working frequency; except for the particular case of Ultra-Wide-Band dedicated to short range low data-rate communications, the relative bandwidth is limited to a maximum of 10 to 15 %. Hence, for a given relative bandwidth, increasing the working frequency increases the bandwidth. The antennas size is also a key issue. It is obvious that smaller antennas lead to smaller systems, but the main interest stays the possibility to achieve large antennas arrays allowing focused beams, which is mandatory in order to address consumption issues for autonomous systems. Antennas arrays also enable to carry out beam-steering and/or beam-forming systems by using phased antenna arrays. In a more general point of view, millimetre-waves antenna arrays lead to an improved efficiency, as compared to RF systems, for the same area of the antenna system.

High-data-rate communications, radars, security, and medical applications are concerned by the development of millimetre-wave systems. In order to ensure data rates greater than a few Gbit/s, the most suitable solution has been to operate in the millimetre-waves. In the vicinity of 60 GHz, in particular, a common 5 GHz band between 59 and 64 GHz was defined for unlicensed use in the countries where the consumer electronic market was the most developed. This spectrum is an attractive option for very high data rate wireless local area networks (WLANs) or wireless personal area networks (WPAN). Moreover, this millimetre-waves radiation is capable of penetrating clothing while being partially reflected by human skin. As the reflection pattern of metals, but also plastics, ceramics and liquids are readily detectable for radiation at these frequencies, millimetre-waves imagers have been considered as a superior alternative as compared to traditional metal detectors. Hence, the security domain constitutes one of the major areas for millimetre-waves imaging systems. The frequencies better suited to this use are 35, 94, 140, and 220 GHz, which correspond to the atmospheric propagation windows, e.g. to the minima observed in terms of atmospheric attenuation. In the past, 94 GHz systems were usually adopted, but higher frequencies, leading to even better spatial resolutions, are under study. Recently, significant technological advances in the automotive industry have taken place for improving vehicles safety. The radar system can detect and track objects in the frequency domain triggering a driver warning of an imminent collision and initiate electronic stability control intervention. For long range radar there is a certain international consensus regarding the 76-77 GHz band whereas for short range such as anti-collision and

handheld radars for parking assistance, pre-crash sensing, obstacle avoidance and blind spot detection the working frequency was fixed to 79 GHz. Here again, high spatial resolution is required and obviously the smallest antennas as possible.

All these millimetre-waves applications are commonly recognized to belong to and to lead to a smart society because they will facilitate the communications between people, inside or outside homes and offices, and from building to building (backhauling), avoiding heavy civil engineering infrastructure. They will also increase safety in transports, with improvement of traffic and parking. Nonetheless, they will also be sustainable because they will not consume much power, will have a small area and high performances level.

CMOS and BiCMOS technologies are addressed to fabricate low cost millimetre-wave devices. Indeed traditional monolithic microwave integrated circuits (MMICs) with Gallium Arsenide (GaAs) can provide high-performance millimetre-waves devices due to the higher electron mobility of GaAs, higher breakdown voltage, and good insulating properties. However, GaAs technology is expensive even in mass production, which results in systems with prohibitive costs for consumer applications. This is why CMOS/BiCMOS technologies are preferred for mass production.

Such applications convey high innovation. They will also permit a large part of the microelectronic industry in developed countries to pursue its activities.

As discussed above, for some applications beam-steering systems are required either to achieve specific functions (e.g. radars) or to improve point-to-point transmissions efficiency. The beam-steering approach gives spatial agility, locating and concentrating the emitted/received energy in the direction of the receiver/emitter. This allows a longer communication range and an improvement of the system capability, leading to a more secure communication, and also to the detection of mobile blind spots. In that case, the system will quickly establish a new communication path, using for example, beams that reflect off the walls. It is a significant technological challenge to achieve such goal in a compact, cost-effective and energy-efficient solution. Mechanical beam-steering has been used with the advantage of a wide field of view and no signal processing requirement; but its manufacturing complexity, size, weight and scanning rate are not appropriate for low-cost consumer applications. Nowadays, few techniques have been developed for beam-steering. It can be performed by changing the phase of the local oscillator at the millimetre-wave mixers level but high power consumption is induced because one mixer is necessary for each antenna element of the antenna array. Other realizations have shown monolithic millimetre-waves antenna array front-ends, with digitally processed phase shifting for each antenna. Here again, the main drawback of such approach is linked to its very high power consumption, which is not compatible with mobile applications where autonomy is mandatory. The phase shifting in the millimetre-waves path would ensure low power consumption. The system could be very simple, with simple power splitters feeding phase shifters controlling each antenna of the antenna array. The key issue is then to improve the

devices performance while decreasing their surface area in order to decrease the fabrication costs. A great challenge!

To improve the performances and reduce the area of the passive components needed in the millimetre-waves range, slow wave transmissions lines have proved to be good candidates and particularly the slow-wave coplanar waveguides (S-CPWs). It has been shown in [1] and [2] that the phase constant (β) increases while keeping the same attenuation constant (α) than a classical microstrip transmission line, leading to a quality factor (Q) defined as:

$$Q = \frac{\beta}{2\alpha}$$

about two to three times higher than the classical transmission line. With such transmission lines not only performances can be improved but also the compactness of the devices.

The performances of the integrated tunable devices are usually related to the tuning elements used to vary the phase. The utilization of varactors induces high insertion loss level because of the low quality factor of the varactors, particularly at millimetre-wave frequencies. Until no varactors with better performances are achieved, all the tunable topologies developed at RF frequencies have to be studied again in order to reduce the insertion loss or should be modified in order to substitute the varactors. Ferrites could be used for this purpose but they suffer from high cost and lead to large size components. Liquid crystal (LC) appears to be a promising tunable dielectric, since its losses decrease with frequency. Thus, it is ideally suited for high performance millimetre-waves applications. At these frequencies, LC features low dielectric losses and continuous tunability. The main drawback of LC-based devices is the response time (tenths of ms) and the length of the devices due to a low tunability of the dielectric constant of about 25 %. BST material is a good candidate at RF frequencies, but suffers from high dielectric losses at millimetre-waves. Finally, microelectromechanical systems (MEMS) have the potential to be inexpensive, low loss, with high quality phase-shifting capability. However, all the above technologies are not compatible with CMOS unless performing a post-process. Hence, in parallel of the study of these hybrid solutions, it is still important to continue to study fully integrated solutions and try to develop high-quality factor tunable elements.

The purpose of my thesis work was thus to explore the possibilities to use S-CPWs in order to achieve high-performance passive devices at millimetre-waves. Power dividers, baluns and phase shifters were realized in CMOS or BiCMOS technologies. Efforts were carried out towards the study of new topologies in order to improve both performance and compactness. Some devices were first realized at RF in a PCB technology as a proof-of-concept, but also for some of them because their development at RF frequencies was interesting for RF systems.

In the first chapter, the principle of planar dividers/combiners with their most important striking evolutions and applications in the RF range are given. Baluns are considered as an application of certain power divider type devices. Then, the reflection type phase shifter topology is explored. The common miniaturization techniques for all the presented components are also listed. Finally, the state-of-the-art, at millimetre-waves, for phase shifters and power dividers is developed.

In the second chapter, in order to highlight the great interest of slow-wave coplanar waveguides at millimetre-waves, baluns achieved by the use of power dividers and a wideband phase inverter were designed in the 65 nm CMOS technology and measured. Also, power dividers with in phase (modified Wilkinson power divider) and in quadrature (branch-line coupler) were designed in the 28 nm CMOS technology.

The third chapter presents a new topology of in phase power divider, which is compact and flexible, perfectly adapted to millimetre-waves. Two power dividers and two antennas array feeding circuits were realized in PCB technology, as a proof-of-concept, and then characterized. Next, the simulation results of such a power divider with slow-wave coplanar waveguides designed in the 55 nm BiCMOS technology are given.

Finally, the last chapter describes a new topology of reflection type phase shifter (RTPS) in RF with a high figure-of-merit as compared to the state-of-the-art. This topology is based on lumped varactors together with transmission lines as a reflexion load and was achieved after a careful study of the most suitable topologies and a new optimization procedure. A second solution of reflection type phase shifter was developed for millimetre-waves in the 55 nm BiCMOS technology. As a reflexion load, a slow-wave coplanar waveguide loaded with distributed capacitive switches is used. This phase shifter was achieved thanks to the development of a new switched capacitor showing improved quality factor as compared to the varactors available in the design kit. Designs carried out showed that high performance reflection type phase shifters could be realized thanks to this new topology.

Chapter I : Power dividers/combiners and Reflection Type Phase Shifter presentation

With the fast development of multifunctional technologies and the need for miniaturization in wireless communication systems, compact microwave components and circuits—especially microwave integrated circuits with system-level performance—have become increasingly popular. Those considerations stay available whatever the considered frequency range and topology, i.e. radio frequency (RF) in advanced PCB technologies, or millimetre-waves (mmW) compatible with CMOS and 3D integration techniques.

Among the large number of microwave integrated passive circuits, power dividers and phase shifters are fundamental, powerful and necessary, device building blocks. For wireless communication purpose, they are full part of the front-end transceiver. They can also be used independently to make analog active circuits more performing: power amplifiers or local oscillators are common example.

In this chapter, after a brief overview of the already existing solutions in terms of planar dividers/combiners, we will remind the principle of the commonly used components with their most important evolution and recent applications in the RF range. In a second time, solutions for phase shifting will be explored, focusing on the theory of the Reflection Type Phase Shifting, the most appropriate technique to combine high phase shifting and port matching in the meantime. Various topologies are compared and explained. Then, we will list, illustrate and comment miniaturization techniques; most of which are similarly used to miniaturize both components: power dividers and phase shifters. Finally, we will draw the state-of-the-art, at millimetre-waves, for phase shifters, power dividers, and baluns (one application among many of power dividers).

I.1 Planar dividers/combiners

Power dividers are usually considered to be a family of devices. They can be found in many applications, including power division and combination, modulation and demodulation, balanced mixing, balun for power amplification, Butler matrices, and feeding network of antenna arrays, among others. A reciprocal divider can provide an equal or unequal power split between two or more channels. Thanks to reciprocity, and assuming that input signals to be combined should be coherent and of equal magnitudes, this circuit may also be employed to combine a number of oscillators or amplifiers towards a single port.

The major parameters used to define and compare the dividers/combiners in RF and microwave integrated circuits are bandwidth, power division, relative phase difference,

phase and magnitude imbalance, insertion loss, matching or return loss, isolation, number of inputs/outputs, integration level and cost. The performances concerning these parameters have been improved over time, either developing new topologies or with the help of more advanced techniques and methodologies. Consequently, more than one hundred different types of dividers/combiners have been developed over the past four decades.

I.1.1 Overview

Dividers/combiners can be classified according to numerous characteristics. The most common ways are: distributed, lumped-element, or combination of both, number of ports, equal or unequal power division, fixed or tunable power division, bandwidth and relative phase difference. Hereby this is the last criterion which is chosen as a parameter so that the graph in Figure I.1 shows the main planar dividers/combiners classified according to the relative phase difference. Outputs can be in phase ($\Delta_\varphi = 0^\circ$), in quadrature ($\Delta_\varphi = 90^\circ$) or out-of-phase ($\Delta_\varphi = 180^\circ$).

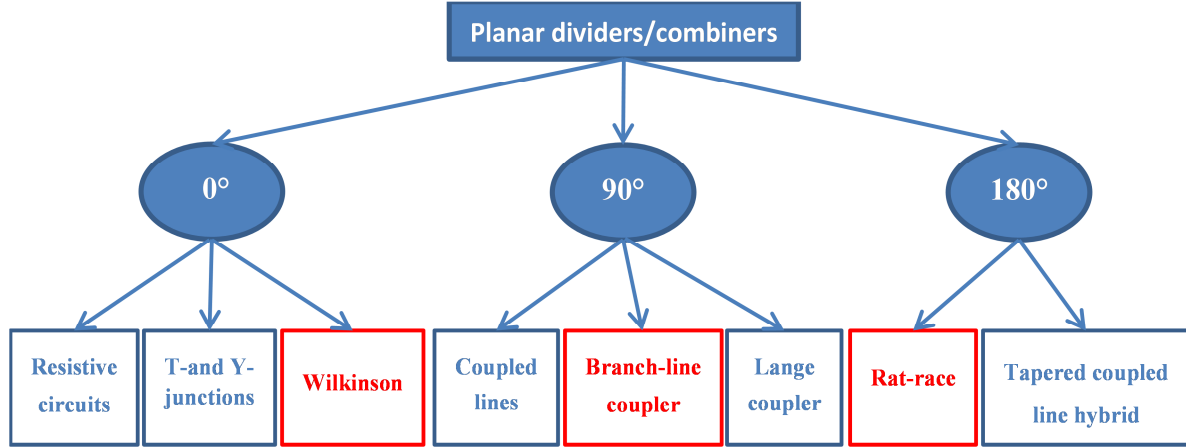


Figure I.1: Main types of planar dividers/combiners

This study concentrates on the Wilkinson power divider/combiner, the branch-line coupler and the rat-race. They are the three mostly used dividers/combiners among the ones of their phase difference category.

I.1.2 Wilkinson power divider/combiner

I.1.2.1 Presentation

The lossless Wilkinson divider/combiner developed in 1960 [3], shown in Figure I.2, is composed of two quarter wave transmission lines (TLs), of characteristic impedance $Z_0\sqrt{2}$, with Z_0 being the ports impedance. It is a really efficient component in terms of matching and isolation. Indeed, it can be matched at all ports simultaneously, while keeping isolation, thanks to a unique lossy element R connected between the two output ports. The branch between the output ports is named isolation branch. Theoretically, the resistance R

equates $2 \times Z_0$. However, this resistance limits the ability to combine any signals of higher power than that developed in the isolation branch, which is usually rated for several watts.

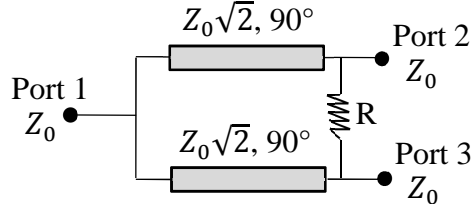


Figure I.2 : Wilkinson power divider

Because of the quarter wave TLs, its relative bandwidth under 20 dB of return loss is limited to 20 %. For the applications requiring broadband one possibility consists to cascade the dividers. Obviously, not only the bandwidth increases but the insertion loss and the complexity of the device as well. The real divider characteristics deviate from the ideal ones, due to manufacture tolerances, losses, discontinuities, mismatching of the terminations, as well as the physical quality of the resistance. The influence of these different factors on the parameters of the divider was examined by Paral and Moynihan in 1965 [4]. The ideal $[S]$ matrix has the following form:

$$[S] = \frac{-j}{\sqrt{2}} \begin{bmatrix} 0 & 1 & 1 \\ 1 & 0 & 0 \\ 1 & 0 & 0 \end{bmatrix} \quad (\text{I-1})$$

I.1.2.2 Evolution

The first modified Wilkinson divider/combiner with unequal power-split ratio was presented in [4] (see Figure I.3 and equations (I-2)). The electrical lengths of the four TLs are 90° at the working frequency. The properties of full-matching and isolation at the working frequency are observed.

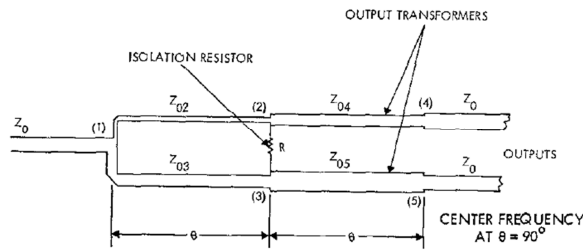


Figure I.3 : Wilkinson power divider with arbitrary power division

$$\begin{aligned} \frac{\text{POWER AT PORT 4}}{\text{POWER AT PORT 5}} &= \frac{1}{K^2} & R &= Z_0 \frac{1+K^2}{K} \\ Z_{02} &= Z_0 \sqrt{K(1+K^2)} & Z_{04} &= Z_0 \sqrt{K} \\ Z_{03} &= Z_0 \sqrt{\frac{1+K^2}{K^3}} & Z_{05} &= \frac{Z_0}{\sqrt{K}} \end{aligned} \quad (\text{I-2})$$

However, when the power dividing ratio is higher than 3 ($K^2 > 3$), TLs with very high characteristic impedances are required. Some popular TLs with potentially very high characteristic impedances, such as microstrip or CPW, become too narrow to be realized practically. The high characteristic impedance can be realised by using a meander-shaped defected ground structure (DGS) [5]. Nevertheless, the increase of impedance in such a manner is limited. The rectangular-shaped defected ground structure is also effective for the realisation of high characteristic impedances [6]. In [7] the high characteristic impedances for a 5:1 unequal power divider were realized by using offset doubled-sided parallel-strip lines (DSPSL). DSPSL-to-microstrip transitions have to be employed at the three ports, which inevitably introduces additional insertion loss and increases the circuit size. The grooved substrate microstrip method could be used to realize high characteristic impedance as in [8]. But this grooved substrate microstrip is difficult to be fabricated, compared to traditional microstrip. In [9] the high characteristic impedance TLs were replaced by T-shaped structures, in order to decrease the characteristic impedances towards more suitable values. In the case of the 4:1 unequal divider designed, the highest characteristic impedance was 97 Ω and the lowest 43 Ω instead of 158 Ω and 35 Ω for the conventional unequal divider.

I.1.2.3 Striking applications

I.1.2.3.a Feeding network

The Wilkinson power divider is the basic device for many applications. In [10] and [11], it was used as a feeding circuit for antenna arrays beam forming. In [10] one power divider feeds two antennas and used stepped-impedance open-circuited radial stubs to achieve good operation within a ultra-wide band. In [11] two power dividers in parallel were connected at the outputs of a first one to feed an array of four antennas as shown in Figure I.4. Phase shifters between the Wilkinson power dividers and the antennas enable beam-steering. In both cases, the measured input reflection coefficient (S_{11}) is below -10 dB, in the band 4-14 GHz for [10] and 1.8-2.1 GHz for [11], respectively.

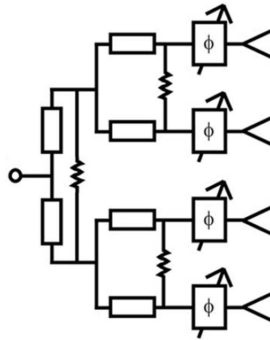


Figure I.4 : Electronic passive vertical beam scanning with Wilkinson dividers and phase shifters.

I.1.2.3.b Balun

If a phase inverter is placed in series with one of the two quarter wave TLs of the Wilkinson power divider, as in Figure I.5, the 180° relative phase difference obtained between the two output ports makes its use as a balun possible. The output ports of the modified Wilkinson power divider stay close to each other. We will see soon this is a great advantage comparing to the rat-race balun. However, the resistance R , mandatory for isolation and output matching, must be removed. Indeed, the 180° relative phase difference between the outputs would create a permanent flowing current through the resistance and would increase considerably the losses. When removing this resistance, isolation and output ports matching are degraded in such a way that the component cannot be used anymore as a combiner. Nevertheless, it is still remarkably suitable for differential power amplification. This device, performed at the IMEP-LAHC, is totally novel. It has been designed and measured in a 65 nm CMOS technology and will be described in detail in chapter II. It is not referenced herein since the final version is an optimised case of Figure I.5.

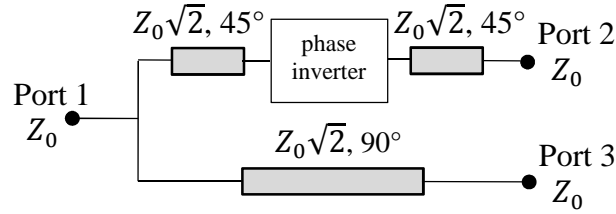


Figure I.5 : Modified Wilkinson divider with phase inverter for balun application.

I.1.3 Branch-line coupler

I.1.3.1 Presentation

The branch-line coupler or 90° hybrid coupler is a particular case of a directional coupler. It is a four ports network where coupling factor is -3 dB and phase relationship between the output ports is 90° . The ideal coupler is lossless and matched at all ports. Compared to the Wilkinson power divider, it does not need any resistance for ports matching, but requires a fourth port. The branch-line coupler is composed by four quarter wave TLs of characteristic impedances Z_0 for the vertical TLs and $Z_0/\sqrt{2}$ for the horizontal ones in a Z_0 system as shown in Figure I.6. Incident power at port 1 separates between port 2 (the through port) and port 3 (the coupled port), but no power flows through port 4 (the isolated port). Similarly, incident power at port 2 will couple to ports 1 and 4, but not 3. Thus, ports 1 and 4 are decoupled, as are ports 2 and 3. The fraction of power coupled from port 1 to port 3, named coupling (C), is given by (I-3). The leakage of power from port 1 to port 4 is given by (I-4) and is named isolation (I). To conclude, the directivity (D), which is the ratio of the power delivered to the coupled port and the isolated port is defined as $D = I - C$ (dB) or by (I-5).

$$\text{Coupling} = C = -10 \log \frac{P_3}{P_1} = -10 \log |S_{31}|^2 \quad (\text{I-3})$$

$$\text{Isolation} = I = -10 \log \frac{P_4}{P_1} = -10 \log |S_{41}|^2 \quad (\text{I-4})$$

$$\text{Directivity} = D = -10 \log \frac{P_4}{P_3} = -10 \log |S_{43}|^2 \quad (\text{I-5})$$

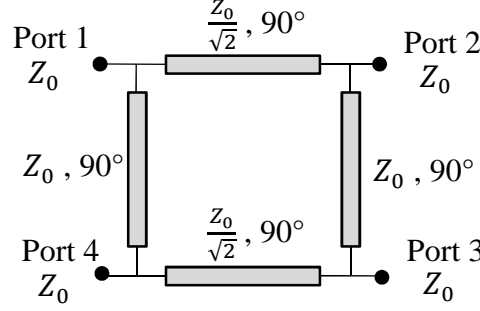


Figure I.6 : Branch-line coupler

The bandwidth of this device is about 10-20 %. As for the Wilkinson power divider, by cascading dividers, the bandwidth is enlarged, leading unfortunately to an increase of the insertion loss and the complexity of the device. Scattering parameters demonstration is available in [12]. The ideal $[S]$ matrix has the following form:

$$[S] = \frac{-1}{\sqrt{2}} \begin{bmatrix} 0 & j & 1 & 0 \\ j & 0 & 0 & 1 \\ 1 & 0 & 0 & j \\ 0 & 1 & j & 0 \end{bmatrix} \quad (\text{I-6})$$

I.1.3.2 Evolution

When the output ports of the hybrid coupler are connected to impedances different from Z_0 , an additional matching network is needed. To avoid the need for a supplementary network, [13] presented a device with both arbitrary termination impedances and arbitrary power division. By referring to the nomenclature in Figure I.7, the ratio of the scattering parameters $|S_{11}|$ to $|S_{31}|$ is that of d_1 to d_2 . The electrical TL lengths θ_1 , θ_2 , θ_3 , and θ_4 are all $\lambda/4$ at the centre frequency, and the characteristic impedances Z_1 , Z_2 , Z_3 and Z_4 in Figure I.7 are expressed as:

$$\begin{aligned} Z_1 &= \sqrt{\frac{d_1^2}{d_1^2 + d_2^2}} \sqrt{R_a R_b} & Z_2 &= \frac{d_1}{d_2} \sqrt{R_b R_c} \\ Z_3 &= \sqrt{\frac{d_1^2}{d_1^2 + d_2^2}} \sqrt{R_c R_d} & Z_4 &= \frac{d_1}{d_2} \sqrt{R_d R_a} \end{aligned} \quad (\text{I-7})$$

where R_a , R_b , R_c , and R_d are the real impedances termination. For both $d_1 = d_2$ and $R_a = R_b = R_c = R_d$, the results are similar to a conventional 3 dB branch-line hybrid.

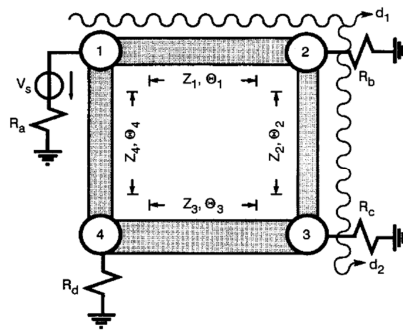


Figure I.7 : Branch-line coupler with both arbitrary termination impedances and arbitrary power division

I.1.3.3 Striking applications

I.1.3.3.a *Coupling for frequency mixing*

Mixers are frequency translation devices. Thanks to a local oscillator (LO), they allow the signal conversion from a high frequency (RF) to a lower intermediate frequency (IF or baseband), and inversely. In down-conversions, hybrids as well as rat-races may be used as functional passives to bring the RF and LO signals towards the non-linear active component. In [14], a 138 GHz down-conversion mixer with a branch-line coupler was developed. It was based on a 90 nm CMOS technology. As shown in Figure I.8 the branch-line coupler converts the separated RF and LO input signals into two RF-LO combined signals, which were injected into M1 and M2 that basically operate as independent mixers and generate the IF signals. Although at 138 GHz a quarter wavelength line, equivalent to one edge of the coupler, becomes shorter than 300 μm on silicon substrates, the size is still reduced with specific techniques such as capacitive open-stub loading (non-visible here). This miniaturization technique will be explained with more details further in this chapter.

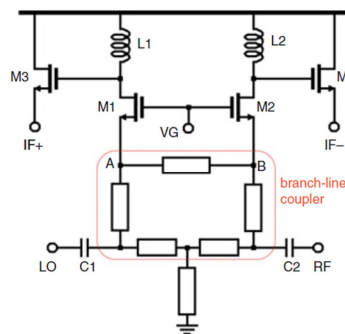


Figure I.8 : Down-conversion mixer with branch-line coupler

I.1.3.3.b *Reflection Type Phase Shifting*

When connecting the output ports 2 and 3 of a branch-line coupler by two identical reflective loads, a reflection type device is obtained between ports 1 and 4. If Γ is the reflection coefficient at ports 2 or 3, the phase shift between ports 1 and 4 is equal to the phase of Γ plus 90° ; such device is so called Reflection Type Phase Shifter (RTPS). Figure I.9 shows the block diagram of a typical RTPS with the impedance value of the reflective

loads denoted as Z_L . If Z_L is purely reactive, there is no power lost in the reflective loads so that the whole power is coupled to the output. The main advantage of this configuration is that input and output impedance matching is preserved, whatever the phase shifting is, as long as the coupler is terminated with identical reflective loads. Any load which can provide an impedance mismatch can produce reflections. However, to get better performance, which means high phase shifting with low loss, different kinds of modified loads were compared. In chapter IV, devices with optimised loads are achieved and measured in a PCB technology with state-of-the-art performances. Simulations in a CMOS technology show excellent performances, to be confirmed soon by measurements.

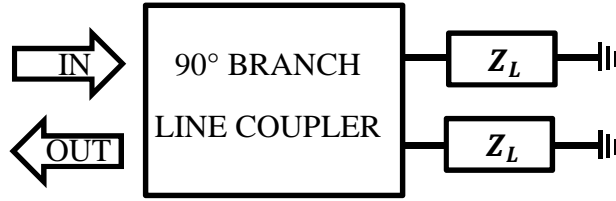


Figure I.9: Block diagram of a RTPS

I.1.4 Rat race coupler

I.1.4.1 Presentation

The rat-race coupler or hybrid ring directional coupler is a lossless reciprocal four ports network. The conventional circuit is schematized in Figure I.10. It comprises three 90° branches and one 270° branch. The characteristic impedance of the ring branches should be $\sqrt{2}$ times the characteristic impedance of the ports terminations with the purpose of impedance matching at all ports.

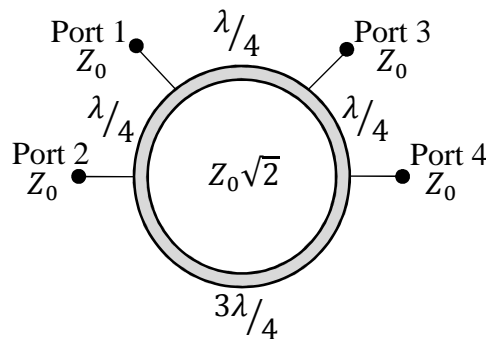


Figure I.10 : Rat-race coupler

Historically, the first hybrid ring was described by Tyrrel in 1947 [15]. As a power divider, the rat-race coupler can be used for in-phase operation and 180° out-of-phase operation. However some of the components described herein are much more suitable and compact for in phase power division. Consequently, the rat race coupler is mainly used for 180° out-of-phase. For this application, a signal injected at port 2 divides evenly between ports 1 and 4 with 180° phase difference, meanwhile port 3 keeps isolated. As a power

combiner, signals are simultaneously injected in phase at ports 2 and 3, summing at port 1, and subtracting at port 4. Consequently, ports 1 and 4 are referred to as Σ and Δ , respectively. By contrast, if signals injected at ports 2 and 3 have a 180° phase shift, sum and difference result inversely at ports 1 and 4. The bandwidth of this device is less than 25 %; improvement can be obtained by the addition of a fifth port. Scattering parameters demonstration is available in [12]. The $[S]$ matrix has the following form:

$$[S] = \frac{-j}{\sqrt{2}} \begin{bmatrix} 0 & 1 & 1 & 0 \\ 1 & 0 & 0 & -1 \\ 1 & 0 & 0 & 1 \\ 0 & -1 & 1 & 0 \end{bmatrix} \quad (\text{I-8})$$

I.1.4.2 Evolution

In 1961, [16] gave the design equations of a rat-race coupler with any degree of coupling. These equations are detailed in (I-9) with Y_1 and Y_2 the normalized admittances and a_i and b_i the incident and reflected waves at port i , respectively, as in Figure I.11.

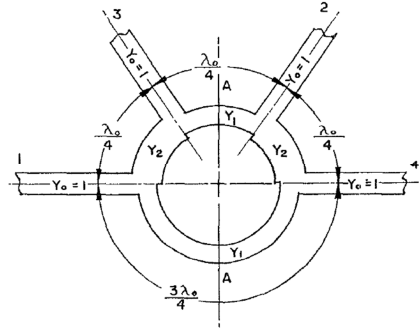


Figure I.11 : Rat-race with any degree of coupling

$$\begin{aligned} Y_1^2 + Y_2^2 &= 1 \\ \frac{b_3}{b_4} &= -\frac{Y_2}{Y_1} \\ \frac{b_1}{b_2} &= \frac{Y_2}{Y_1} \end{aligned} \quad (\text{I-9})$$

In 2007, Mandal and Sanyal proved that there is more than one solution in terms of electrical lengths and characteristic impedances to bring to a lossless, isolated and full-matched component. Indeed, in [17] it is shown that an infinite number of solutions exist for coupler design at a given frequency. For all the solutions, characteristic impedances are less than the conventional $Z_0\sqrt{2}$. Theoretically, the characteristic impedance of the ring can be chosen between 0 and $70.7 \, \Omega$ in a $50 \, \Omega$ system. For each value, two ring electrical lengths are addressable, one giving a total ring electrical length higher than $1.5 \, \lambda$ and one lower. The drawback is the bandwidth strengthening further and further with the decrease of the total electrical length.

I.1.4.3 Application

The main application of the rat race coupler is the balun function, used for instance in balanced mixers as in [18]. The single balanced mixer gets use of a microstrip rat race hybrid and two GaAs Schottky diodes, in the configuration given in Figure I.12. The LO and RF signals are mixed in these diodes and are isolated by the rat-race. The IF port is isolated from both the RF port and the LO port by the low-pass filter. The RF chokes provide a tuning mechanism and prevent the RF signal from leaking into ground. Measurement results show that conversion loss is less than 13.5 dB from 90 GHz to 97 GHz. Such mixer can be widely used in communication and radar systems in the mmW range.

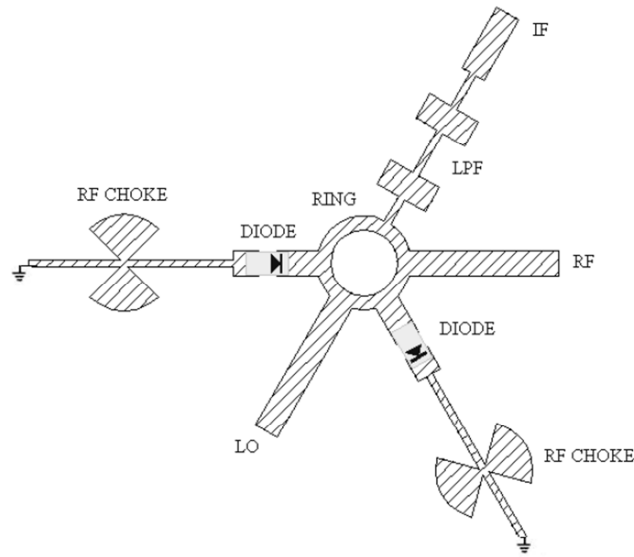


Figure I.12 : Configuration of the rat-race balanced mixer [18].

Another application of the rat race as a balun is the differential measurement as presented in [19]. The purpose is to measure the gain and noise performances of differential amplifiers by using single-ended measurements. Ideally, the input balun B1 shown in Figure I.13, equally splits the signal along two 180° out-of-phase branches. The behaviour of the output balun B2 is equivalent, although combining the output signals from the amplifiers A. Baluns to characterize a differential amplifier allow the use of conventional two ports measurement equipment.

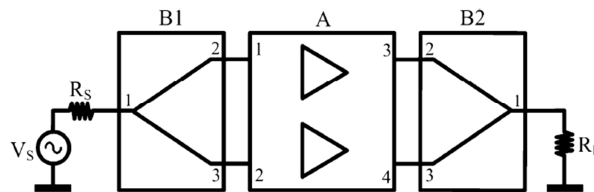


Figure I.13: Measurement procedure of a differential amplifier using baluns.

I.2 Reflection Type Phase Shifter

I.2.1 Principle and theory

The first Reflection Type Phase Shifter (RTPS) was proposed in 1960 by Hardin *et al.* [20]. The RTPS is composed by the branch-line coupler given in Figure I.7 with equal power split loaded by two identical varactors as in Figure I.14. The usual input and isolation ports of the branch-line coupler alone, ports 1 and 2 in Figure I.14, have a port impedance of Z_0 , whereas the usual through and coupled ports have a port impedance of Z_T . The input signal is divided into two parts. Each part is reflected by a reflective load, to finally combine at the last port.

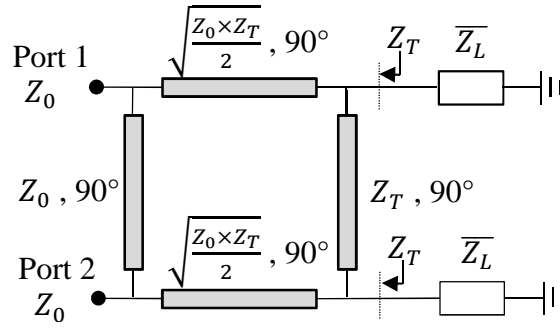


Figure I.14 : RTPS loaded by varactors

The calculation of the transmission parameter S_{21} with the S matrix of the branch-line coupler loaded by the variable impedances $\overline{Z_L}$ easily brings to:

$$S_{21} = j\overline{\Gamma} \quad (\text{I-10})$$

with $\overline{\Gamma}$ the reflection coefficient between the outputs of the branch-line and the loads defined as:

$$\overline{\Gamma} = \frac{\overline{Z_L} - Z_T}{\overline{Z_L} + Z_T} \quad (\text{I-11})$$

Considering the load $\overline{Z_L}$ as an ideal varactor $1/jC\omega$, the magnitude of the transmission parameter S_{21} is 1, which means that all the power is transmitted, while the phase depends on the reflection coefficient $\overline{\Gamma}$ and so, on the load $\overline{Z_L}$. The principle of the RTPS is demonstrated. Intentionally, the two following sub-parts which detail the theoretical equations for loss and phase shift are not referenced. To our best of knowledge, the analysis throughout the literature was not enabling to enlighten the compromise between minimized losses and maximized phase shift. The following demonstrations are thus totally novel.

I.2.1.1 Insertion loss

In practice the load is not ideal and leads to losses. To represent losses, a resistance R representing the loss was connected in series with $1/jC\omega$. $\overline{Z_L}$ can be written as:

$$\overline{Z}_L = R + \frac{1}{jC\omega} = R \frac{1 + j/Q}{j/Q} = R(1 - jQ) \quad (\text{I-12})$$

with Q (I-13) the quality factor of the varactor.

$$Q = \frac{1}{R \cdot C \cdot \omega} \quad (\text{I-13})$$

Under these conditions, the reflection coefficient $\bar{\Gamma}$ is:

$$\bar{\Gamma} = \frac{\overline{Z}_L - Z_T}{\overline{Z}_L + Z_T} = \frac{R(1 - jQ) - Z_T}{R(1 - jQ) + Z_T} = \frac{1 - \frac{Z_T}{R} - jQ}{1 + \frac{Z_T}{R} - jQ} = \frac{1 - \kappa - jQ}{1 + \kappa - jQ} \quad (\text{I-14})$$

with $\kappa = \frac{Z_T}{R}$.

The magnitude of S_{21} is thus given by:

$$|\overline{S}_{21}| = |\bar{\Gamma}| = \sqrt{\frac{\left(1 - \frac{Z_T}{R}\right)^2 + Q^2}{\left(1 + \frac{Z_T}{R}\right)^2 + Q^2}} = \sqrt{\frac{(1 - \kappa)^2 + Q^2}{(1 + \kappa)^2 + Q^2}} = \sqrt{\frac{1 + \left(\frac{1 - \kappa}{Q}\right)^2}{1 + \left(\frac{1 + \kappa}{Q}\right)^2}} \quad (\text{I-15})$$

According to (I-15), κ has to be much greater or much lower than 1 to get $|\overline{S}_{21}|$ close to 1 and so to reduce the insertion loss. If $Z_T = Z_0$ (for the conventional branch-line coupler), since Z_0 and R are both fixed values, this condition cannot be met for lossy varactors with the simple configuration given in Figure I.14. Looking at $\kappa = \frac{Z_T}{R}$, it is straightforward that by increasing Z_T , the condition $\kappa \gg 1$ is roughly met and therefore the insertion loss is reduced. In accordance with the formulas given in (I-7), Z_T may take any desired value while the branch-line coupler given in Figure I.14 would keep equal split and matched ports 1 and 2.

I.2.1.2 Relative phase shift

According to (I-10) and (I-14) the phase of the transmission parameter S_{21} of the RTPS is:

$$\begin{aligned} \varphi_{S_{21}} &= \frac{\pi}{2} + \text{Arg}(\bar{\Gamma}) = \frac{\pi}{2} + \text{Arg}\left(\frac{1 - \kappa - jQ}{1 + \kappa - jQ}\right) \\ &= \frac{\pi}{2} + \text{ArcTan}(-Q/(1 - \kappa)) + \text{ArcTan}(Q/(1 + \kappa)) \end{aligned} \quad (\text{I-16})$$

Among the two possible solutions for minimizing the insertion loss, the only one leading to a variable phase according to Q and so to C , is a κ much greater than 1. Indeed, with $\kappa \gg 1$:

$$\varphi_{S_{21}} \approx \frac{\pi}{2} + 2 \cdot \text{ArcTan}(Q/\kappa) = \frac{\pi}{2} + 2 \cdot \text{ArcTan}\left(\frac{1}{Z_T \cdot C \cdot \omega}\right) \quad (\text{I-17})$$

We named C_{min} and C_{max} the minimum and maximum values of the varactor. The relative phase shift calculated as $\varphi_{S_{21}(C_{min})} - \varphi_{S_{21}(C_{max})}$ is:

$$\Delta\varphi \approx 2 \cdot \left[\text{ArcTan}\left(\frac{1}{Z_T \cdot C_{min} \cdot \omega}\right) - \text{ArcTan}\left(\frac{1}{Z_T \cdot C_{max} \cdot \omega}\right) \right] \quad (\text{I-18})$$

Theoretically, if the condition $\kappa \gg 1$ is checked and if the varactor varies between 0 and $+\infty$, $\Delta\varphi$ could reach 180° without insertion loss. However, varactors have a limited range so that only a maximum relative phase shift may be reached corresponding to a fixed value of Z_T . The equation (I-18) is derived according to Z_T and fixed equal with 0 in order to find the value of Z_T leading to the maximal $\Delta\varphi$. The obtained equation is given in (I-19), and is consequently the condition to respect to get the maximal $\Delta\varphi$, considering that $\kappa \gg 1$.

$$1 = \frac{\sqrt{\frac{1}{C_{min} \cdot C_{max} \cdot \omega^2}}}{Z_T} \quad (\text{I-19})$$

To reduce the insertion loss, Z_T has to be as high as possible whilst to get the highest relative phase shift the equation (I-19) has to be verified. For a given varactor, two different criteria have to be met by only one variable. In consequence, it is not possible to benefit simultaneously from the lowest loss with the highest relative phase shift. A compromise between these two characteristics has to be found. The next part illustrates this case with a practical example.

I.2.1.3 Practical example with non-ideal varactor

Let's choose a varactor with a capacitor value C in the range [1-5] pF with a parasitic resistance R of 2Ω at 2 GHz. According to (I-19) Z_T has to be fixed to 35.6Ω to get the maximal relative phase shift. Table I.1 sums up the calculated performances of two RTPS realized with ideal hybrid couplers, taking into account only the parasitic resistance R of the load. For one RTPS $Z_T = 35.6 \Omega$, chosen to get the maximal relative phase shift, and for the other one $Z_T = 100 \Omega$, chosen as high as possible to respect $\kappa \gg 1$ while taking into account standard technology limitation.

Z_T (Ω)	κ	Approximate $\Delta\varphi$ according to (I-18) ($^\circ$)	Exact $\Delta\varphi$ according to (I-16) ($^\circ$)	Max. insertion loss according to (I-15) (dB)	FoM ($^\circ/\text{dB}$)
35.6	17,8	80.57	83.53	0.81	75.3
100	50	58.79	58.94	0.34	92.1

Table I.1 : RTPS performances with simple capacitive reflective load.

The figure-of-merit (FoM) of a phase shifter is defined as the relative phase shift over the maximum insertion loss. It would not be accurate to calculate the FoM only taking into account the loss due to R , if we consider that these circuits were fabricated on a

dielectric substrate with $\tan \delta = 0.0027$, the insertion loss added by the branch-line coupler is estimated to about 0.3 dB. So the FoMs presented here take also into account the insertion loss induce by the branch-line coupler.

With $Z_T = 35.6 \Omega$, the relative phase shift is about 83° with 0.81 dB of insertion loss leading to a FoM of 75.3 °/dB. As expected, with $Z_T = 100 \Omega$ the insertion loss is lower with 0.34 dB but the relative phase shift as well with 59° . The FoM is higher with 92.1 °/dB. We can notify that the criteria $\kappa \gg 1$ is respected in both cases, because the error between the approximate $\Delta\varphi$ and the exact one is less than 4 %.

I.2.1.4 Conclusion

The ideal RTPS is lossless and has a phase controlled by the loads connected at the branch-line output ports. Due to the limited range and the parasitic resistance of the varying loads, the performances of the phase shifter are getting worse. With the flexible output port impedance of the branch-line coupler, it is possible to find different values than the classical 50Ω in such a way that performances can be improved. It will be a compromise between the relative phase shift and the loss level. However, in this configuration the maximum relative phase shift stays modest and not high enough for some applications. In order to get more degrees of freedom than the only Z_T for better performances and compromise, networks may be placed between the output ports of the branch-line coupler and the varactors. As we have seen, the purpose is to get a value of Z_T different from R , so the added network can be called a mismatching network. The next part introduces the most usual modified reflective loads including mismatching network.

I.2.2 Modified reflective load

I.2.2.1 Serial inductance

A modified reflective load can be designed with one, two or even more varactors depending on the targeted phase shift. As a general rule, the more varactors, higher the phase shift. The simplest modified reflective load used as a mismatching network is a series inductance with the varactor, also named series-resonating load. We will first explain the advantages of this widely used reflective load before presenting mismatching networks with or without inductance, but of higher complexity.

If the reflective load consists in a fixed inductance L in series with an ideal varactor C as in Figure I.15, the reflective load becomes:

$$Z_L = jL\omega + \frac{1}{jC\omega} \quad (\text{I-20})$$

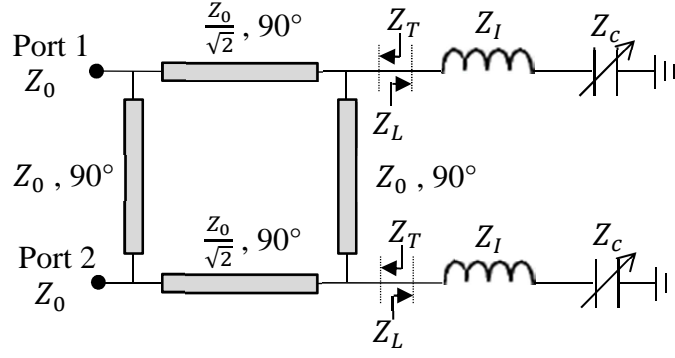


Figure I.15 : RTPS with inductive load.

The minimum and maximum values of Z_L are reached for the extreme values of the variable C . For this study, C and L are ideal, e.g. without loss, and C can reach any value in the $[0; +\infty]$ range.

For $C = 0$: $Z_L = jL\omega - j\infty = -j\infty$ (L has no influence)

For $C = +\infty$: $Z_L = jL\omega + \frac{1}{+j\infty} = jL\omega$ if $L = +\infty$, $Z_L = +j\infty$

So $\Delta\varphi = 2 \cdot \left[\text{ArcTan}\left(\frac{-j\infty}{Z_0}\right) - \text{ArcTan}\left(\frac{+j\infty}{Z_0}\right) \right] = 2 \cdot (90 + 90) = 360^\circ$.

When adding a series inductance the maximum relative phase shift increases up to 360° as long as its value tends to be $+\infty$. In practice the value of C and L are limited. Hence the relative phase shift is much lower, so that a compromise should be found between phase shift and insertion loss. This is shown in the state-of-the-art.

I.2.2.2 State-of-the-art at RF frequencies

I.2.2.2.a Reflective load with lumped inductance and one varactor

With an lumped inductance in series with a capacitor, a relative phase shift of 97° with 1.5 dB of maximum insertion loss was measured at 2 GHz in [21]. The varactor range value is [1.4-8] pF with a parasitic resistance of 2Ω . The insertion loss variation for the 97° is 0.4 dB. The relative phase shift is much below the 360° theoretical maximum one calculated above. This is due to the limited range of values of the varactor and the finite inductance value. Moreover, there is a compromise to make between the insertion loss and the insertion loss variation. The outputs ports impedance Z_T of the branch line coupler is 50Ω , leading to an impedance transforming ratio $r_Z = Z_0/Z_T = 1$. Still in [21], another RTPS with the same reflective load was measured, but with $Z_T = 12.5 \Omega$, e.g. $r_Z = 4$. In that condition the relative phase shift is now 240° with 3.8 dB of maximum insertion loss and an insertion loss variation of 2.2 dB. In counterpart of the increase of almost 150 % of the relative phase shift, both the maximum insertion loss and the insertion loss variation expanded. To reduce the insertion loss variation, a resistance R_P of 82Ω was connected in parallel with the load, as shown in Figure I.16.

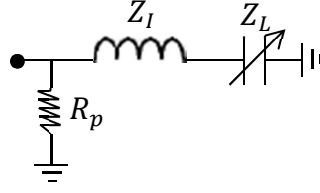


Figure I.16 : Reflective load proposed in [21].

This resistance smoothes the loss at its maximum value but does not modify the relative phase shift. Indeed, concerning the device with R_p , the maximal insertion loss is still 3.8 dB but the variation of this characteristic dwindles as low as 0.1 dB. The return loss is better than 20 dB. Figure I.17 shows the measured reflection coefficient of the three presented RTPSs at 2 GHz.

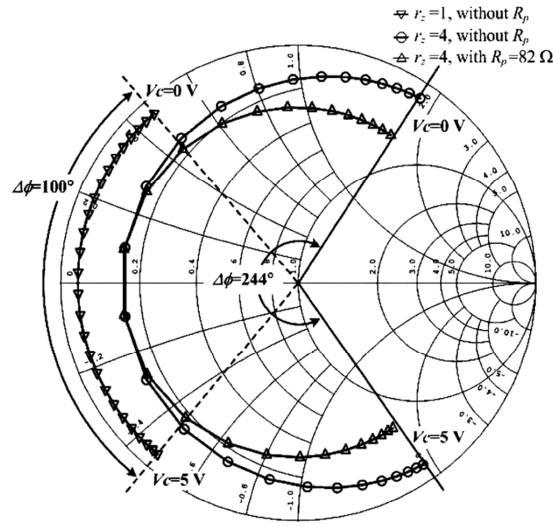


Figure I.17 : Reflection coefficient of the three types of reflective load at 2 GHz.

These results confirmed that it is not possible yet to get a relative phase shift of 360° with only one varactor in series with an inductance, due to their limited range. Other variable reflective loads have been envisaged with several varactors in order to increase $\Delta\phi$. Some of them include a series inductance.

I.2.2.2.b Reflective load with lumped inductance and several varactors

In [22], a varactor was added before the reflective load previously presented in Figure I.15, leading to a Π -shape as described in Figure I.18(a). The simulation Figure I.18(a) shows that the impedance variation of Z_{IN} is not centred anymore on the Smith chart real axis. Consequently the relative phase shift is really small. Therefore, an impedance transformation was added. On the Smith chart in Figure I.18(b), it can be seen that the simulated relative phase shift becomes higher than 360° with the impedance transformation.

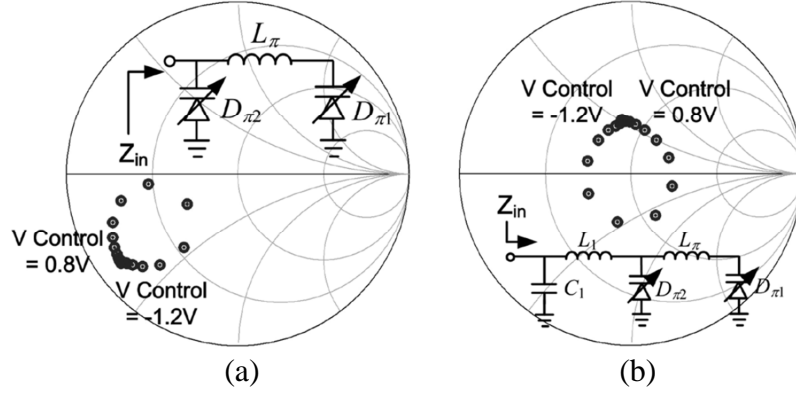


Figure I.18 : Simulated Impedance trajectory on the Smith chart. (a) II-shape load without impedance transformation. (b) II-shape load with impedance transformation.

This RTPS was implemented in a 0.18 μm CMOS technology at 2.45 GHz. The two varactors have a capacitance range of [0.52-1.4] pF and [1.9-5.4] pF, resulting in a measured relative phase shift of 340° with a maximum insertion loss of 12.6 dB and a loss variation of 4 dB. With this topology the simulated relative phase shift shown that 360° can be reached but the measurement result was limited to 341° .

In [23], the reflection loads are composed by two inductances in series with varactors, interconnected by a quarter-wavelength TL, as shown in Figure I.19.

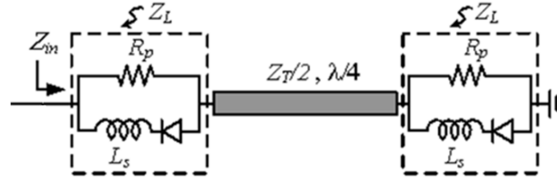


Figure I.19 : Reflective load proposed in [23].

Here again the resistance R_p was used to smooth the insertion loss, and r_z was modified and fixed to 1.25. The measured maximum relative phase shift is 407° and the insertion loss is 4.6 dB at 2 GHz with a variation of 0.4 dB. The phase shifter was realized with silicon varactors of a [1.4-8] pF capacitance range and an average 2 Ω resistance.

I.2.2.2.c Reflective load without lumped inductance

It is also possible to get 360° of relative phase shift with a reflective load without inductance. The reflective load suggested in Figure I.20 by [24] consists in two shorted transmission-line stubs connected in series with the varactors. Those two parallel arms are interconnected with a quarter-wave TL. It increases both the total amount and the linearity of the phase shift. The phase shifter showed a total phase shift of 380° and a maximum insertion loss of 5.3 dB with a variation of 1.6 dB at 10 GHz. The high insertion loss is mainly due to the GaAs beam-lead varactor diodes which exhibit a 5.5 Ω parasitic resistance.

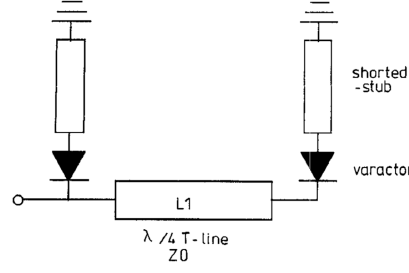


Figure I.20 : Reflective load proposed in [24].

In [25], 6 varactors were used in each reflective load. Z_L is shown in Figure I.21. Each one of the seven TL is 50- Ω quarter-wavelength arms with a varactor diode at every node. All the varactors are similar, with a [0.2-1.1] pF capacitance range. The relative phase shift is really high with 500° . The maximum insertion loss is 3.5 dB with 2.5 dB of variation. The main drawbacks of this topology are the big area needed due to the numerous quarter-wavelength TLs and the cost with the use of 12 varactors for one RTPS.

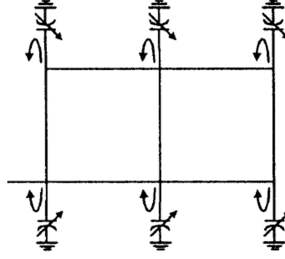


Figure I.21 : Reflective load proposed in [25].

I.2.3 Branch-line coupler substitution

The above literature review showed that all of the papers that dealt with the RTPS assumed by default that the coupler, which is the backbone of the phase shifter, is a branch-line coupler. However, the Lange coupler or quarter-wavelength coupled lines coupler can be used instead, particularly in order to increase the bandwidth. The RTPS presented in [26] consists in a CPW Lange coupler with 3-dB coupling and, as a reflective termination, a combination of two interdigital capacitors in series with an inductor. The relative phase shift is 95° at 2.5 GHz with a 96 % relative bandwidth determined for an input return loss better than 10 dB, whereas it is about 10-15 % for a RTPS using a branch-line coupler.

[27] shows that a RTPS can be designed using less than one tenth of a wavelength coupled structure if the mode impedances of that structure are chosen properly. At 2.2 GHz, the relative phase shift is 373° with a bandwidth of 36 % under 10 dB of input return loss. To achieve the maximum possible phase range across the required bandwidth, the odd-mode impedance of the short coupled structure needs to be around 10 Ω , whereas the even-mode impedance needs to be around 200 Ω . Thus, the optimized short-section design requires higher even-mode impedance and lower odd-mode impedance than the values needed in the traditional design method. To realize such extreme impedances, slotted

ground plane was used, which results in a reduction in the even-mode capacitor and, thus, an increase in the even-mode impedance. Concerning the requirement for a range of low odd-impedance values, it can be achieved by connecting a chip capacitor between the middle points of the coupled lines. This capacitor has no effect on the even-mode circuit. However, it increases the equivalent odd-mode capacitor of the coupled structure and thus decreases the odd-mode impedance.

I.2.4 Applications

Phase shifters are used to adjust transmission phase in a system; they can be fixed digital phase shifters or analogue variable types. They are key elements in phased arrays, especially tunable phase shifters. They can be used to perform adaptive beam-forming or beam-steering; they enable multi-beam operation and are also used in phase-modulation communication systems. Recently, the demand for phased array systems operating at millimetre-wave bands has increased owing to the applications of security, imaging, radars (automotive), military surveillance and satellite communication. The RTPS is praised as a low control complexity device (only one control voltage), owing good stability against temperature changes and low sensitivity to process tolerances. Nevertheless, its main advantage stays the independency between ports matching and phase tunability thanks to the recourse of a four-port coupler which leads to design simplicity and high electrical performance.

I.2.5 State-of-the-art review

Ref.	Freq. (GHz)	Phase shift (°)	Average insertion loss (dB)	Insertion loss variation (dB)	Varactor range (pF)	Parasitic resistance (Ω)	Lumped inductance	Return loss (dB)	10 dB return loss bandwidth (%)	Max. insertion loss in the BW (dB)	Nb. of varactors	Type of RTPS	FoM (°/dB)
[21]	2	237	3.75	± 0.05	1.4 - 8	2	Yes (2.7 nH)	-21	>10	>4.6	2	Branch-line	62.4
[23]	2	407	4.4	± 0.1 for 360° ± 0.2 for 407°	1.4 - 8	2	Yes (-)	-20	>10	>5.8	4	Branch-line	88.5
[24]	10	380	4.5	± 0.7	0.16 - 2.9	5.5	No	-10	-	-	4	Branch-line	73.1
[25]	2.05	500	2.2	± 1.25	0.2 - 1.1	2	No	-12	>10	>3.5	12	Branch-line	142.9
[26]	2.5	95	1.6	± 0.4	1.35-4.2	<1	Yes (2.2 nH)	-15	96	3.8	4	Lange coupler	47.5
[27]	2.2	373	2.5	± 0.75	0.6-4.8	2	Yes (1.7 nH)	-13	36	4	2	Lange coupler	116.6

Table I.2 : State-of-the-art of the RTPS in PCB technology.

Table I.2 summarizes the electrical performances and important characteristics of the RTPS in PCB technology. The RTPS presented in [25] has the highest FoM with 142.9 °/dB but suffers from serious drawbacks as the big surface, the cost due to the numerous varactors and a big variation loss. Other phase shifters reached high phase shift as in [23] with 407° but it is worth to insist that there is no practical need for phase shift over 360°. Some phase shifters have very small loss variation as in [21] but a high level of loss and are not optimized to decrease it, leading to low FoMs.

I.3 Miniaturization techniques

Size reduction is an old but very important topic that runs throughout the design procedure of microwave components from the first to the last stage. To get low cost and competitive components, the shrinking of the occupied circuit area is essential and pressing especially when considering integrated technologies like CMOS. Many efforts are carried out to miniaturize the components. Among them, TLs miniaturization is one of the research topics of major interest in the microwave range. TLs are the basis of any passive distributed device and therefore proportional. Nevertheless, attention has to be paid to other miniaturization techniques in parallel to TLs improvement. Thus in this section, several techniques dedicated to exploiting miniaturization are described. The use of high-K dielectrics was not addressed in this section, because it relates to specific substrates, and cannot be transferred to integrated technologies.

Although other performances improvement such as harmonic suppression, broadband or multiband techniques does not focus specifically on miniaturization, most of them involve it, and, thus, should be included also in this discussion. Finally, it is worth mentioning that striking references that illustrate the numerous solutions for miniaturization mainly focus on the Wilkinson power divider, the rat-race coupler and the branch-line coupler, that is to say the components studied during this thesis for power division, power combining and reflection type phase shifting purposes.

I.3.1 Shunt-stub-based artificial transmission lines

The most promising strategy for miniaturization may be the shunt-stub-based artificial TL. As an example, it has been developed as the T- and Π -shaped open-stubs in [28]. The shunt-stub-based artificial TL which consists of series high-impedance microstrip and bilateral low-impedance shunt stubs, as shown in Figure I.22(a), can be replaced by shunt stubs with two sets of high-impedance branch-type stubs to become more flexible to utilise the folding technique, as shown in Figure I.22(b). Thanks to the slow-wave effect generated by the shunt stubs, this artificial TL can replace the $\lambda/4$ TL of any device, with an equivalent 90° electrical length at centre frequency, which results in a significant miniaturization.

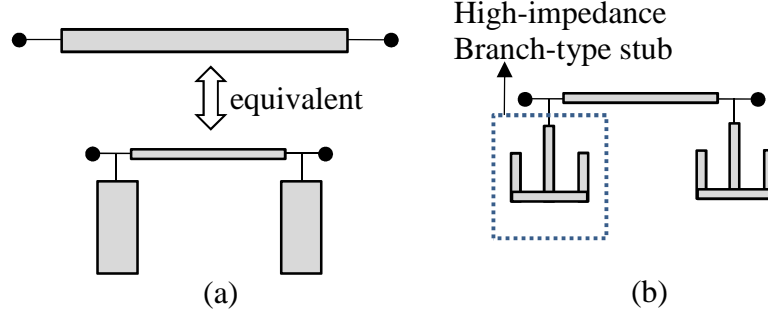


Figure I.22 : (a) A conventional TL and its π - equivalent shunt-stub-based artificial TL, (b) compact structure.

In [29], [30] and [31] this strategy was applied a Wilkinson power divider, a branch-line coupler and a rat race coupler, respectively. [29] occupies 14.7 % circuit size compared to the conventional structure, [30] occupies 8 % and [31] only 3.9 %. The drawback of this feature is the stubs characteristic impedance that can be high with non-reachable values in an integrated technology. In the previous papers the characteristic impedance may be as high as 110 Ω . In integrated technologies, values above 70 Ω are unattainable when considering microstrip TLs.

I.3.2 Meander and Fractals

The space-filling behaviour of the folding technique has proven to be beneficial in the design of small size devices. It is somewhat similar to the space-filling nature of meanders [32] and fractals [33], applied to a rat-race and a branch-line coupler. Fractal geometry is an essential and typical technique with its simple miniaturization mechanism arising from the high degree of meandering and segment compression introduced during the space-filling process. The performance of fractal-shaped devices has been demonstrated without any performance deterioration in various publications. However, it should be highlighted that the small fractal segments encountered in the second- or even higher-order iterations deserve consideration [33].

I.3.3 Phase inverter

The 270° TL needed with the conventional rat-race coupler is the main reason for its big surface. In 1968, in [34], March replaced the three-quarter wavelength section by a pair of equilateral and broadside-coupled segments of microstrip TL with an electrical length of 90°, having diametrically opposing short-circuited ends, thus creating a phase-reversing network. Its purpose was to broaden the frequency band meanwhile reducing the rat-race dimensions. In 1994 two 180° phase shifters were developed, one with coplanar striplines in [35] and one with a CPW-slotline transition in [36]. In 1999, [37] showed a phase inverter in a CPW topology with bonding wires. All these phase inverters are efficient in the framework of the fabrication of uniplanar structures although their need for bonding

wires, but they are inefficient for non-uniplanar ones. Later, the concept was developed for non-uniplanar structure as in [38] for a microstrip-CPW transition and even for microstrip TLs in [39]. In [40], a phase inverter in a CPW topology was integrated in a CMOS back end of line (BEOL). Figure I.23 shows two possible phase inverters in a CPW topology compatible with CMOS BEOLs. The symmetrical one is represented in Figure I.23(a) and the asymmetrical one in Figure I.23(b).

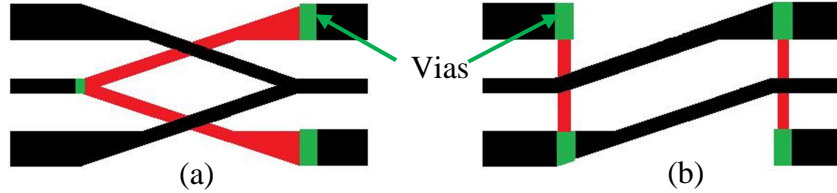


Figure I.23 : (a) Symmetrical and (b) asymmetrical CPW phase inverter.

I.3.4 Capacitor loading

To minimize the physical size of any device, lumped capacitors can load each port as in [41] or distributed capacitors can be placed along the TL as in [42] for a Wilkinson power divider, in [43] for a branch line coupler or in [44] for a rat-race coupler. [42] shrinks the area to 47 % that of the conventional structure, [43] to 38 % and [44] to only 8 %. Furthermore, the capacitor loading has good harmonic suppression performance due to its intrinsic low-pass behaviour.

I.3.5 Stepped-impedance

The stepped-impedance is also a really popular method to reduce the size of a TL. In [45] a periodic stepped-impedance was applied to a rat-race coupler. The reached relative circuit size was only 21.5 % that of the conventional one. In [28], the concept was adapted to a Wilkinson power divider. The conventional quarter-wave transformers were replaced by a constant VSWR-type transmission-line impedance transformer (CVTs). Stubs can be added at one or two extremities of these CVT in order to get a modified constant-conductance-type transmission-line impedance transformer (MCCT). According to the chosen topology, strong miniaturization can be obtained. It is possible to have CVT or MCCT with electrical lengths smaller than the 90° needed in the classical Wilkinson power divider. However, in that case, more complex isolation circuit is required to keep perfect isolation and matching at the outputs. The same author describes several design of isolation circuit in [47].

I.3.6 Slow-wave transmissions lines

The main drawbacks of the classical TL such as the microstrip TL or the coplanar TL in integrated technologies are their big surface and poor quality factor. Many different

approaches have been studied for miniaturization, for instance the use of high relative permittivity substrates or the use of lumped or semi-lumped components with interesting results at RF frequencies [48]. However these approaches cannot be transferred to CMOS technologies, especially in the mmW range. In conventional CMOS processes, classical coplanar waveguides typically suffer from significant losses (1-2 dB/mm at 10 GHz) mainly due to dielectric loss effects in the low-resistivity silicon substrate.

Slow-wave coplanar waveguides (S-CPW) are based on conventional CPW with a patterned floating shield, consisting in floating metallic strips underneath the line as shown in Figure I.24.

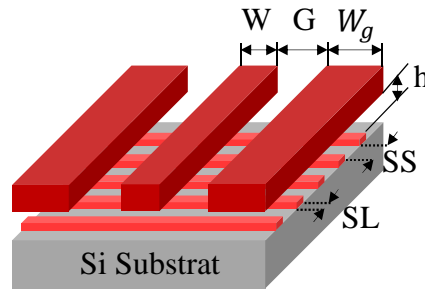


Figure I.24 : S-CPW topology.

Considering a classical S-CPW configuration, geometric parameters can be classified in two groups: one linked with the main CPW and one with the added floating strips.

- Parameters regarding the CPW:
 - W : signal strip
 - G : signal to ground gap
 - W_g : ground planes width
- Parameters regarding the floating strips:
 - SL : floating strips length
 - SS : floating strips space
 - h : dielectric thickness between floating strips and CPW

The two parameters SL and SS are chosen as the minimum allowed by the technology. Concerning SL , this enables to reduce the eddy currents that take place in the floating strips. Meanwhile the conventional conductive loss along these strips increases. Up to now, it appears that an optimum between eddy currents and conductive losses is reached for a SL lower than the minimum authorized by the technology [1]. Concerning SS , it has to be smaller or equal to h so that the patterned floating shield acts as an electric wall. The electric and magnetic fields propagation modes are shown in Figure I.25 assuming that any substrate is replaced with vacuum. The signal strip is centred, with the ground strips on its sides. The horizontal strip is the floating strip. In a 3D view, the length of the structure is equal to a period $SS+SL$ which is much smaller than a wavelength. This enabled to perform

the simulation with Flux 3DTM, a 3D quasi-static electric and magnetic solution software. The electric field, given in Figure I.25(a), is concentrated between the CPW and the floating strips so that the capacitance per unit length C_l is greatly enhanced. Moreover, there is no field underneath the floating shield, which let us think there would be no electric field neither if the substrate were the lossy silicon. On the contrary, the magnetic field, as shown in Figure I.25(b), passes through the patterned ground, so that the inductance per unit length L_l is quite unchanged and stays similar to that of a conventional CPW.

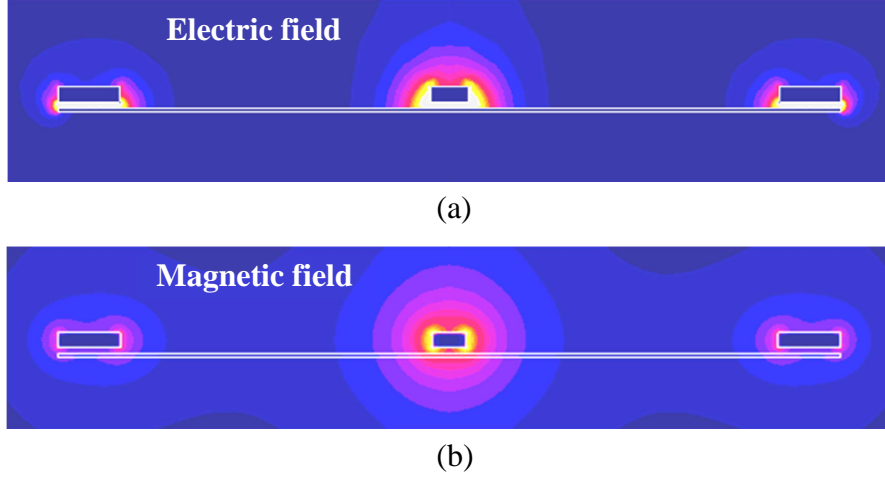


Figure I.25 : Cross-section of the (a) electric field and (b) magnetic field of a S-CPW.

In this context, the phase velocity v_ϕ given in (I-21) decreases for the S-CPW as compared to the CPW one. This explains the name: slow-wave. In the same manner, according to (I-22) a high relative effective permittivity is reached.

$$v_\phi = \frac{1}{\sqrt{L_l \cdot C_l}} \quad (\text{I-21})$$

$$\epsilon_{\text{reff}} = C_0^2 \cdot L_l \cdot C_l \quad (\text{I-22})$$

The quality factor, defined in (I-23) by [49] express the loss per degree of phase. This definition is used all along this manuscript.

$$Q = \frac{\beta}{2\alpha} \quad (\text{I-23})$$

In practice, the quality factor of slow-wave TLs carried out in CMOS/BiCMOS technologies is about 2 to 3 times higher than the classical TL one, as we will see further in chapter II, and the characteristic impedance can reach 100 Ω , that is simply impossible with other TLs, with a limitation of about 70 Ω . In [50] an efficient electric model was proposed for S-CPWs. More details about this S-CPW are given in [1] and [2].

A classical dual behaviour resonator (DBR) filter was realized in [51] by associating two different parallel open-ended stubs built with S-CPW. This topology of TL was also used to realize matching networks in a power amplifier PA at 60 GHz in [52], fabricated in the BEOL of a 65 nm CMOS technology. Power dividers were fabricated in [53] at 56 GHz

and 71 GHz without isolation and in [54] at 67 GHz with isolation. In [54] the authors did not deal with a floating shield but applied toward the CPWs periodical loading stubs and elevated signal conductors. The performances of those two power dividers are discussed in the next section focusing on the state-of-the-art review at mmW.

I.4 State-of-the-art in millimetre-waves

With increased bandwidth and speed requirement for the wireless access and data transfer, much effort has been carried out to extend the exploration of silicon-based passive components to mmW applications. Commercially available silicon technology presents a cost-effective option to realize highly integrated systems for applications such as local multipoint distribution system (LMDS) at 36 GHz, multi-gigabit short range applications at 60 GHz, but also at 77 GHz for high performance long (76–77 GHz) and short (77–81 GHz) range automotive radars, and future emerging RF-imaging applications above 100 GHz.

60 GHz radio has proved growing interest because of the worldwide availability of unlicensed 9 GHz bandwidth. The major drives for commercial applications of 60 GHz radio are SiGe BiCMOS and CMOS technologies. With further down-scaling and accuracy of fabrication, it is expected that the CMOS/BiCMOS technologies may become an alternative solution for circuits and systems implementation at millimetre-wave frequencies and even towards terahertz.

I.4.1 Power divider with in phase outputs

Distributed passive components such as power dividers/combiners, which are used extensively to split or combine power at board level are not considered practical at RF frequencies to be used on a chip because of chip size limitations and cost factors. However, in the mmW range, the wavelength becomes much smaller. With a relative permittivity of about 4-4.2, the dimension of a quarter-wave length TL approximates the 650 μm at 60 GHz. As it is the case for any distributed passive component, the miniaturisation at mmW is a mandatory topic to get low cost devices. Obviously, the size reduction should maintain high level performance to keep highly competitive dividers/combiners.

Table I.3 summarize the state-of-the-art for power dividers at mmW frequencies. In [55], a Wilkinson power divider was developed using asymmetrical shunt-stub and meander-line leading to an ultra-compact device. In [54], the design was based to a slow-wave elevated coplanar waveguide. The area was smaller than the one in [55] but its working frequency is higher, with 60 GHz instead of 45 GHz in [55]. The worst value of the input reflection coefficient S_{11} of the power divider using this technique is -8 dB. Hence matching is poor. Also in [54] 2.3 dB of extra insertion loss (that is to say excluding the theoretical 3-dB power dividing ratio) were measured whereas only 0.9 dB were added in

[55]. The simple meander technique applied in [56] leads to a bigger surface but with only 0.5 dB of insertion loss at 60 GHz. The meander-line associated with a floating defected ground structure in [57] induced 1.5 dB of extra loss with a middle area compared to the other devices.

Ref./Tech.	Freq. (GHz)	Topology	Insertion loss (dB)	Return loss		Isolation (dB)	In 20 % bandwidth				Area (mm ²)
				S ₁₁ (dB)	S ₂₂ & S ₃₃ (dB)		Max. insertion loss (dB)	Return loss		Min. isolation (dB)	
								S ₁₁ (dB)	S ₂₂ & S ₃₃ (dB)		
[54]/90 nm CMOS	60	slow-wave elevated coplanar waveguide	-5.3	-8	-11	-12	-5.3	-6	-10	-11	0.051
[55]/90 nm CMOS	45	asymmetrical shunt- stub and meander-line	-3.9	-21	-15	-19	-4.2	<-13	-14	-15	0.06
[56]/0.13 μ m BiCMOS	60	meander-line	-3.5	-19	-17	-22	-3.7	<-17	<-17	-18	0.12
[57]/0.18 μ m SiGe BiCMOS	60	floating defected grounding structure and meander-line	-4.5	-	-16.5	-21	-4.3	-	-16.5	-19	0.09

Table I.3 : State-of-the-art of power divider around 60 GHz.

Isolation is often desired in order to avoid reflected signals to propagate to other paths in the system. In [55], [56] and [57] the isolation reaches respectively -19, -22 and -21 dB. In [54] isolation is only of -12 dB.

I.4.2 Power divider with quadrature outputs

At mmW frequencies, power-efficient quadrature generation based on a passive approach has been widely adopted in I/Q direct-conversion transceiver, in the radio front-ends of wireless systems, amplifiers, balanced mixers, and vector modulators because of their versatile use. The realization of these couplers requires a large area because of the utilization of quarter-wavelength TLs. Thus, it is essential to reduce the couplers size, which significantly lowers the fabrication costs, keeping low insertion loss and good return loss and isolation.

Table I.4 compares the state-of-the-art in terms of power dividers with quadrature outputs at 60 GHz. The simple branch-line coupler with meandering in [58] adds the least insertion loss with 1.5 dB, induces the best return loss and isolation but is much less compact than the other topologies. Branch-line couplers with modified CPWs are studied in [59] and [60]. The Lange coupler [40] leads to the most compact device with an area of 0.048 mm². The difficulty with coupled lines, as in the Lange coupler, is that high even characteristic impedance Z_{oe} is needed. Values are usually unreachable in silicon technology. In [40] a Thin Film MicroStrip TLs (TFMS) is used. The magnitude imbalance between the outputs is less than 1 dB for any of these power dividers.

Ref./Tech.	Freq. (GHz)	Topology	Max. insertion loss (dB)	Worst return loss at any port (dB)	Isolation (dB)	Magnitude imbalance (dB)	Phase imbalance (°)	Area (mm ²)
[40]/0.13 μ m SiGe BiCMOS	60	Lange coupler with TFMS TLs	5.5	19 (only S ₁₁)	15	1	0.5	0.048
[58]/0.13 μ m SiGe BiCMOS	60	meandering	4.5	20 (only S ₁₁)	25	0.35	1.3	0.28
[59]/90 nm CMOS	60	elevated-center coplanar waveguide	5.5	15	17	0.7	2	0.10
[60]/90 nm CMOS	60	slow-wave coplanar waveguide	6.2	12	25	0.8	0.3	0.083

Table I.4 : State-of-the-art of power divider with quadrature outputs at 60 GHz.

I.4.3 Power divider with out-of-phase outputs

In the RF domain, both active and passive baluns are commonly used. For mmW frequencies, nevertheless, the use of active structures becomes more troublesome as the delay introduced by the transistors yields to a significant negative effect on the phase balance of the balun output. Among passive circuits' solutions, they can be realized with lumped coupled inductors or transformers, or with distributed TL's based circuits. The key issue for CMOS RFICs is the chip area. While in RF, say until one tenth of GHz, the use of transformers is obvious and easy to implement, and on the other hand distributed circuits are size consuming, the situation becomes different when dealing with frequencies of 60-100 GHz and above. The design of the transformers becomes more difficult because of the low efficiency of the coupled inductors, the insertion loss increases and the phase and magnitude imbalance becomes difficult to control. This lumped approach needs the development of very accurate electrical models taking into account all the parasitic elements, in particular the capacitors. On the other hand, the design of TLs is made easier because of less parasitics, and they are well suited for millimetre-wave devices.

Among the TL based baluns, two main structures are prominent: the Marchand balun [61], [62], and the rat-race balun [40] and [63]. Marchand baluns combine two pairs of coupled $\lambda/4$ lines, one of which is open-ended and the two others are shorted. Rat-race baluns, adapted from rat-race couplers, are set by 4 ports in a circular disposition with a total length of $3\lambda/2$. Table I.5 compares the performances of several baluns realized with the main structures.

Ref./Tech.	Freq. (GHz)	Architecture	Return loss (dB)	Isolation (dB)	Magnitude imbalance (dB)		Phase imbalance (°)	Area (mm ²)
					Through	Coupled		
[61]/0.18 μm CMOS	16.5-67	Marchand balun	<-6	-	-7 to -5	-8 to -5	180 \pm 5	0.06
[62]/0.18 μm CMOS	25-65	Marchand balun	<-7	-	-10 to -7	-9 to -6	180 \pm 10	0.55
[40]/0.13 μm SiGe BiCMOS	48-80	Rat-race	<-10	<-18	-5 to -4	-6 to -5	184 \pm 2	0.11
[63]/0.13 μm BiCMOS	57-71	Rat-race	<-14	<-16	-7.5 to -5.5	-6 to -4.5	180 \pm 30	0.28
[64]/0.13 μm CMOS	55-65	Transformer	-	-	-7.5 to -4.5		180 \pm 5	0.05

Table I.5 : State-of-the-art of the baluns at 60 GHz.

I.4.4 Phase shifter

Phase shifters can be active or passive in nature. Active ones can be located in the high or low frequency path of a transceiver. Phase shifters in the low frequency path tend to be more complicated with larger surface area and higher power consumption. In this approach, power consumption is a major concern as it can range from 20 mW to almost 1 W. 60 GHz active phase shifters limit the linearity of the front-end and may be prone to saturation in presence of interferers or jammers and therefore passive designs are preferable.

The passive phase shifter can be classified among three main types: the reflection type, the switched-network approach, and the loaded TLs. The varactors allow the RTPS to have a continuous and accurate variation of the phase. Nevertheless, the low quality factor of the silicon varactors at mmW makes this kind of RTPS really lossy, as high as 7.5 dB for 180° in [65]. The use of lumped MEMS can improve the insertion loss, however, they still remain high with 5.5 dB for only 135° of phase shift as reported in [66]. The switched-network approach consists on switching different delay networks to obtain the required phase delay. In [67] and [68], these networks were composed of simple TL sections. Switched-path type phase shifters are inherently digital, and quickly become cumbersome if a large number of phase states are desired. Devices such as phased arrays often require high resolution in phase control, which would lead to a large and lossy digital phase shift system. Another solution for the reflective network consists on periodically loading a high-impedance TL with MEMS variable (or switched) capacitors [69] or varactors [70]. The phase shift of the loaded line can be controlled by varying the capacitance of each period (or a set of periods). Here again the varactors induce high loss, 12.5 dB for 156° in [70] instead of 3.6 dB for 337° with MEMS. Table I.6 compares more in detail the performances of the discussed phase shifters.

Ref./Tech.	Freq. (GHz)	Architecture	Phase shift (°)	Average insertion loss (dB)	Insertion loss variation (dB)	Return loss (dB)	Return loss over a 10 % BW (dB)	Area (mm ²)	FoM (°/dB)
[65]/130nm SiGe	60	RT Varactor MOS	180	5.85	±1.65	-	-	0.18	24
[66]/quartz substrate	60	RT MEMS	135	4.25	±1.25	-14	-13	3.15	24.5
[67]/quartz substrate	60	SL MEMS	269.2	2.5	±0.5	-13	-12	4	89.7
[68]/90nm CMOS	60	SL without small-size capacitor	360	12.5	±2	<-10	<-10	0.28	24.8
[69]/quartz substrate	65	CPW Loaded MEMs	337	2.8	±0.8	-10	-10	9.45	93.6
[70]/65nm CMOS	60	Differential TL loaded MOS	156	9.25	±3.25	-13	-11	0.2	12.5

Table I.6 : State-of-the-art of phase shifter around 60 GHz.

The maximum FoM of the phase shifters presented herein is about 90 °/dB for [67] and [69]. However, the areas of these two devices are respectively 4 and 9.45 mm² on a quartz substrate which is unacceptable for a simple phase shifter in integrated circuit, even in an interposer type technology with 3D integration. Such surface, and so such cost, will eliminate these solutions for most of the applications. Among the moderate areas, the FoM dramatically decreases down to around 25 °/dB for a maximal phase shift of 180° for RTPS and 360° for switched-network approach.

I.5 Conclusion

The Wilkinson power divider/combiner (in phase), the branch-line coupler (in quadrature) and the rat-race coupler (out-of-phase) has been selected and described because of their efficiency and their popularity among the designers. They were first defined for equal power split and 50 Ω ports impedance loading, but later on, their definition was generalized to arbitrary termination impedances and/or arbitrary power division leading to more freedom for their applications. The reflection type phase shifter, based on branch-line coupler, is also explained and different types of reflection loads are compared. The state-of-the-art is given at RF. The shrinking of these circuits area is an essential topic to get low cost and competitive components, and it is even more pressing when considering integrated technologies like CMOS. Shunt-stub-based artificial and S-CPWs, folding technique, phase inverter, capacitor loading and stepped-impedance are usual ways to reduce the size of the power dividers but also of any circuits using TLs and can be available to both PCB and

silicon technologies. Finally, the state-of-the-art of the presented power dividers and phase shifters working around 60 GHz is given.

It is really difficult to associate compactness, low insertion loss level and low phase/magnitude imbalance at millimetre-wave frequencies for power dividers. In chapter II the S-CPWs are used to design two baluns comprising a phase inverter, a branch-line coupler and a Wilkinson power divider. Design is performed at 60 GHz in order to highlight their potential as passive circuits. Among the various power divider applications: balun, mixing, differential measurement..., feeding circuit for antenna arrays beam-steering attracted our attention because of its structure. It is usually composed of Wilkinson power dividers and reflection type phase shifters which are themselves based on branch-line coupler. Both Wilkinson power divider and reflection type phase shifter face limitations in CMOS technology at millimetre-wave frequencies. The first one needs an isolation resistance in order to work as a combiner but the latter induces unwanted parasitic and coupling, moreover it suffers from a lack of characteristic impedance flexibility. A new solution is proposed in chapter III, first on a PCB technology as a proof of concept and then at 60 GHz in a CMOS technology. The second one does not offer high FoM which means high insertion loss level. In chapter IV two solutions are provided, one in RF on a PCB technology and another one at 60 GHz in a CMOS technology. All the proposed passive devices at millimetre-wave frequencies were achieved with S-CPWs in order to improve performances and compactness.

Chapter II : S-CPW applications

Performance and compactness are extremely important requirements for components design, especially in integrated circuits where performance is limited by the technology and costs are directly linked to the surface area. Many miniaturization techniques, with their impact on the performance, have already been listed and described in the chapter I. Here we are interested in the Slow-wave CoPlanar Waveguide (S-CPW). This topology of transmission line (TL) has been under study for about six years in our laboratory IMEP-LAHC and already proved its great interest, [50] to [53], and [71], to [73]. Its low insertion loss leads to quality factors between 2 and 3 times higher than the classical TL one. Many development steps have been overcome: simulation, de-embedding, parameters extraction, topology optimisation, physical circuit model and realisation of simple circuits. The continuity of this development is now to enlarge the use of this type of TL in more complex microwave passive circuits in order to improve their performances and compactness.

A phase inverter in S-CPW, also presented as a miniaturisation tool in chapter I, was simulated, fabricated and measured. To prove its broadband and compactness benefits, two power dividers for balun application making requirement of a phase inverter were designed and measured. These circuits were realized in the 65 CMOS technology by STMicroelectronics.

In order to cover all the types of power dividers that had been considered in chapter I, the slow-wave technique was also applied to two power dividers with in phase and in quadrature outputs. The circuits are still under fabrication while writing my dissertation, so only the simulation results are shown. The technology involved for those ones is the 55 nm BiCMOS by STMicroelectronics.

At the beginning of this chapter, the simulation tool used for designing the TLs and devices is mentioned and the de-embedding methods applied to the measured TLs, two ports and four ports devices is explained. The performances and dimensions of the simulated and/or measured TLs needed for the devices are presented and gathered according to their back end of line (BOEL).

II.1 Simulation tool

The simulation results of the TLs were obtained thanks to the industry-standard simulation tool HFSSTM provided by ANSYS. This software is a 3D full wave frequency domain electromagnetic field solver based on the finite element method (FEM). HFSS automatically generates mesh and solves Maxwell equations at several nodes of the meshing. A big amount of random access memory (RAM) and long simulation time are

needed, particularly with our structures because of the huge difference between the smallest and the biggest dimensions.

II.2 Calibration & De-embedding

The whole TLs and devices presented in this report were measured at the IMEP-LAHC laboratory with a two ports 110 GHz vector network analyzer (VNA) ME7808C by Anritsu or with a four ports 67 GHz VNA 8510C by Agilent Technologies. The first step of a RF S -parameters measurement consists in calibrating the VNA, before placing the RF probes on the circuit pads. In addition to the correction of the errors associated with the test setup, the calibration step fixes the measurement reference planes. The LRRM (Line Reflect Reflect Match) calibration method was applied because of its accuracy concerning S -parameters until 110 GHz [74]. However, the calibration method does not correct the interconnects parasitics (pads, TLs, tapers...) of the device under test (DUT). Considering the high working frequency and the size of the device compared to the size of the pads, it is mandatory to correct these parasitic effects by another step, named de-embedding, in order to extract rightly the parameters of the DUT, the intrinsic device.

II.2.1 Two port devices

II.2.1.1 Transmission Line

To reduce the influence of the pads and eventually of the interconnects from pads to TLs, the two lines method proposed by Mangan in [75] was applied in this work. To compute de-embedding, two identical TLs of different lengths must be measured ($l_1 > l_2$ for instance). The purpose is then to deduce the ABCD matrix (or transfer matrix) of a fictive TL of length $l_1 - l_2$ from the raw results of the two TLs. This matrix can be written as:

$$\begin{aligned} ABCD_{(l_1-l_2)} &= \begin{pmatrix} A_{(l_1-l_2)} & B_{(l_1-l_2)} \\ C_{(l_1-l_2)} & D_{(l_1-l_2)} \end{pmatrix} \\ &= \begin{pmatrix} \cosh[\gamma(l_1 - l_2)] & Z_c \sinh[\gamma(l_1 - l_2)] \\ \sinh[\gamma(l_1 - l_2)]/Z_c & \cosh[\gamma(l_1 - l_2)] \end{pmatrix} \end{aligned} \quad (\text{II-1})$$

From (II-1), it is then easy to extract the characteristic impedance Z_c and the propagation coefficient γ with equations (II-2) and (II-3).

$$Z_c = \sqrt{\frac{B_{(l_1-l_2)}}{C_{(l_1-l_2)}}} \quad (\text{II-2})$$

$$\gamma = \alpha + j\beta = \frac{\text{arccosh}(A_{(l_1-l_2)})}{l_1 - l_2} \quad (\text{II-3})$$

One advantage of this de-embedding method is that the parasitics from the pads and interconnects do not need to be known or approximated by a lumped-element network. On the other hand, as all the TLs that have to be de-embedded have to be fabricated twice with two different lengths, this method results in a big area.

II.2.1.2 Devices

Concerning the devices, the applied de-embedding principle is explained in Figure II.1. Contrary to the S-matrix, the ABCD matrix offers the advantage of being chained. So the purpose consists in calculating the ABCD matrices of the global device with pads and interconnects (indexed as raw), and the pads and interconnects alone (indexed as pad and TL, respectively). In our work, the used interconnects are TLs. Then, the raw ABCD matrix can be written as in equation (II-4):

$$[ABCD]_{\text{raw}} = [ABCD]_{\text{pad}} \cdot [ABCD]_{\text{TL}} \cdot [ABCD]_{\text{DUT}} \cdot [ABCD]_{\text{TL}} \cdot [ABCD]_{\text{pad}} \quad (\text{II-4})$$

The determination of the ABCD matrix of the interconnects relies on the aforementioned two lines method. The TL ABCD matrix is expressed as in (II-5) with the parameters Z_c and γ extracted thanks to the Mangan method.

$$\begin{pmatrix} \cosh(\gamma L) & Z_c \sinh(\gamma L) \\ \sinh(\gamma L) / Z_c & \cosh(\gamma L) \end{pmatrix} \quad (\text{II-5})$$

The pads are usually modeled by a lumped elements circuit, those elements are determined thanks to a shorted S_{11_short} and an open S_{11_open} pads measurements. Then the ABCD matrices of the pads are determined from their lumped elements equivalent circuits. In our specific case, with the pad dimensions and the considered frequencies below 110 GHz, the open measurement alone is enough to elaborate the model of the pad effect. As the pad is considered as a one port circuit, with the reflection coefficient $\Gamma = S_{11}$ between the probes and the pad, it is easy to deduce the impedance of the pad thanks to the equation:

$$S_{11} = \frac{Z_{\text{pad}} - Z_0}{Z_{\text{pad}} + Z_0} \quad (\text{II-6})$$

where Z_0 is the impedance of the probes, here 50 Ω . The values of Z_{pad} show a capacitance effect. Consequently, the matrix of the pad has the form of a parallel capacitance as:

$$\begin{bmatrix} 1 & 0 \\ 1/Z_{\text{pad}} & 1 \end{bmatrix} \quad (\text{II-7})$$

The raw S-parameters are simply converted to ABCD matrices [12]. The final equation to calculate $[ABCD]_{\text{DUT}}$ with pads and TLs as interconnects is:

$$\begin{aligned}
\begin{bmatrix} A & B \\ C & D \end{bmatrix}_{\text{DUT}} &= \begin{bmatrix} \cosh(\gamma L) & Z_c \sinh(\gamma L) \\ \frac{\sinh(\gamma L)}{Z_c} & \cosh(\gamma L) \end{bmatrix}_{\text{TL}}^{-1} \cdot \begin{bmatrix} 1 & 0 \\ \frac{1}{Z_{\text{pad}}} & 1 \end{bmatrix}_{\text{pad}}^{-1} \\
&\cdot \begin{bmatrix} A & B \\ C & D \end{bmatrix}_{\text{raw}} \cdot \begin{bmatrix} 1 & 0 \\ \frac{1}{Z_{\text{pad}}} & 1 \end{bmatrix}_{\text{pad}}^{-1} \\
&\cdot \begin{bmatrix} \cosh(\gamma L) & Z_c \sinh(\gamma L) \\ \frac{\sinh(\gamma L)}{Z_c} & \cosh(\gamma L) \end{bmatrix}_{\text{TL}}^{-1}
\end{aligned} \tag{II-8}$$

Then, it is easy to convert the ABCD matrix into a S matrix.

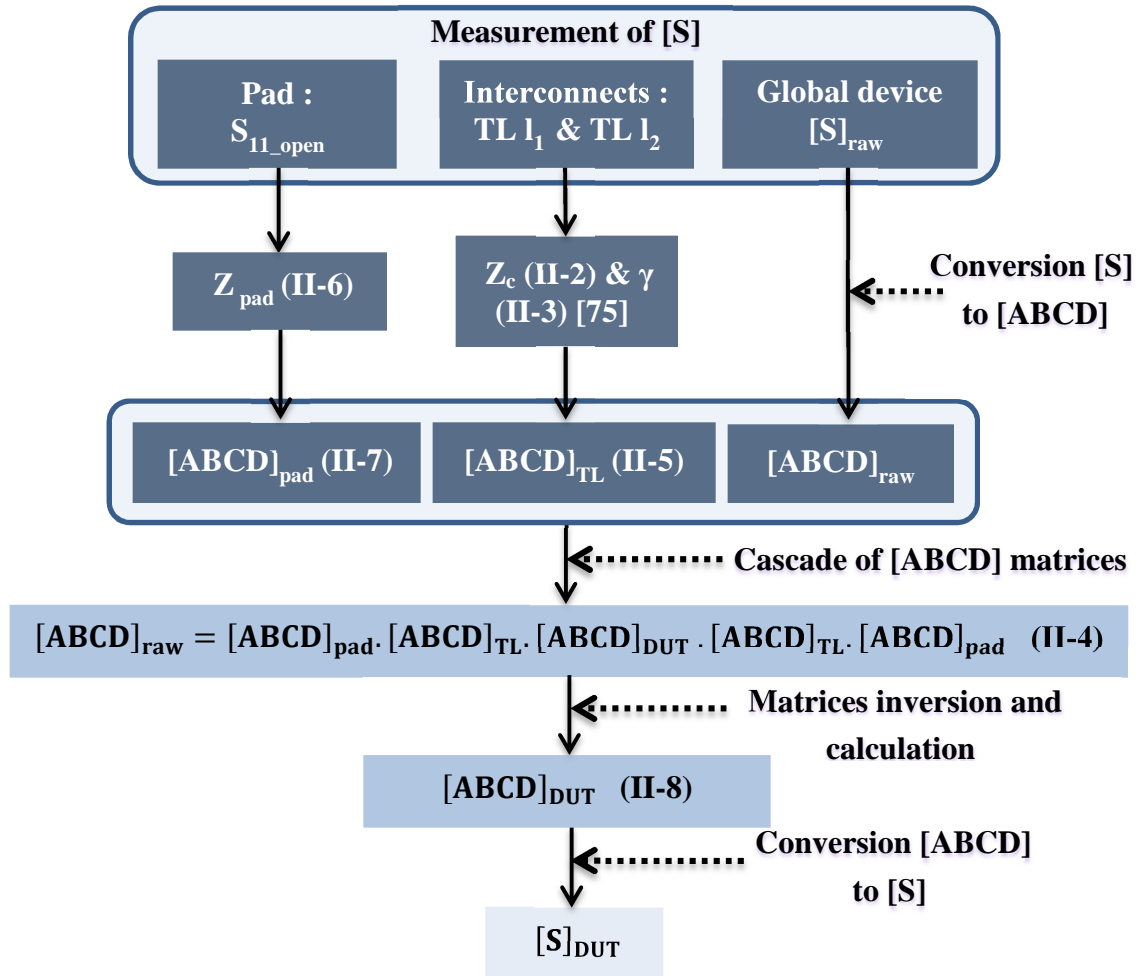


Figure II.1: De-embedding principle for two ports devices.

II.2.2 Four port devices

Concerning the de-embedding of a four ports device, the principle is similar to the 2 ports method except that classical S to ABCD and ABCD to S matrices conversion formulas cannot be directly used since they are consistent only for two ports devices. These formulas have thus been modified involving matrices instead of complex numbers. The

measured parameters of a four port S matrix are gathered in such a way that a two ports matrix is created where the four parameters are not algebraic coefficients but matrices of coefficients, as expressed in (II-9).

$$[S]_{4 \times 4} = \begin{bmatrix} S_{11} & S_{12} & S_{13} & S_{14} \\ S_{21} & S_{22} & S_{23} & S_{24} \\ S_{31} & S_{32} & S_{33} & S_{34} \\ S_{41} & S_{42} & S_{43} & S_{44} \end{bmatrix} = \begin{bmatrix} [S_{11}]_{2 \times 2} & [S_{12}]_{2 \times 2} \\ [S_{21}]_{2 \times 2} & [S_{22}]_{2 \times 2} \end{bmatrix} \quad (\text{II-9})$$

with

$$\begin{aligned} [S_{11}] &= \begin{bmatrix} S_{11} & S_{12} \\ S_{21} & S_{22} \end{bmatrix} & [S_{12}] &= \begin{bmatrix} S_{13} & S_{14} \\ S_{23} & S_{24} \end{bmatrix} \\ [S_{21}] &= \begin{bmatrix} S_{31} & S_{32} \\ S_{41} & S_{42} \end{bmatrix} & [S_{22}] &= \begin{bmatrix} S_{33} & S_{34} \\ S_{43} & S_{44} \end{bmatrix} \end{aligned} \quad (\text{II-10})$$

The equations between the voltage and current used in the ABCD matrix definition (V_n, i_n) and the power waves of the S matrix definition (a_n, b_n) are rewritten as follows:

- For [S] to [ABCD] conversion:

$$\begin{aligned} [A_1] &= \frac{[V_1] + Z_0[I_1]}{2\sqrt{Z_0}} & [A_2] &= \frac{[V_2] - Z_0[I_2]}{2\sqrt{Z_0}} \\ [B_1] &= \frac{[V_1] - Z_0[I_1]}{2\sqrt{Z_0}} & [B_2] &= \frac{[V_2] + Z_0[I_2]}{2\sqrt{Z_0}} \end{aligned} \quad (\text{II-11})$$

- For [ABCD] to [S] conversion:

$$\begin{aligned} [V_1] &= \sqrt{Z_0}([A_1] + [B_1]) & [V_2] &= \sqrt{Z_0}([A_2] + [B_2]) \\ [I_1] &= \frac{[A_1] - [B_1]}{\sqrt{Z_0}} & [I_2] &= \frac{[B_2] - [A_2]}{\sqrt{Z_0}} \end{aligned} \quad (\text{II-12})$$

In both cases $[A_1] = \begin{bmatrix} a_1 \\ a_2 \end{bmatrix}$, $[B_1] = \begin{bmatrix} b_1 \\ b_2 \end{bmatrix}$, $[V_1] = \begin{bmatrix} v_1 \\ v_2 \end{bmatrix}$, $[I_1] = \begin{bmatrix} i_1 \\ i_2 \end{bmatrix}$ and $[A_2] = \begin{bmatrix} a_3 \\ a_4 \end{bmatrix}$, $[B_2] = \begin{bmatrix} b_3 \\ b_4 \end{bmatrix}$, $[V_2] = \begin{bmatrix} v_3 \\ v_4 \end{bmatrix}$, $[I_2] = \begin{bmatrix} i_3 \\ i_4 \end{bmatrix}$. Z_0 is the common port termination, it is an algebraic value.

Therefore, the conventional development to calculate the conversion equations [S] to [ABCD] or [ABCD] to [S] can be applied, paying attention to the matrices properties, as the non-commutability. Thus equations (II-13) and (II-14) are derived:

- For [S] to [ABCD] conversion:

$$\begin{aligned} [A] &= \frac{1}{2} \left(([I_d] + [S_{11}])[S_{21}]^{-1}([I_d] - [S_{22}]) + [S_{12}] \right) \\ [B] &= \frac{Z_0}{2} \left(([I_d] + [S_{11}])[S_{21}]^{-1}([I_d] + [S_{22}]) - [S_{12}] \right) \\ [C] &= \frac{1}{2Z_0} \left(([I_d] - [S_{11}])[S_{21}]^{-1}([I_d] - [S_{22}]) + [S_{12}] \right) \end{aligned} \quad (\text{II-13})$$

$$[D] = \frac{1}{2} \left(([I_d] - [S_{11}])[S_{21}]^{-1}([I_d] + [S_{22}]) - [S_{12}] \right)$$

- For [ABCD] to [S] conversion:

$$[S_{12}] = \left(\left([A] + \frac{[B]}{Z_0} \right)^{-1} + ([C]Z_0 + [D])^{-1} \right)^{-1} \left(\left([A] + \frac{[B]}{Z_0} \right)^{-1} \left([A] - \frac{[B]}{Z_0} \right) - ([C]Z_0 + [D])^{-1}([C]Z_0 - [D]) \right)$$

$$[S_{21}] = 2 \left([A] + \frac{[B]}{Z_0} + [C]Z_0 + [D] \right)^{-1} \quad (\text{II-14})$$

$$[S_{11}] = ([C]Z_0 + [D]) \left([A] + \frac{[B]}{Z_0} + [C]Z_0 + [D] \right)^{-1} \left([A] + \frac{[B]}{Z_0} - [C]Z_0 - [D] \right) ([C]Z_0 + [D])^{-1}$$

$$[S_{22}] = \left([A] + \frac{[B]}{Z_0} + [C]Z_0 + [D] \right)^{-1} \left(-[A] + \frac{[B]}{Z_0} - [C]Z_0 + [D] \right)$$

$[I_d]$ is the identity matrix of the second order. The $[ABCD]_{2 \times 2}$ matrices of the interconnects and pads are obtained as previously explained, then cascaded and combined in order to get only one matrix (pad + interconnect) for each port. After that, these matrices are rearranged into two $[ABCD]_{4 \times 4}$ matrices to be cascaded with the four ports global device matrix. If the ports of the four ports matrix are named p_1, p_2, p_3 and p_4 , the ports of the two ports equivalent device are P_1 (including p_1 and p_2) and P_2 (including p_3 and p_4), as described in Figure II.2.

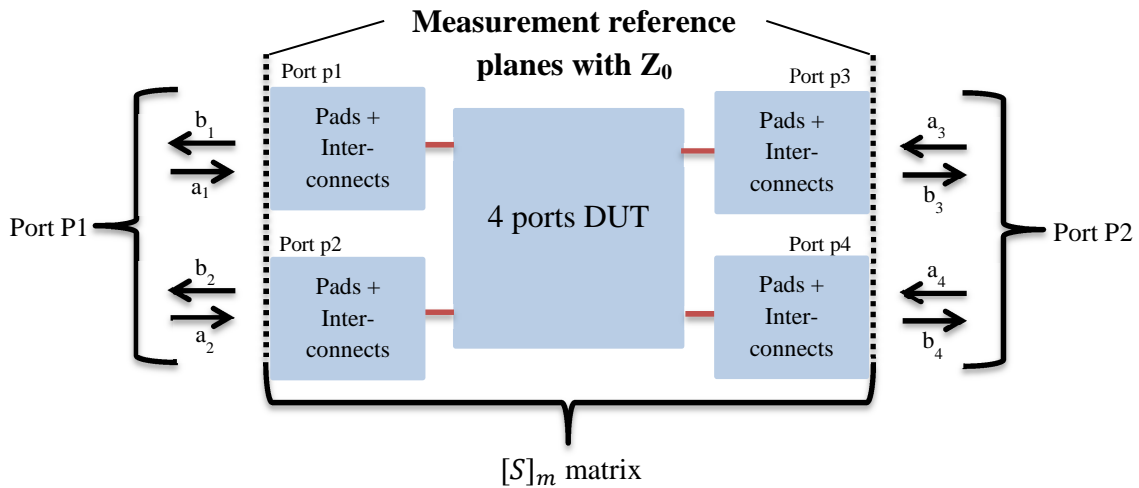


Figure II.2 : Schematic of a four ports device measurement.

The $[ABCD]_{2 \times 2}$ matrix of the pad with interconnects at port number n is:

$$\begin{bmatrix} A_{pn} & B_{pn} \\ C_{pn} & D_{pn} \end{bmatrix} \quad (\text{II-15})$$

If there is no coupling between ports p_1 and p_2 , neither between ports p_3 and p_4 the $[ABCD]_{4 \times 4}$ matrix of the pads with interconnects at port P_1 is:

$$[ABCD]_{P1} = \begin{bmatrix} \begin{bmatrix} A_{p1} & 0 \\ 0 & A_{p2} \end{bmatrix} & \begin{bmatrix} B_{p1} & 0 \\ 0 & B_{p2} \end{bmatrix} \\ \begin{bmatrix} C_{p1} & 0 \\ 0 & C_{p2} \end{bmatrix} & \begin{bmatrix} D_{p1} & 0 \\ 0 & D_{p2} \end{bmatrix} \end{bmatrix} \quad (\text{II-16})$$

and the $[ABCD]_{4 \times 4}$ matrix at port P_2 is:

$$[ABCD]_{P2} = \begin{bmatrix} \begin{bmatrix} A_{p3} & 0 \\ 0 & A_{p4} \end{bmatrix} & \begin{bmatrix} B_{p3} & 0 \\ 0 & B_{p4} \end{bmatrix} \\ \begin{bmatrix} C_{p3} & 0 \\ 0 & C_{p4} \end{bmatrix} & \begin{bmatrix} D_{p3} & 0 \\ 0 & D_{p4} \end{bmatrix} \end{bmatrix} \quad (\text{II-17})$$

If the interconnects are similar, all X_{pn} are equalled with X referring to A, B, C or D.

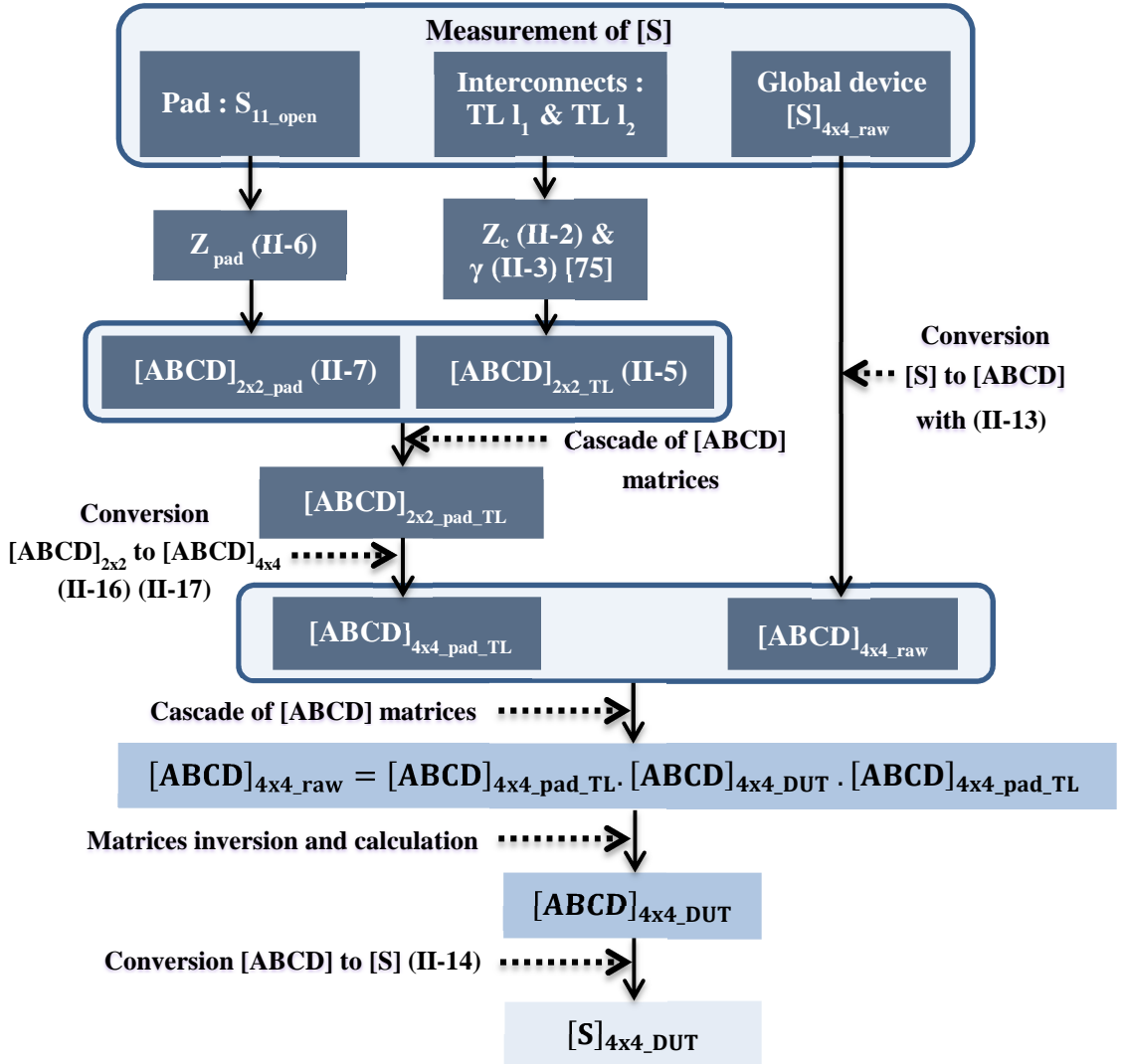


Figure II.3: De-embedding principle for four ports devices.

On the basis of the previous theory, it is now possible to follow the process described in Figure II.3.

II.3 Stacks

The simulated and fabricated components in this report involve three different Back End Of Lines (BEOL) from STMicroelectronics company: the 65 nm and 28 nm CMOS technologies and the 55 nm BiCMOS technology. Figure II.4(a) compares the various stacks and Figure II.4(b) is a SEM (scanning electron microscopy) picture of the 65 nm CMOS technology BEOL by STMicroelectronics, from [76]. In those BEOLs at least three thick metal layers (M6, M7 and Alucap) are available at the upper levels, which have for purpose to decrease the resistive loss. In the 55 nm technology, an eighth level (M8) of very thick metal is even added before the aluminum cap. In the lower levels (between levels M1 and M5) the dimensions significantly decrease in terms of thickness and authorized small widths for metallic paths. The decrease of the metal layers thickness also leads to smaller dielectric thicknesses, and concludes to thin metallic layers closer to the lossy substrate which decreases the quality factor of the passive components built in these layers.

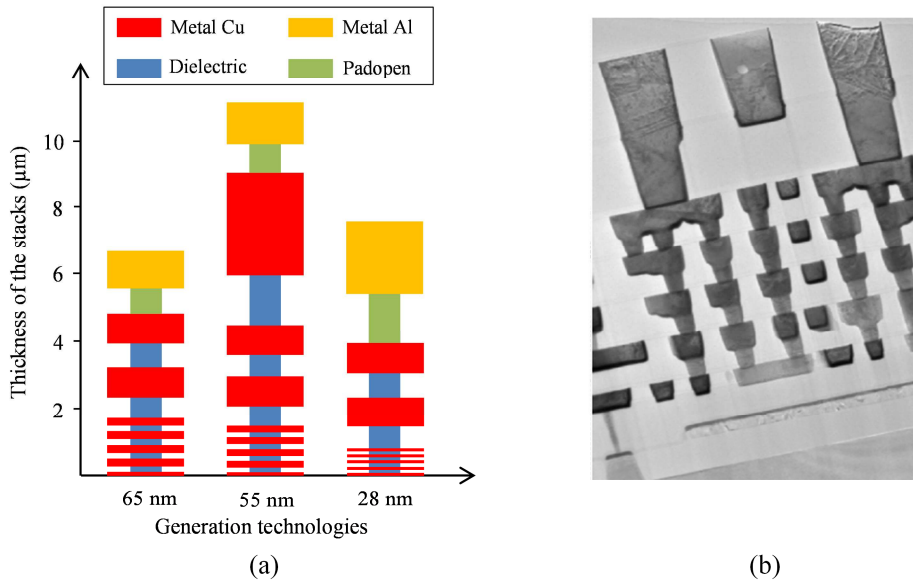


Figure II.4 : (a) Comparison of the STMicroelectronics BEOL stacks used during this work. (b) SEM picture of the 65 nm CMOS technology BEOL from STMicroelectronics [76].

II.4 Simulated and measured transmissions lines

As it was the first time that S-CPWs were realized in these BEOLs, it was important to study the influence of the different available stack configurations. This enabled to, firstly, select TLs with the best quality factors, and, secondly, to measure the TLs further used in the devices in order to verify their characteristics and compare them with the simulation. In the 65 nm CMOS technology, devices composed of S-CPW and microstrip TLs were fabricated and measured. In the 28 nm CMOS and 55 nm BiCMOS technologies,

components with S-CPW were also designed and simulated but the chips containing them are still in the fabrication chain which compels us to present only the simulated results.

II.4.1 Study of the quality factor of the S-CPW in the 65 nm CMOS technology

The characteristic impedance $Z_c = \sqrt{L_l/C_l}$ and the effective relative permittivity ϵ_{reff} of a TL depend on the capacitance per unit length C_l , and so depend on their signal width W . The influence of W is even more significant in the case of S-CPWs because of the high value of C_l . When W increases, C_l increases, leading to the increase of the insertion loss in the floating strips, whereas the series resistance decreases leading to the decrease of the insertion loss in the signal strip. Hence both effects act oppositely. Therefore it is not easy to fix the right W . It is also not easy to determine which stack configuration and dimensions lead to the best compromise α / ϵ_{reff} . In this part, three stack configurations are compared at 60 GHz for S-CPW in the 65 nm technology, the CPW part is respectively simulated in M7, M7-Al and Al layer, as shown in Figure II.5. To make the study easier, the floating strips (FS) level is fixed to M5 layer for all configurations.

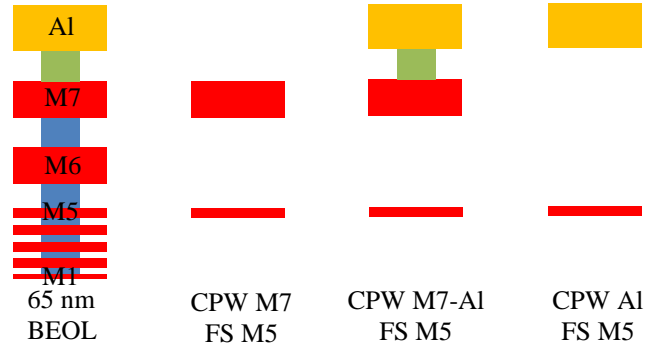


Figure II.5: Compared stack configurations for S-CPWs.

The de-embedding method applied here is the one of HFSS with 15 μm of CPW feeding. First simulations, not reported herein, showed that the quality factor Q increases with the gap G and so with the total width of the TL. However the total width cannot be too large otherwise the physical length saved with the high ϵ_{reff} would be wasted by a too wide TL. This is why the maximal width was fixed to 100 μm . The width of the ground strip was fixed to 12 μm because of design constraint. When the ground is enlarged, there is only a small variation in the characteristic impedance. Figure II.6 gives the effective relative permittivity, the insertion loss and the quality factor versus the characteristic impedance Z_c for the three different stacks and different dimensions, for a total width equal to 100 μm . The shape of the symbols indicates the stack configuration and the colour the dimensions of the TLs. The characteristic impedance range is 38-100 Ω .

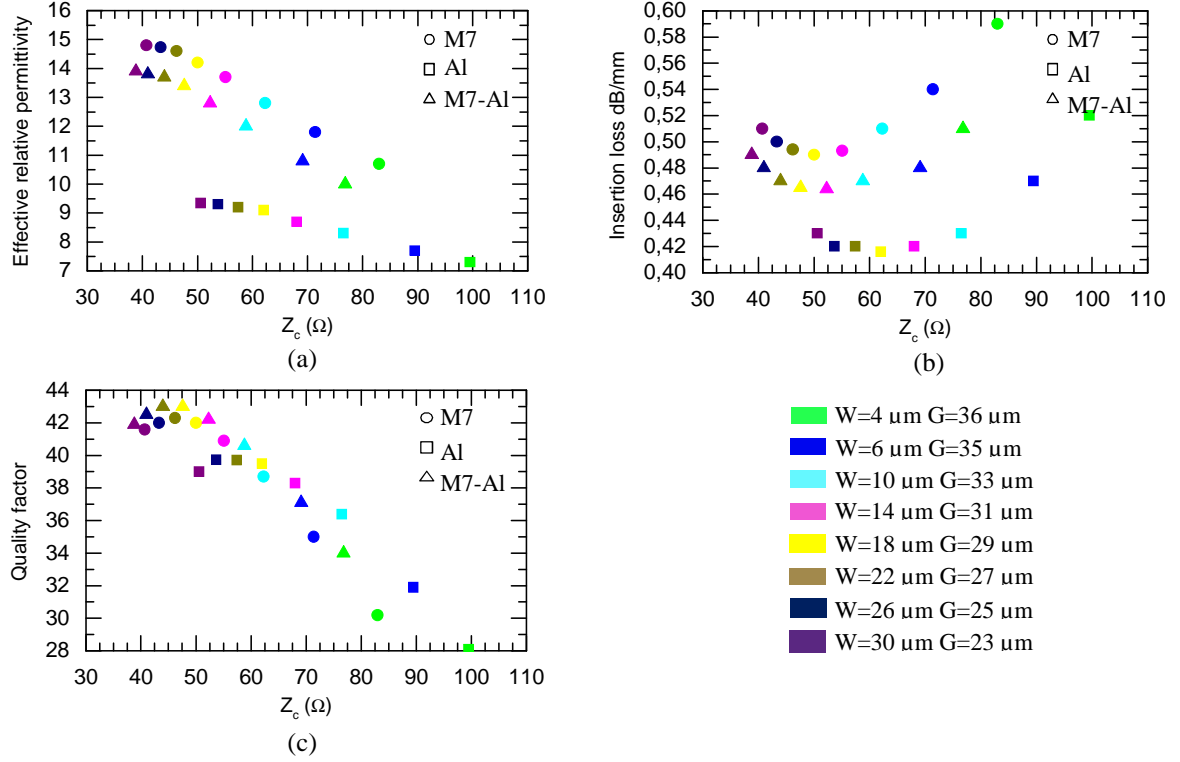


Figure II.6 : Parametric study for three stack configurations. (a) Effective relative permittivity, (b) insertion loss and (c) quality factor versus characteristic impedance.

For each couple of W - G , the CPW in Al layer shows a higher Z_c and a lower ϵ_{eff} , as shown in Figure II.6(a), and a lower insertion loss, as shown in Figure II.6(b). Indeed, there is a greater distance between the floating strips and the ground strips and so a lower capacitance per unit length as shown in Figure II.7(a). Z_c and ϵ_{eff} are slightly shifted for the stack configurations M7 and M7-Al whereas the capacitances per unit length are similar, as shown in Figure II.7(a). The inductance per unit length is however reduced when the Al layer is stacked with M7 as shown in Figure II.7(b) and has for consequence to decrease Z_c and ϵ_{eff} . With the stack M7-Al the insertion loss is lower than with M7 because the series resistance is decreased. As shown in Figure II.6(c), whatever the stack is, an optimal value of Z_c concluding to a maximal value of Q can be found. The highest Q is reached for a CPW in M7-AL level for a Z_c standing between 40 and 50 Ω .

As expected from the theory of electromagnetism, the inductance decreases when the metal stack increases with a stack composed of M7 and Al layers, as shown in Figure II.7(b).

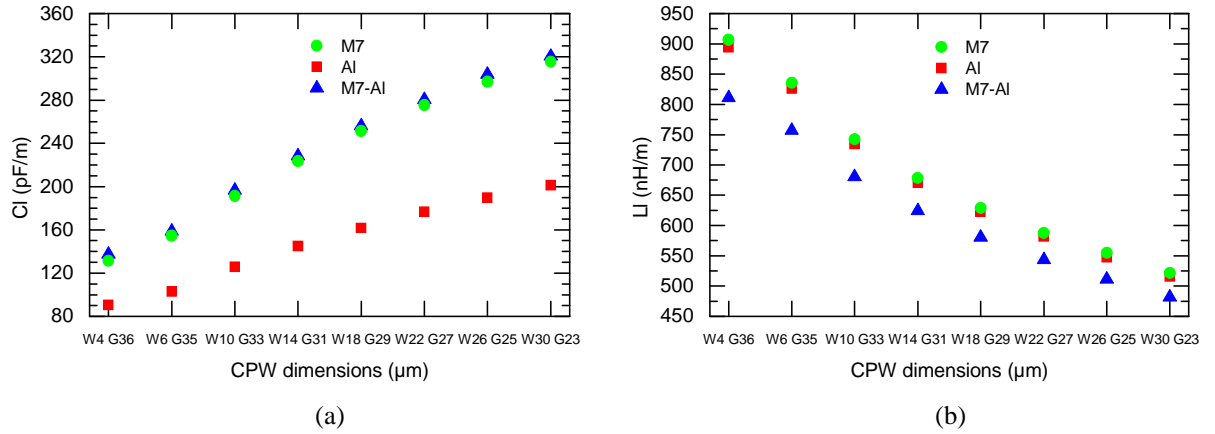


Figure II.7 : (a) Capacitance and (b) inductance per unit length for three stack configurations

II.4.2 Transmission lines in the 65 nm CMOS technology: measurement versus simulation results

II.4.2.1 Microstrip

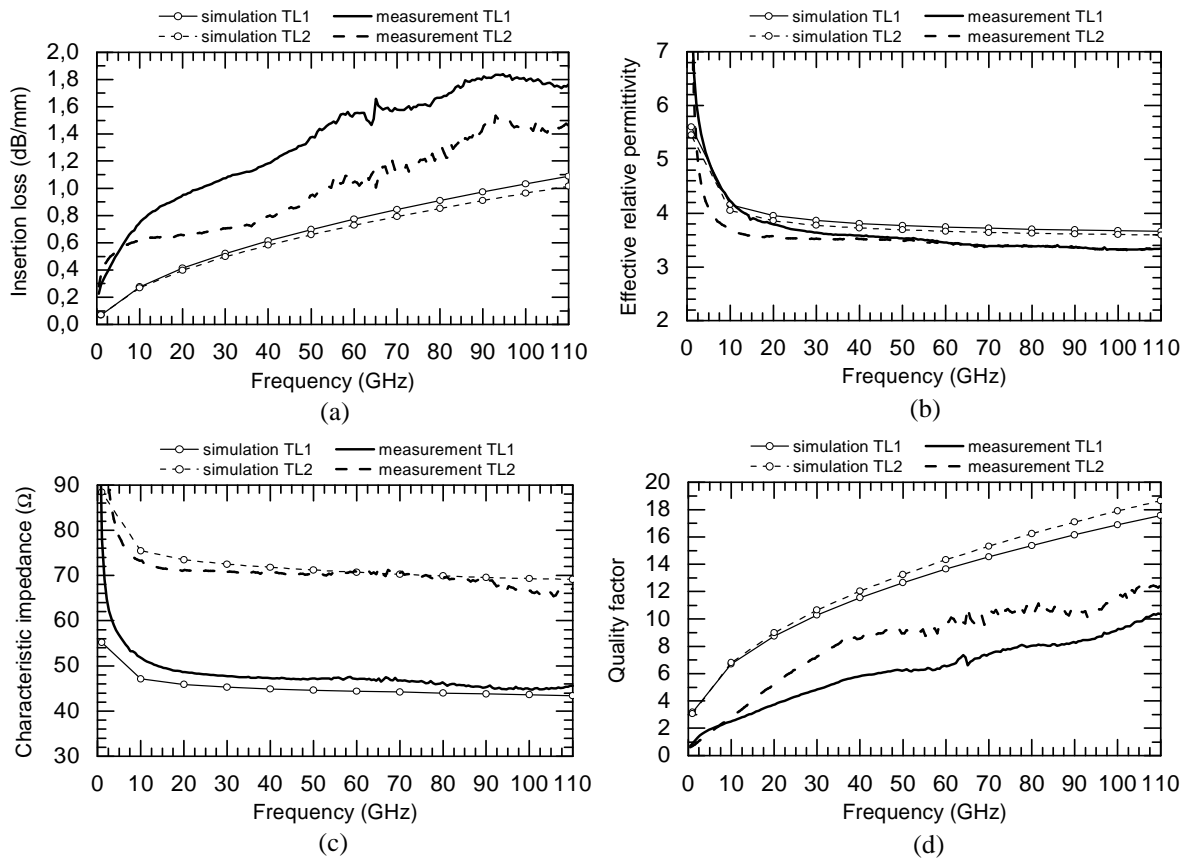


Figure II.8 : Simulation / measurement results comparison for microstrip TLs in the 65 nm technology. (a) Characteristic impedance, (b) effective relative permittivity, (c) insertion loss and (d) quality factor versus frequency.

Two different microstrip TLs were simulated, fabricated and measured, one with a characteristic impedance of 45Ω and $W = 6.2 \mu\text{m}$ in M7-Al (TL1) and one of 70Ω with

$W = 3.8 \mu\text{m}$ in Al (TL2). The comparison between the simulation and measurement results are shown in Figure II.8. The measured parameters fit very well with the simulation, except for the insertion loss which is under estimated by the software tool leading to a measured quality factor lower than expected. The measured effective relative permittivity is about 3.5. The measured quality factor reaches 6 to 9 at 60 GHz

II.4.2.2 S-CPW

Two S-CPWs were also measured, one with $W = 20 \mu\text{m}$, $G = 25 \mu\text{m}$, $W_g = 12 \mu\text{m}$ with floating strips in M5 (TL1) and one with $W = 7 \mu\text{m}$, $G = 31 \mu\text{m}$, $W_g = 12 \mu\text{m}$ with floating strips in M4 (TL2). In both cases the stack configuration of the CPW strips is M7-Al. For all the S-CPWs designed in this work, the floating strip width (SL) was chosen close to the smallest feasible value fixed by the technology and the floating strip space (SS) large enough in order to respect the density rules. Figure II.9 shows the comparison between the simulated and measured parameters.

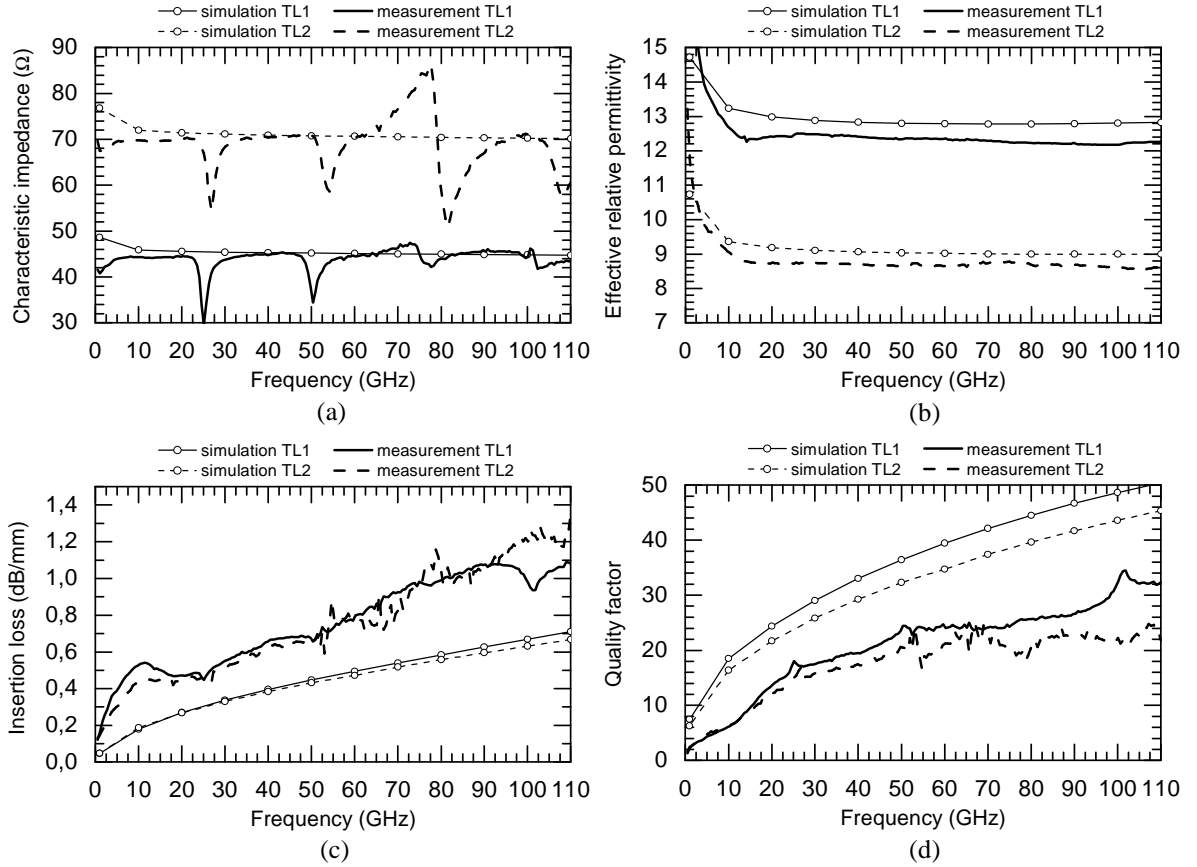


Figure II.9 : Simulation / measurement results comparison for S-CPWs in the 65 nm technology. (a) Characteristic impedance, (b) effective relative permittivity, (c) insertion loss and (d) quality factor versus frequency.

The measured parameters fit well with the simulation, but here again the insertion loss was under estimated in simulations, leading to a lower quality factor in practice. The resonances of the characteristic impedance seen in Figure II.9(a) are due to the electrical length of the TLs which reaches values multiple of $\lambda/2$ because of the high value of the

effective relative permittivity. In the case of the microstrip TLs no resonance appeared because of effective relative permittivity low value.

The measured effective relative permittivity is about 8.4 and 12.3 for the 45 Ω and 70 Ω characteristic impedance, respectively. The measured quality factor is greater than 20 at 60 GHz.

II.4.2.3 Results synthesis

Table II.1 gathers the physical parameters and performances of the measured TLs in both topologies, microstrip and S-CPW, at 60 GHz.

Topology	Z_c (Ω)	Signal stack	Floating strips layer	Dimensions					Performances		
				W (μm)	G (μm)	W_g (μm)	SL (nm)	SS (nm)	E_{reff}	Insertion loss (dB/mm)	Q
S-CPW	45	M7-AL	M5	20	25	12	100	550	12.3	0.78	24
S-CPW	70	M7-AL	M4	7	31	12	100	550	8.4	0.76	21
μstrip	47	M7-AL	-	6.2	Ground plane in M1				3.5	1.55	6.5
μstrip	70.7	AL	-	3.8					3.5	1.05	9.6

Table II.1 : Characteristic and performances of the measured TLs in the 65nm technology at 60 GHz.

The Q factor slightly depends on the characteristic impedance. It reaches 24 and 21 for the 45 Ω and 70 Ω TLs, respectively. In the worst case, measurements show a Q factor at least 2.2 times higher for the S-CPW, as compared to the microstrip lines.

II.4.3 Transmission lines in the 28 nm CMOS technology: simulation results

Table II.2 summarize the physical parameters and performances of the simulated TLs in both topologies, microstrip and S-CPW, at 60 GHz in the 28 nm technology. Because of design constraints, the width of the ground strip was fixed here to 10.8 μm . Three different characteristic impedances were targeted, 35 Ω , 50 Ω and 70 Ω , with both types S-CPW and microstrip. The maximal characteristic impedance reachable in microstrip topology is limited to 65 Ω but it is still close to 70 Ω . The effective relative permittivity of the microstrip TLs is 3.7 whereas it is between 10 and 12 for the S-CPWs. As for the 65-nm technology, the Q factor of the S-CPW type should also be in the worst case 2.2 higher as compared to the microstrip one. The highest Q is reached for a 50 Ω characteristic impedance.

Topology	Z_c (Ω)	Signal stack	Floating strips layer	Dimensions					Performances		
				W (μm)	G (μm)	W_g (μm)	SL (nm)	SS (nm)	E_{reff}	Insertion loss (dB/mm)	Q
S-CPW	36	M7-Al	M5	32	18	10.8	50	450	11.4	0.5	37
S-CPW	50	M7-Al	M5	16	31	10.8	50	450	11.9	0.43	44
S-CPW	70	Al	M5	7	35.5	10.8	50	450	10.3	0.44	40
μstrip	35	Al	-	15	Ground plane in M1				3.7	0.61	17
μstrip	50	Al	-	7.6					3.7	0.64	16
μstrip	65	Al	-	3.6					3.7	0.7	15

Table II.2 : Characteristic and performances of the simulated TLs in the 28 nm technology at 60 GHz.

II.4.4 Transmission lines in the 55 nm BiCMOS technology: simulation results

The physical parameters and performances of the simulated TLs in both topologies, microstrip and S-CPW, at 60 GHz in the 55 nm technology are summarized in Table II.3. The maximal total width of the S-CPW was fixed here to 124 μm , with 12 μm of ground strip width.

Topology	Z_c (Ω)	Signal stack	Floating strips layer	Dimensions					Performances		
				W (μm)	G (μm)	W_g (μm)	SL (nm)	SS (nm)	E_{reff}	Insertion loss (dB/mm)	Q
S-CPW	23	M8-M3	M1	32	34	12	16	64	36.6	1.2	27.5
S-CPW	50	M8-M7	M1	26	37	12	16	64	10.4	0.46	38
S-CPW	83	M8	M5	6	47	12	16	64	8.5	0.5	31
μstrip	26	M8	-	26	Ground plane in M1				3.8	1.01	10.5
μstrip	49	M8	-	8					3.86	1	11.2
μstrip	72	M8	-	2					3.9	1.1	9.1

Table II.3 : Characteristic and performances of the simulated TLs in the 55 nm technology at 60 GHz.

The three targeted characteristic impedances were 23 Ω , 50 Ω and 83 Ω (72 Ω for microstrip), for both types S-CPW and microstrip. It could be possible to reduce the signal width of the 72 Ω microstrip TL in order to get higher characteristic impedance but the insertion loss would increase as well. Indeed W is really thin, equal to 2 μm . Lower values would lead to very high series resistance and high insertion loss. The effective relative permittivity of the 23 Ω S-CPW is 36.6. This value is really high thanks to the stack M8-M3 of the CPW and leads to a strong capacitance per unit length. The drawback is the high level of insertion loss, 1.2 dB/mm, but in spite of that, the quality factor is still 2.6 times

higher as compared to the microstrip TL with the same characteristic impedance. The highest Q factor is still obtained for the $50\ \Omega$ TL.

II.5 Phase inverter

As the phase inverter is an important component which was used in two devices fabricated in the 65 nm technology, it has been simulated and characterized alone. Figure II.10(a) shows the symmetric 3D view from HFSS and Figure II.10(b) the layout of the measured phase inverter. The topology is based on a symmetrical design. The floating strips are on M1, the top branches on M7 and the bottom ones on M6. The wider the overlap between signal and ground conductors at the cross point, the bigger its parasitic capacitor value. Thus, the narrowest width allowed by the technology was used in order to minimize the parasitic capacitor.

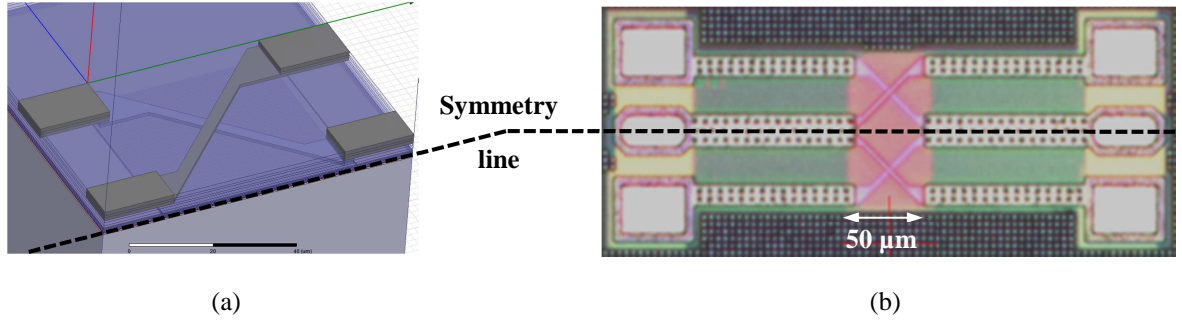


Figure II.10 : (a) 3D symmetrical design and (b) layout picture of the phase inverter.

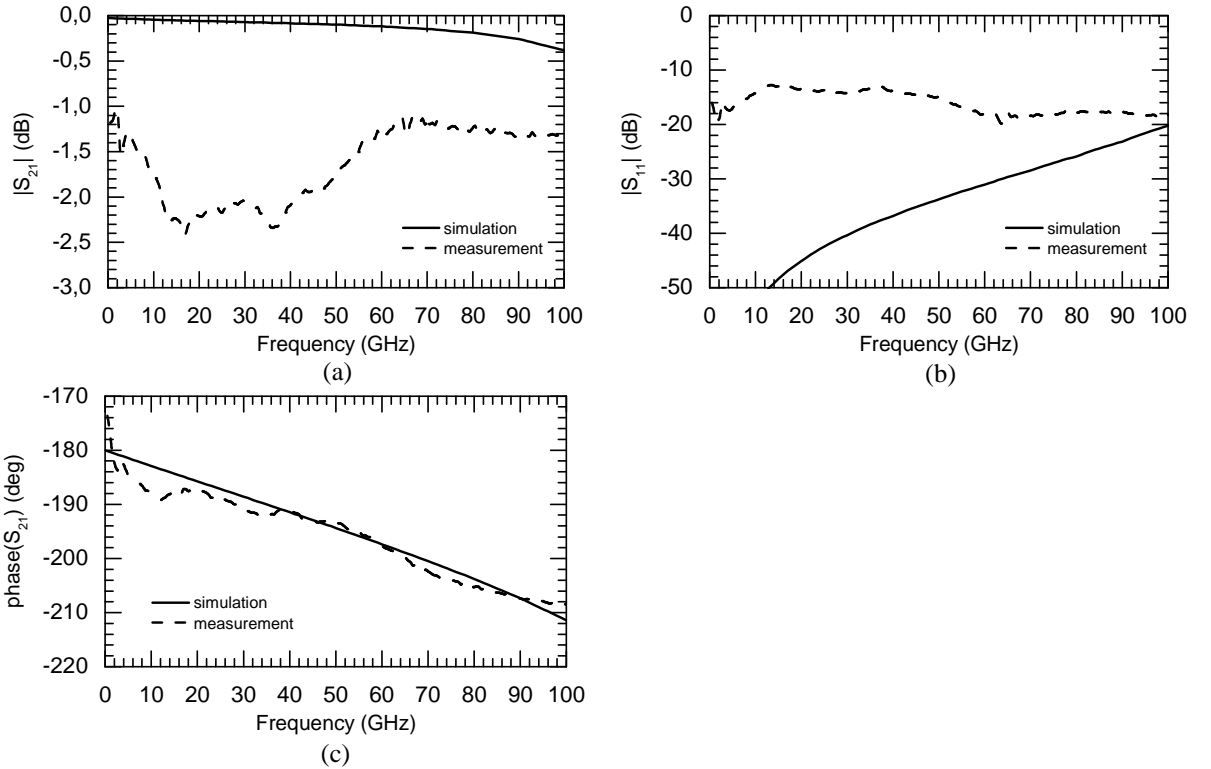


Figure II.11 : Simulation and measurement results of the phase inverter in the 65 nm technology. Magnitude of (a) S_{21} , (b) S_{11} , and (c) phase of S_{21} .

Figure II.11 gives the comparison between the simulated and measured S -parameters. The magnitude of the measured transmission S_{21} and reflection S_{11} parameters are slightly different from the simulated ones. At 60 GHz, measured S_{21} is -1.28 dB and S_{11} , -18 dB. The return loss is better than -11 dB from DC to 100 GHz. Simulation of such device is a real issue because of its physical length which is really small, 50 μm , and seems not long enough to enable the propagating mode to be properly established. However, the measured phase of S_{21} , 198° at 60 GHz, fits well with the simulation. This value is greater than 180° , due to in-out inductive parasitic effects, and the capacitive loading when ground and signal strips are overlapping. If better accuracy of the simulation tool could be reached, the phase inverter could be optimized in such a way to improve the performance of the whole device in which it takes place. Other phase shifters are currently under fabrication with different widths for the TLs at the overlap in order to better understand this component in the future. Also special attention has been paid to the interconnects to be de-embedded.

II.6 Baluns

II.6.1 Rat-race coupler balun

A rat-race coupler working at 60 GHz was designed, fabricated and measured in the 65 nm technology. The design was divided in several blocs simulated individually with HFSS. Then, the S -parameters were all gathered to be simulated thanks to the circuit simulator ADS. As already mentioned in chapter I, in [17], it is reported that an infinite number of electrical lengths exists for the design of a 3-dB hybrid coupler. Whatever the arms characteristic impedance is, below the conventional value of $Z_0\sqrt{2}$, the ring electrical length may be less than 1.5λ . This is very interesting, because the rat-race ring can be shortened, and the characteristic impedance of the S-CPW can be chosen in order to reach the highest quality factor. Moreover, in order to reduce even more the ring physical length, to equate the insertion loss, and to improve the phase imbalance between the two output ports, a phase-inverter was inserted in the longest arm of the rat-race. Figure II.12 gives the rat-race topology. The selected TL for the rat-race ring exhibits a characteristic impedance $Z_c = 45 \Omega$ with $W = 20 \mu\text{m}$ and $G = 25 \mu\text{m}$, with the CPW stack in M7-Al and floating strips in M5. As shown in Figure II.6(c), this stack configuration and characteristic impedance leads to the highest reachable quality factor in this technology. According to [17], considering a 45Ω characteristic impedance, the electrical lengths of the rat-race paths become 52° and 232° instead of 90° and 270° for the conventional topology, respectively. Thus, while choosing the TL with the highest quality factor, not only the rat race will present better loss performances but it will also be miniaturized.

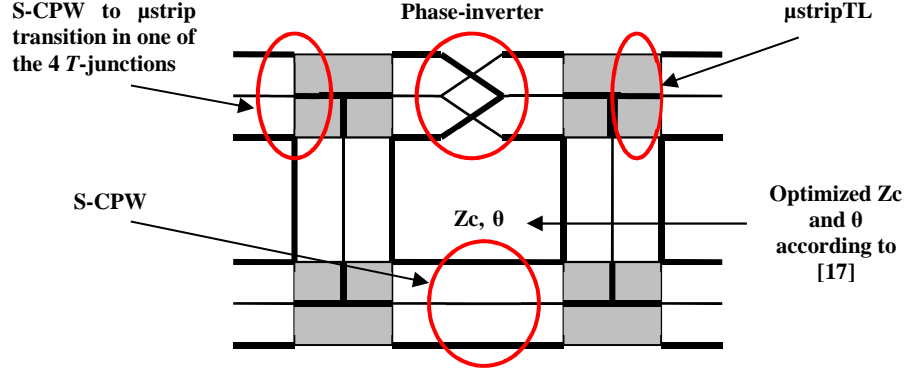


Figure II.12 : Schematic of the rat-race balun

II.6.1.1 Design and layout

Because of the high memory computing needs due to the presence of the very thin thickness and width of the floating strips, the T -junctions based on S-CPWs are heavy to simulate and to optimize with a full-wave simulation tool. In a T -junction of S-CPW, the floating strips placement is problematic and absolutely not obvious. Hence, to avoid errors due to inaccurate simulation results, T -junctions were designed in a microstrip technology, much more easy to simulate. The characteristics of the microstrip TL used were previously presented in Table II.1 and exhibit a characteristic impedance $Z_c = 47 \Omega$. The S-CPW/microstrip transition brings about 0.11 dB of insertion loss at 60 GHz with a very good return loss (S_{11} equal to -28 dB in simulation). The T -junction model was taken into account in the whole rat-race model. Figure II.13 is a picture of the rat-race layout, its dimensions and the different elements are pointed out. The highlighted phase inverter is the one presented before. The main disadvantage of the rat-race when integrated in a CMOS process is that the orientation of the device is limited to only two positions in quadrature. As a consequence the output ports are far from each other and need non-symmetric interconnects towards the next circuit. Non-symmetric interconnects mean different induced insertion loss which is problematic for applications dealing with differential systems.

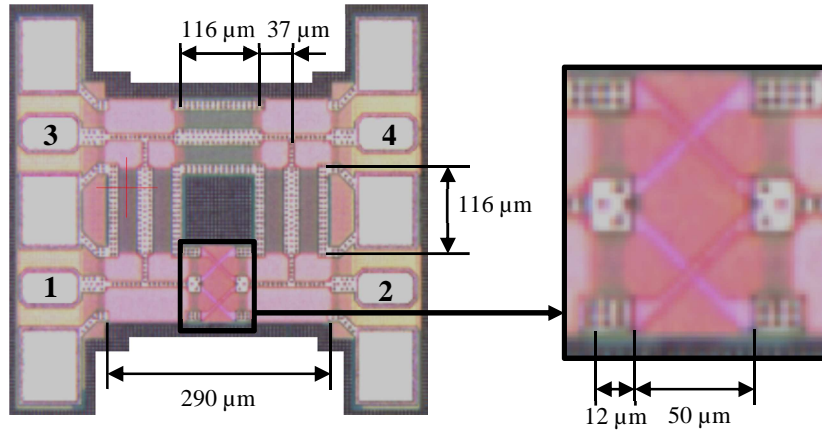


Figure II.13 : Layout of the circuit

II.6.1.2 Simulation versus measurement results

Measurements were carried out from 10 GHz to 67 GHz on a four-ports VNA. The four ports de-embedding method presented above was applied with open pad measurements including the tapers as explained in the section discussing the de-embedding method. Figure II.14(a) compares the simulation (solid line) and measurement (dash line) results. The return loss S_{11} and S_{22} of the measurements show a shift of the working frequency of 8 GHz; indeed the best matching is reached around 67 GHz with -12.5 dB and -20.5 for S_{11} and S_{22} , respectively, instead of -22 dB at 59 GHz for the simulation. The transmission coefficient S_{31} , through the branch without phase inverter, fits well with the simulated one and reaches 4.6 dB, which means 1.6 dB of added losses beyond the theoretical 3 dB. S_{21} , the transmission through the phase inverter is 7.2 dB, that is to say 4.2 dB of added losses. The transmission parameters are robust with very flat curves. With a bandwidth defined by considering a return loss better than -10 dB, and a working frequency centred at 67 GHz, a minimum of 15 % is obtained by symmetry of the measured result at 67 GHz (between 62 GHz and 72 GHz minimum). A measurement till 110 GHz may confirm this assumption. Isolation S_{32} is better than -23 dB over a very large frequency band, at least from 10 GHz to 67 GHz. Figure II.14(b) shows a phase difference centred around 185° with a phase imbalance of $\pm 1^\circ$ between 32 GHz and 67 GHz or $185.5 \pm 0.5^\circ$ between 62 GHz and 67 GHz which is excellent in comparison to the state-of-the art. This result is clearly obtained thanks to the use of the phase inverter, because its phase does not vary with frequency, leading to an equivalent phase shift for the rat-race branches over the frequency. There is a shift of 5° compared to the perfect phase imbalance, but it is very flat over the whole bandwidth. 5° is easy to overcome thanks to TL length readjustment in a second run. Finally, the chip is compact with an area equal to 0.085 mm^2 .

- How to explain the discrepancies?

The simulated microstrip and S-CPWs of the rat-race have small electrical lengths, and we noticed afterwards that the S -parameters of such small lengths obtained with HFSS were not right, leading to an inaccurate estimation of the TLs effective relative permittivity. This comes from an un-established propagating mode when considering small-length TLs. However, this error could be easily corrected. As shown above, simulation and measurement results of the TLs characteristic parameters fit really well, and hence could be used for the design of a second set of rat-race baluns.

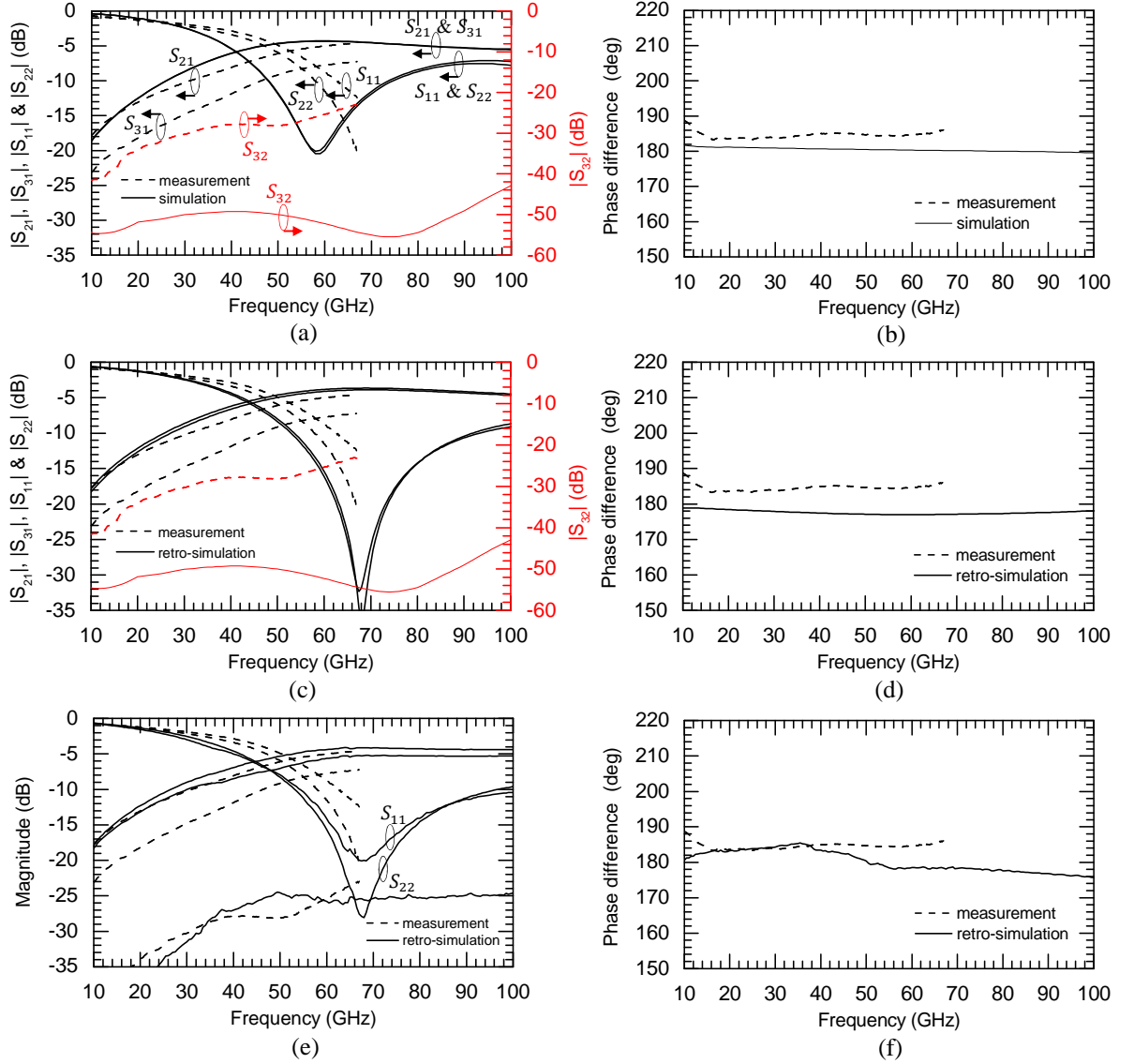


Figure II.14 : S -parameters for measurements and (a)-(b) simulation, (c)-(d) first retro-simulation and (e)-(f) second retro-simulation.

A comparison between the measurement results and retro-simulation is shown in Figure II.14(c) and (d), where the S -parameters blocs of the TLs were replaced by equivalent TLs with the parameters Z_c , ϵ_{reff} and α determined from the measurements results. The S -parameters of the phase inverter from HFSS simulator were kept. The return loss S_{11} and S_{22} of this retro-simulation show a good fitting of the centre working frequency with the measurement results, at 67 GHz (Figure II.14(c)). The phase difference is kept flat and is 177.1° at 67 GHz, as shown in Figure II.14(d). The matching is improved because in this retro-simulation the microstrip/S-CPW transitions were not taken into account. If now the S -parameters bloc of the simulated phase inverter is replaced by the measured phase inverter bloc, the curves shown in Figure II.14(e) and (f) are obtained. The return loss S_{11} containing a branch connected with the phase inverter is degraded compared to the S_{22} which does not contain any branch with phase inverter, as shown in Figure II.14(e). The

effects of the phase inverter are here highlighted. S_{32} is also degraded and gets closer to the measurement result. Finally the simulated insertion loss S_{31} increases up to 5.2 dB.

II.6.1.3 Further improvements

The method consisting in simulating the TLs with their real lengths and taking their S -parameters in a circuit simulator does not work in our case because of the really small physical lengths. Equivalent TLs have to be used in the circuit simulator with the parameters obtained from HFSS simulation with long enough physical lengths.

The phase inverter has a strong effect on the rat-race balun performances. In order to get better performances, the S -parameters magnitude of the phase inverter has to be better simulated in order to allow an accurate optimization. With the measurements of the different phase inverters upcoming soon, we should better understand the influence of the parasitics induced by the overlap. Special attention has been paid to the future de-embedding procedure for these phase inverters. Moreover, it could be possible to replace the CPW phase inverter by a microstrip type to avoid the use of really short S-CPW. In that case all the TLs between ports 1 and 2 of the rat-race would be of a microstrip type.

II.6.2 Power divider balun

A new topology of balun has been tested out: it is a classical $\lambda/4$ power divider in which a phase inverter was inserted in one branch to get 180° of phase difference between the two output ports. The isolation resistance R used in the Wilkinson power dividers must be removed, otherwise the 180° relative phase difference would increase considerably the losses. Removing this resistance, this topology cannot be used anymore as a combiner because isolation and output ports matching are degraded. This balun was fabricated and measured in the 65 nm technology on the same chip as the rat-race balun presented above. The layout with the dimensions is given in Figure II.15.

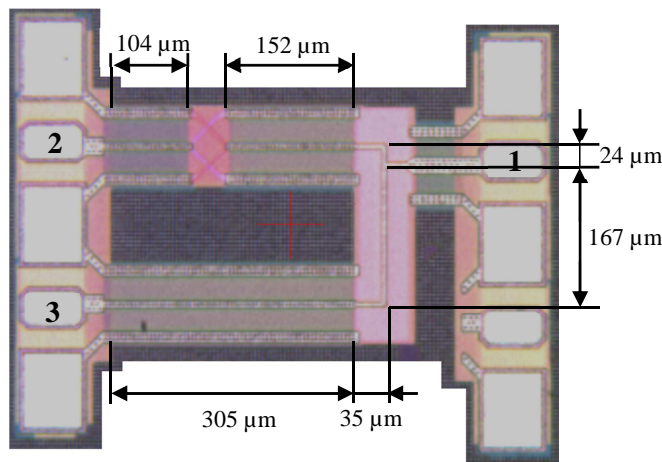


Figure II.15 : Layout of the power divider balun

As for the conventional Wilkinson power divider, the characteristic impedance of the TLs is 70Ω with 90° electrical length. The characteristics of the microstrip and S-CPWs used in this design were presented in Table II.1. The main advantage of this topology compared to the rat-race balun is the proximity of the two output ports. The input port was placed in such a way that the outputs are at the same level with a phase of S_{21} and S_{31} equal to 90° and 270° , respectively. In that case, a good matching at port 1 and 180° of phase difference should be obtained.

The design method is the same as for the rat-race balun. TLs, S-CPW/microstrip transitions and phase inverter were simulated with HFSS to get the S -parameters, and then gathered in ADS to simulate the whole device.

II.6.2.1 Simulation versus measurement results

Measurements were carried out from 10 GHz to 67 GHz. The same four ports de-embedding method as the rat-race balun was applied. Figure II.16 compares simulation and measurement results. The return loss S_{11} resonance was shifted towards a lower frequency with a down step of 7 GHz, as shown in Figure II.16(a). The best matching is -43 dB at 53.3 GHz instead of 60 GHz. However, the matching is still equal to -20 dB at 60 GHz. S_{21} and S_{31} equal -4.3 dB and -3.6 dB, respectively. The phase difference is 173° , as shown in Figure II.16(b).

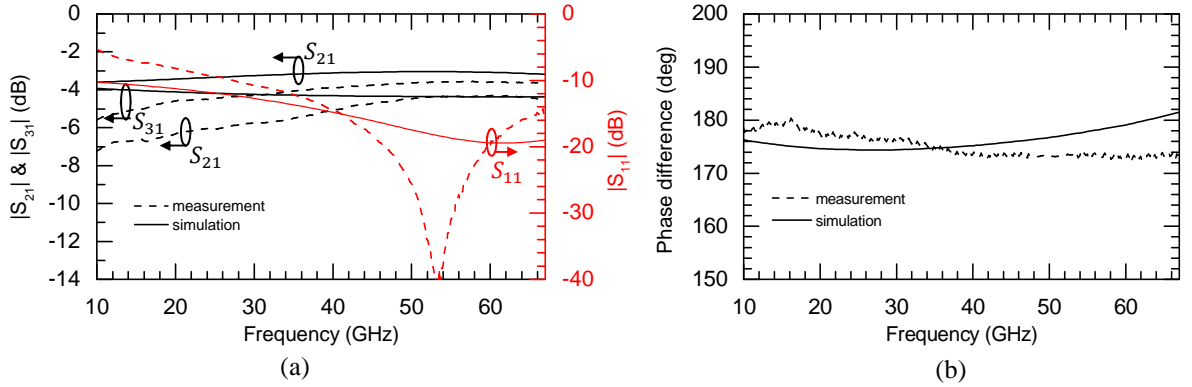


Figure II.16 : Simulation and measurement results of the power divider balun in the 65 nm technology.
(a) Magnitude and (b) phase difference.

The simulation of the transmission coefficients shows that S_{21} , through the phase inverter, should have less insertion loss than S_{31} along a long lossy microstrip TL. That is to say that the simulation of the basic components erroneously indicates lower insertion loss due to the phase inverter than to the microstrip TLs. The measured results, on the contrary, clearly show that S_{21} is higher than S_{31} . We already discussed about the high insertion loss added by the phase inverter and the complexity to simulate it. Despite that, S_{21} and S_{31} were measured at -4.4 dB and -3.6 dB at 53 GHz, which are really good results. The difference of magnitude between S_{21} and S_{31} is also due to impedance mismatch seen from the input port. The phase inverter acts as a stepped impedance creating a discontinuity

for the signal between ports 1 and 2. The relative bandwidth centred at 53 GHz satisfying a -20 dB return loss reaching 25 % (between 46.5 GHz and 60 GHz). In this band the phase difference is 173.5° , e.g. a discrepancy of 6.5° as compared to the targeted 180° . However it is really flat since the phase imbalance is only $\pm 0.4^\circ$. S_{21} varies from -4.64 dB to -4.31 dB and S_{31} from -3.72 dB to -3.56 dB. The area equal to 0.1 mm^2 is bigger as compared to the rat-race balun (0.085 mm^2). This directly stems from the output ports position which was adjusted to fit with the RF probes (in order to avoid extra connection TLs and to simplify the de-embedding). The TLs could be designed closer from each other and would decrease the surface area of at least 25 %. Even though the design method was the same as for the rat-race balun, here no problem occurred because of an eventual misestimating of the TLs effective relative permittivity. Indeed, the simulated TLs are longer, and so, long enough for their propagation mode to be well established and their simulation to be accurate.

II.6.2.2 Further improvements

The mismatch due to the phase inverter slightly shifts the working frequency. With shorter TLs and better adjustment, the working frequency and the phase difference could be improved. Moreover, a study of the position of the phase inverter in the branch could lead to an optimised position.

II.6.3 Comparison with the state-of-the-art

The Table II.4 compares the measurement results of the two topologies of baluns with the state-of-the-art of power divider with out-of-phase presented in Chapter I.

Ref./Tech.	Freq. (GHz)	Architecture	Return loss (dB)	Isolation (dB)	Magnitude imbalance (dB)		Phase imbalance ($^\circ$)	Area (mm^2)
					Through	Coupled		
[61]/0.18 μm CMOS	16.5-67	Marchand balun	<-6	-	-7 to -5	-8 to -5	180 ± 5	0.06
[62]/0.18 μm CMOS	25-65	Marchand balun	<-7	-	-10 to -7	-9 to -6	180 ± 10	0.55
[40]/0.13 μm SiGe BiCMOS	48-80	Rat-race	<-10	<-18	-5 to -4	-6 to -5	184 ± 2	0.11
[63]/0.13 μm BiCMOS	57-71	Rat-race	<-14	<-16	-7.5 to -5.5	-6 to -4.5	180 ± 30	0.28
[64]/0.13 μm CMOS	55-65	Transformer	-	-	-7.5 to -4.5		180 ± 5	0.05
This work	62- >67	Rat-race	<-10	<-23	-7.56 to -7.24	-4.87 to -4.62	185.5 ± 0.5	0.085
This work	46.5-60	Power divider with phase inverter	<-20	-6	-4.64 to -4.31	-3.72 to -3.56	173.5 ± 0.4	0.1

Table II.4 : Comparison of this work with the state-of-the-art.

II.7 Branch-line coupler

A branch-line coupler with -3 dB at each output port for 50- Ω system characteristic impedance was designed in the 28 nm technology at the working frequency of 60 GHz. Only the simulated results are presented here. The vertical TLs have a characteristic impedance of 35 Ω and the horizontal ones of 50 Ω . 50 Ω microstrip feeding lines connect the pads to the input/output ports of the branch-line, as shown on the layout in Figure II.17. These feeding lines and pads will be easily de-embedded thanks to the method described above.

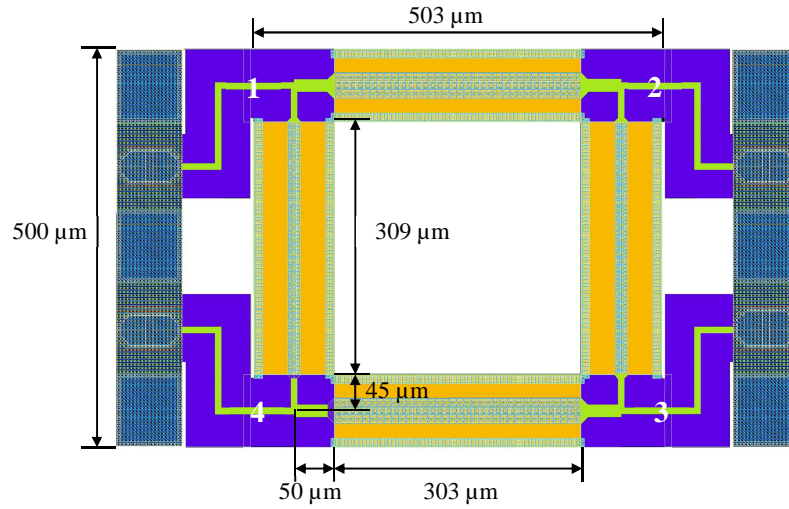


Figure II.17 : Layout of the branch-line coupler with S-CPWs in the 28 nm technology.

The simulated performances of the S-CPW and microstrip TLs used in this device have been summarized in Table II.2. Here again the T -junctions were designed in a microstrip technology to simplify simulations and layout design. To simulate the full device, equivalent TLs on ADS were modelled with the parameters Z_c , ϵ_{reff} and α , the attenuation loss. All the parameters were determined previously thanks to HFSS. The S-CPW/microstrip transitions were considered as perfect, which means that the equivalent TLs were directly and ideally connected in the circuit simulator. The simulated results are shown in Figure II.18. The S -parameters correspond to the ports number according to their position in the device, which means that pads and 50 Ω feed lines were not taken into account in the simulations.

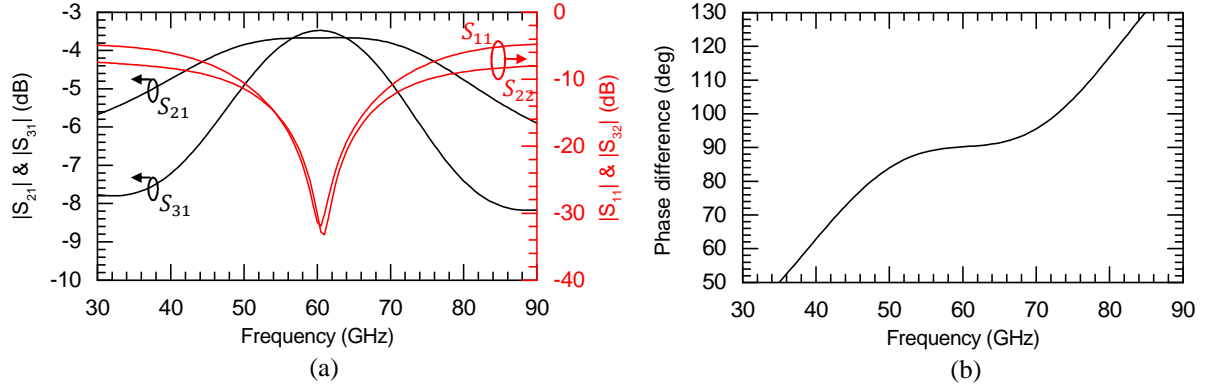


Figure II.18 : Simulation results of a branch-line coupler with S-CPWs in the 28 nm technology.
(a) Magnitude and (b) phase difference.

At 60 GHz, the return loss is -28 dB and the transmission coefficients S_{21} and S_{31} are respectively -3.67 dB and -3.48 dB, as shown in Figure II.18(a). The device has two symmetry axes, vertical and horizontal, so the return loss parameters are similar at all ports. The isolation between ports 1 and 4, S_{41} , is -30 dB. The bandwidth determined with a return loss better than -20 dB reaches about 12 %, between 57 GHz and 64 GHz. Over this bandwidth S_{21} is constant and S_{31} varies between -3.48 and -3.68 dB, so the maximal magnitude imbalance is 0.19 dB. The variation of S_{31} is less flat than the variation of S_{21} because the electrical length between ports 1 and 3 is 180° and only 90° between ports 1 and 2, so the narrow band effect of the TLs is consequently stronger for S_{31} . The phase difference is 90.2° at 60 GHz and between 89.6° and 91° in the bandwidth, which means a phase imbalance of $\pm 0.7^\circ$, as shown in Figure II.18(b). The TLs were not placed in a configuration to optimize the device area, leading to a surface of 0.252 mm^2 . In order to reduce the surface area, it could be possible to meander the TLs by using the free space in the middle of the device.

II.8 Power divider

A power divider was designed in the 28 nm technology to be used at 60 GHz. The layout is presented in Figure II.19. No resistance was placed between the two output ports, hence it was not realized a Wilkinson power divider. In CMOS technology the resistance dimensions are really small and the S-CPW width quite large (around $100 \mu\text{m}$) so that long interconnects were needed between the S-CPW signal strip and the resistance which leads to a strong inductive effect. As it is really difficult to simulate and estimate this parasitic effect, the isolation resistance was removed. Obviously this has for consequence to limit the use of this device as a power divider only. A $40\text{-}\mu\text{m}$ long 50Ω microstrip feed line was inserted between the pad at port 1 and the T -junction. Same feed lines were used for output ports 2 and 3. Then 65Ω microstrip TLs connect this T -junction to the 70Ω S-CPWs. The minimal allowed width and the highest distance h (between the ground and the signal strip) were fixed for the microstrip topology to get the maximal possible impedance, which is

only of $65\ \Omega$. The equivalent TLs modelled with the parameters Z_c , ϵ_{reff} and α given in Table II.2 were ideally connected, without S-CPW/microstrip transition equivalent electrical model.

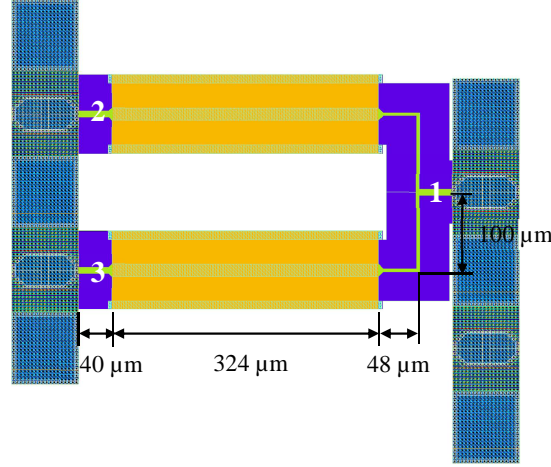


Figure II.19 : Layout of the Wilkinson power divider with S-CPWs in the 28 nm technology.

Figure II.20 shows the magnitude of S_{11} , S_{22} , S_{21} and S_{32} . The circuit has horizontal symmetry axis so that $S_{22} = S_{33}$ and $S_{21} = S_{31}$. The return loss is really good with -44 dB at 60 GHz. Using $65\ \Omega$ characteristic impedance instead of $70.7\ \Omega$ shifted the working frequency of 3 GHz towards the lower frequencies. This was corrected by adjusting the electrical length of the S-CPWs in order to reach a 60-GHz working frequency. By this way, the working frequency is centred with a total electrical length of 84° instead of the theoretical 90° between the input and output ports. Moreover, as the error is only 8 % on the characteristic impedance and as the electrical length of the $65\ \Omega$ microstrip line is small, 21° among 84° , the device keeps an excellent matching. As expected, with no isolation resistance, the isolation and matching of the output ports are only -6.4 dB. The bandwidth determined with a return loss better than -20 dB reaches 40 % (between 48 GHz and 72 GHz). Over this bandwidth, the transmission coefficients S_{21} and S_{31} vary between -3.35 dB and -3.28 dB. The surface area of the power divider is $0.12\ \text{mm}^2$. As for the power divider balun, the output ports were adjusted to fit with the RF probes. With closer TLs the surface could be decreased of at least 25 %.

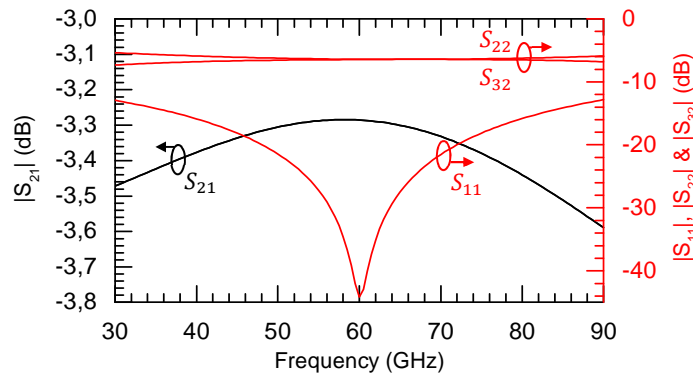


Figure II.20 : Simulation results of a Wilkinson power divider without isolation branch, with S-CPWs in the 28 nm technology.

II.9 Conclusion

In this chapter, S-CPWs were used to realize several devices. The slow-wave TL combines high effective relative permittivity and high quality factor, and lead to compact and performing devices having low insertion loss. Even though for high characteristic impedances the quality factor decreases, S-CPWs can be designed to reach a $100\ \Omega$ characteristic impedance, with a simulated quality factor of 28 in the 65 nm technology. With microstrip type TLs, the maximal characteristic impedance is limited to about $70\ \Omega$ (the poorer case is $65\ \Omega$ only in the 28 nm technology). However, microstrip TLs are still needed, for the T -junctions for example, as S-CPW junctions are still complicated to design due to the floating strips.

A phase inverter was fabricated and measured in the 65 nm technology. It is very wide band and strongly reduces the area of the devices in which it is inserted. Even if the phase of the transmission coefficient is well determined with HFSS, the magnitude is not well predicted. With more accurate simulations, it could be optimized in order to reduce the insertion loss. Based on this phase inverter, two baluns using S-CPWs were achieved in the 65 nm technology at a 60 GHz working frequency. The first one was based on a rat-race. It exhibited good isolation and matching. The second one was carried out by a novel topology based on a power divider with close output ports but without isolation. They exhibit a surface area of $0.085\ \text{mm}^2$ and $0.1\ \text{mm}^2$, respectively. 25 % of surface area could be saved for the power divider balun without fitting the feed lines with the RF probes. Optimised surfaces would reach the state-of-the-art presented in chapter I in terms of miniaturization. The design method used in this work was not suitable for the rat-race and leaded to a shift of 8 GHz towards the higher frequencies. Moreover, the phase inverter degraded the insertion loss in both circuits.

Then, a branch-line coupler and a power divider (without isolation) were simulated in the 28 nm technology. A design method with equivalent transmission lines characterized with the parameters Z_c , ϵ_{reff} and α , obtained from HFSS and validated by the measurements, was applied. Really good performances are expected at 60 GHz. Also, de-embedding methods are given for two ports devices and transmission lines, and for four ports devices.

The devices designed in this chapter proved that the slow-wave transmission lines have a strong interest for the design of compact and low-loss passive devices at millimetre-wave frequencies.

The applications of the power divider designed in the 28 nm technology are limited because of the lack of good matching at the output ports and the lack of isolation. However, despite the constraints of the isolation resistance and its access in silicon technology, it is important to develop fully matched and isolated power dividers for combiner applications.

In the next chapter a new topology of power divider is proposed to design and optimise such power dividers.

Chapter III : New type of power divider based on a Wilkinson power divider/combiner for millimetre-wave frequencies applications

This chapter focuses on the design, development, realization and test of a new type of power divider based on the Wilkinson power divider. This new power divider is intended to be further implemented in a feeding network system for antenna array beam-steering. At the beginning, the original Wilkinson power divider was designed for use in shielded coaxial systems at frequencies low enough not to take into consideration additional parasitic effects. Design complexity arises when dealing with millimetre-wave bands in planar technologies. Parasitics typically derived from undesired coupling between the two quarter-wave arms, or distributed effects introduced by the physical requirements, such as the stretching of the resistance between the two arms in IC's, inhibit performances. This is most of the time not an issue at RF frequencies, but it becomes particularly troublesome at high frequencies.

The Wilkinson power divider faces another issue in silicon technology which is the characteristic impedance limitation. Indeed, it is fixed by the BEOL and the design rules of the considered technology so that it may be not possible for the microstrip type TL to reach the $70.7\ \Omega$ characteristic impedance required in a $50\text{-}\Omega$ system.

As already mentioned in this thesis, miniaturization is an unavoidable topic, particularly for integrated circuits, due to the high cost. Some of the techniques given in the first chapter are really efficient and could be reused, such as the stub loading technique. By using a procedure comparable to Mandal's optimization of the rat-race coupler, described in [17], we will see that many solutions are available (among which the original Wilkinson power divider), so that it becomes very easy by the end to compare one solution to another and to choose the most appropriate for our purpose: lower characteristic impedance or reduced area, or a compromise of both.

Hence, in this chapter a new topology of power divider/combiner with in phase outputs is proposed. Our study shows that compactness and high-performance can be met simultaneously, with high flexibility thanks to several design solutions. The design consists in a modified Wilkinson power divider with added TLs to connect the isolation resistance to the output ports, in association with an open stub at the input port junction. While keeping very good isolation between output ports and matching on all ports, the proposed new power divider enables an optimal choice of the characteristic impedance of the TLs, of the output ports position with the best compromise between size and electrical performances.

This chapter focuses first on the design and the fabrication of the proposed power dividers at RF frequencies, carried out in a classical PCB technology, as proof-of-concept. 1:4 antennas feeding circuit was fabricated and measured, one at 2.45 GHz and another one at 5.8 GHz. The second one is associated to integrated slot-array antennas on a single substrate, taking advantages of small size, low profile, and low cost.

Based on the same technology demonstrated at RF frequencies, a 60 GHz power divider was designed in the 55 nm BiCMOS technology (by STMicroelectronics). S-CPWs were used in order to reduce the TLs' length and hence improve both compactness and performance.

III.1 Issues for Wilkinson power dividers in silicon technology

III.1.1 Isolation resistance

The undesired coupling between the two quarter-wave arms, or the distributed effects introduced by the physical requirements when stretching the resistance between the two arms can be devastating for the performances of the circuit at millimetre-wave frequencies. In order to connect the isolation resistance to the outputs using the smallest footprint as possible, the typical solution involves the wrapping of the quarter-wave arms into rounded shapes converging briefly to the resistance placement [77]-[78]. Another way is the use of interconnects between the isolation resistance and the signal strips [79], but their physical length is long as compared to the resistance dimensions so that they cannot be neglected. It is also worth mentioning that in practice it is really difficult to perfectly model the effects of these interconnects because of the vias, bends and contact resistance parasitics.

III.1.2 Characteristic impedance flexibility

The $70.7\ \Omega$ characteristic impedance of the quarter-wave arms fixed in the conventional Wilkinson power divider may be not reachable in all CMOS BEOL. We have seen for instance that in the 65 nm technology a maximum of $65\ \Omega$ can be obtained with microstrip TLs. If such a $65\ \Omega$ TL is used to build a power divider, the electrical lengths have to be adjusted to compensate for the characteristic impedance mismatch, so the design is more complex, and the return loss will be unavoidably degraded. In the case of S-CPWs, $70.7\ \Omega$ is easily reachable, but the corresponding S-CPW exhibits a lower quality factor as compared to the one with a characteristic impedance around $45\ \Omega$. Hence, flexibility for the choice of the characteristic impedance could permit to choose the TLs exhibiting the highest quality factor. Moreover, if different characteristic impedances leading to full matched, isolated and low loss power divider could be found with electrical lengths shorter than those of the conventional 90° , solutions would conclude to a more compact device.

III.1.3 State-of-the-art of the solutions

In [80], the authors added extra TLs for connecting the isolation resistance to the output ports as shown in Figure III.1. This avoids parasitic coupling between the two output ports and in the same time allows the isolation resistance access to be taken into account. Nevertheless, the proposed power divider suffers from higher surface as compared to the classical Wilkinson one because of the link between the two electrical lengths, e.g. $\theta_1 = \theta_2 + 90^\circ$. More recently, a general model was developed in order to give design rules for the synthesis of these additional TLs [81]. The characteristic impedances depend on the power ratio between the two output ports.

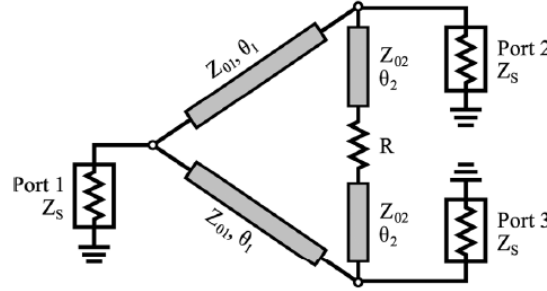


Figure III.1: Modified power divider with resistance access proposed in [80].

In [82], the conventional quarter-wave length of the impedance transformer arms were miniaturized thanks to open stubs and step impedances as shown in Figure III.2. This also enhanced flexibility in the choice of the TLs characteristic impedance, even though all the solutions cannot be applied in a CMOS technology. In counterpart, this topology leads to a complex transformation instead of the classical real one. Since the phase delays of the modified TLs are arbitrarily greater than -90° the isolation circuit does not only consist in a resistance but also a series capacitance for compensating the imaginary part. Moreover, these topologies do not bring any solution concerning the feeding lines.

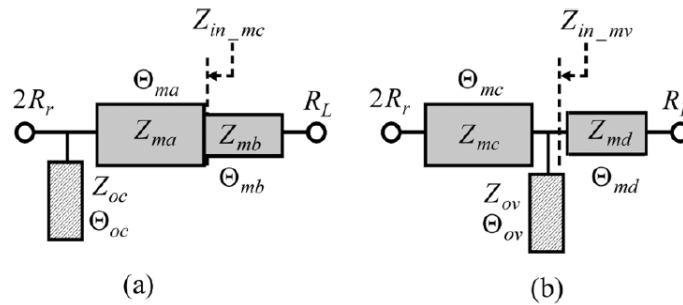


Figure III.2: Modified asymmetric impedance transformer proposed in [82].

III.2 Study of a new solution

III.2.1 Topology presentation

Figure III.3 gives the proposed power divider topology. Compared to the one presented in [80], an open stub of characteristic impedance Z_2 and electrical length θ_2 was added at the junction between input port 1 and the arms joining output ports 2 and 3. The characteristic impedance and electrical length of the latter were named Z_1 and θ_1 , while Z_3 and θ_3 characterize the arms connecting the output ports to the resistance. The new solution is thus a combination of [80], Figure III.1 and [82], Figure III.2. As will be seen, this combination offers a very high flexibility.

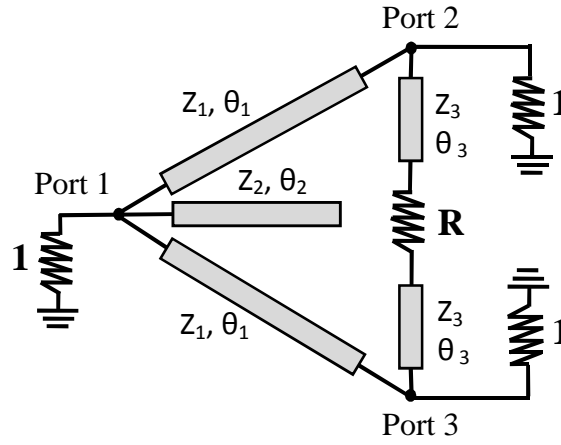


Figure III.3: Modified PD with open stub and resistance feeding lines.

III.2.2 Theory and design equations

It is easy to show, by an even-odd modes analysis, that adding the open stub (Z_2, θ_2) alone, without TLs (Z_3, θ_3), deteriorates the matching of the conventional Wilkinson topology. However, when both TLs (Z_3, θ_3) and open stub (Z_2, θ_2) are used, good matching and isolation can be achieved. They are slightly degraded as compared to the classical Wilkinson topology, but the corollary will be an extended bandwidth as demonstrated by Fano in [83]. For simplicity, all the characteristic impedances were normalized to the system characteristic impedance Z_0 , e.g. $z_i = Z_i/Z_0$. An even-odd mode analysis was carried out considering the circuit symmetry, as illustrated in Figure III.4. The open stub was replaced by two parallel open stubs with a characteristic impedance of $2Z_2$. Similarly, port 1 impedance was doubled. The line of symmetry crosses the middle of the resistance r so that it should be replaced by two series resistances with a value $r/2$. For given ports conditions and a given r , the two circuits, corresponding to even- or odd-mode analyses, totalize six unknown parameters corresponding to the three TLs (z_i, θ_i), so that six independent equations are required to find the solutions.

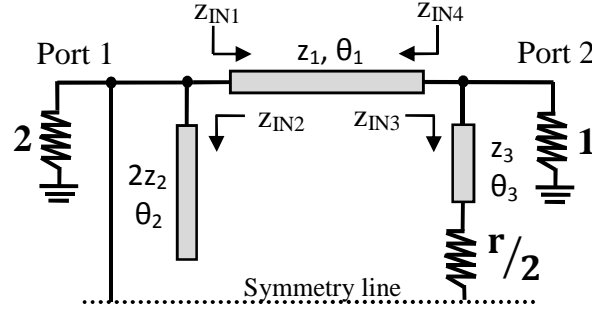


Figure III.4: Half of the normalized topology shorted within the odd-mode and open within the even-mode.

III.2.2.1 Even-mode analysis

For even mode excitation, the voltages at ports 2 and 3 have similar magnitude and phase. No current flows through the resistance $r/2$ which is open circuited. The value of the impedances z_{IN2_e} and z_{IN3_e} looking towards the open stubs (z_2, θ_2) and (z_3, θ_3) , in Figure III.4, are:

$$z_{IN2_e} = -j2z_2 \cot(\theta_2) \quad (\text{III-1})$$

$$z_{IN3_e} = -jz_3 \cot(\theta_3) \quad (\text{III-2})$$

Impedance z_{IN2_e} is in parallel with port 1. The equivalent impedance z_{eq1_e} of their combination is given by equation (III-3):

$$z_{eq1_e} = \frac{2z_2}{z_2 + j \tan(\theta_2)} \quad (\text{III-3})$$

The impedance z_{IN4_e} is then derived as follows:

$$z_{IN4_e} = z_1 \frac{z_{eq1_e} + jz_1 \tan(\theta_1)}{z_1 + jz_{eq1_e} \tan(\theta_1)} \quad (\text{III-4})$$

Impedance z_{IN4_e} is in parallel with z_{IN3_e} and should be equal to port 2 impedance in order to get a matching condition at port 2, leading to equation (III-5):

$$\frac{1}{z_{IN3_e}} + \frac{1}{z_{IN4_e}} = j \frac{\tan(\theta_3)}{z_3} + \frac{z_1 + jz_{eq1_e} \tan(\theta_1)}{z_1 z_{eq1_e} + jz_1^2 \tan(\theta_1)} = 1 \quad (\text{III-5})$$

From (III-5), the real and imaginary parts of the two members of the equation were split in two equations. Equation (III-6) was obtained by equating the real parts while equation (III-7) corresponds to equating the imaginary parts.

$$\begin{aligned}
& z_1 z_2^3 z_3 - 3z_1^2 z_2^2 z_3 \tan(\theta_1) \tan(\theta_2) \\
& + z_1^2 z_3 \tan(\theta_1) \tan(\theta_2)^3 = -z_1 z_2 z_3 \tan(\theta_2)^2 \\
& - 4z_2^2 z_3 \tan(\theta_1) \tan(\theta_2) \\
& - 4z_1 z_2^2 \tan(\theta_2) \tan(\theta_3) \\
& - z_1^2 z_2^3 \tan(\theta_1) \tan(\theta_3) \\
& + 3z_1^2 z_2 \tan(\theta_1) \tan(\theta_2)^2 \tan(\theta_3)
\end{aligned} \tag{III-6}$$

$$\begin{aligned}
& z_1 z_2^2 z_3 \tan(\theta_2) + z_1^2 z_2^3 z_3 \tan(\theta_1) \\
& - 3z_1^2 z_2 z_3 \tan(\theta_1) \tan(\theta_2)^2 = z_1 z_3 \tan(\theta_2)^3 \\
& + 2z_2^3 z_3 \tan(\theta_1) - 2z_2 z_3 \tan(\theta_1) \tan(\theta_2)^2 \\
& + 2z_1 z_2^3 \tan(\theta_3) - 2z_1 z_2 \tan(\theta_2)^2 \tan(\theta_3) \\
& - 3z_1^2 z_2^2 \tan(\theta_1) \tan(\theta_2) \tan(\theta_3) \\
& + z_1^2 \tan(\theta_1) \tan(\theta_2)^3 \tan(\theta_3)
\end{aligned} \tag{III-7}$$

In the same manner, impedance z_{IN3_e} looking towards the TL (z_3, θ_3) is in parallel with port 2 impedance, thus the equivalent impedance named z_{eq2_e} becomes:

$$z_{eq2_e} = \left(1 + \frac{1}{z_{IN3_e}}\right)^{-1} = \frac{-jz_3 \cot(\theta_3)}{1 - jz_3 \cot(\theta_3)} \tag{III-8}$$

Impedance z_{IN1_e} is the input impedance of TL (z_1, θ_1) loaded by z_{eq2_e} , given by (III-9):

$$z_{IN1_e} = z_1 \frac{z_{eq2_e} + jz_1 \tan(\theta_1)}{z_1 + jz_{eq2_e} \tan(\theta_1)} \tag{III-9}$$

The combination of z_{IN1_e} in parallel with z_{IN2_e} should be equal to port 1 impedance in order to obtain a matching condition at port 1, leading to equation (III-10):

$$\frac{1}{z_{IN1_e}} + \frac{1}{z_{IN2_e}} = \frac{z_1 + jz_{eq2_e} \tan(\theta_1)}{z_1 z_{eq2_e} + jz_1^2 \tan(\theta_1)} + j \frac{\tan(\theta_2)}{2z_2} = \frac{1}{z} \tag{III-10}$$

By developing and equating the real and imaginary parts of the two members of equation (III-10), equations (III-11) and (III-12) were derived:

$$\begin{aligned}
& z_1 z_3 \tan(\theta_2) \cot(\theta_3) - z_1^2 \tan(\theta_1) \tan(\theta_2) + 2z_1 z_2 \\
& + 2z_2 z_3 \tan(\theta_1) \cot(\theta_3) \\
& = z_1^2 z_2 z_3 \tan(\theta_1) \cot(\theta_3)
\end{aligned} \tag{III-11}$$

$$z_1 z_3 \tan(\theta_1) \tan(\theta_2) \cot(\theta_3) - z_2 z_3 \cot(\theta_3) = z_1 z_2 \tan(\theta_1) \tag{III-12}$$

Finally, the even-mode analysis leads to four different equations, (III-6), (III-7), (III-11) and (III-12).

III.2.2.2 Odd-mode analysis

For the odd-mode analysis, the voltages at ports 2 and 3 have the same magnitude and are 180° out-of-phase. The voltage is consequently equal to zero along the line of symmetry of the circuit which can be thus short circuited in its middle part. The impedance looking towards the circuits from port 2 can be calculated by means of the impedances z_{IN3_o} and z_{IN4_o} :

$$z_{IN3_o} = z_3 \frac{r/2 + jz_3 \tan(\theta_3)}{z_3 + jr/2 \tan(\theta_3)} \quad (\text{III-13})$$

$$z_{IN4_o} = jz_1 \tan(\theta_1) \quad (\text{III-14})$$

The combination of these two impedances in parallel should match port 2 impedance, which leads to the following equation (III-15):

$$\frac{1}{z_{IN3_o}} + \frac{1}{z_{IN4_o}} = \frac{z_3 + j\frac{r}{2}\tan(\theta_3)}{z_3 \frac{r}{2} + jz_3^2 \tan(\theta_3)} - j\frac{\cot(\theta_1)}{z_1} = 1 \quad (\text{III-15})$$

Equations (III-16) and (III-17) are obtained by equating the real and imaginary parts of equation (III-15), respectively:

$$z_3 \cot(\theta_1) \tan(\theta_3) = z_1 \left(\frac{r}{2} - 1 \right) \quad (\text{III-16})$$

$$-z_3 \cot(\theta_1) \cot(\theta_3) = z_1 \left(\frac{2}{r} z_3^2 - 1 \right) \quad (\text{III-17})$$

Equations (III-16) and (III-17) are the two missing equations over six independent equations, which is the necessary condition to solve a problem with six unknown parameters. Next, equation (III-16) is substituted into (III-17) in order to get:

$$\theta_3 = \tan^{-1} \left(\sqrt{\frac{-\frac{r}{2} + 1}{\frac{2z_3^2}{r} - 1}} \right) \quad (\text{III-18})$$

which implies the following condition on the value of the resistance r according to the value of the characteristic impedance z_3 :

$$\text{if } r < 2, \text{ then } z_3 > \sqrt{\frac{r}{2}} \text{ or if } r > 2, \text{ then } z_3 < \sqrt{\frac{r}{2}} \quad (\text{III-19})$$

Moreover, equation (III-16) can be rewritten as follows:

$$\theta_1 = \tan^{-1} \left(\frac{z_3 \tan(\theta_3)}{z_1 \left(\frac{r}{2} - 1 \right)} \right) \quad (\text{III-20})$$

From equation (III-20), it is obvious that the value of r cannot be lower than 2, which would lead to a negative value of the electrical length θ_1 or an electrical length longer than a quarter wave length which is not acceptable. Thus, the right condition among the two suggested in (III-19) is:

$$r > 2 \text{ with } z_3 < \sqrt{\frac{r}{2}} \quad (\text{III-21})$$

Meanwhile equation (III-12) can also be rewritten as follows:

$$\theta_2 = \tan^{-1} \left(\frac{z_2}{z_3 \cot(\theta_3)} + \frac{z_2}{z_1 \tan(\theta_1)} \right) \quad (\text{III-22})$$

Finally it is remarkable that equation (III-18) gives θ_3 versus r and z_3 only, equation (III-20) gives θ_1 versus r , z_1 , z_3 and θ_3 , and equation (III-22) gives θ_2 versus z_1 , z_2 , z_3 , θ_1 and θ_3 .

III.2.3 Design procedure

With an adequate procedure, it seems thus possible to find, in that order, the TLs' electrical length θ_3 , θ_1 and θ_2 which depend on the values of the characteristic impedances z_1 , z_2 , z_3 and resistance r . However, the three equations (III-6), (III-7) and (III-11) are too complex to be solved in an algebraic way with (III-18), (III-20), and (III-22). Consequently, for equations (III-6), (III-7), and (III-11) delta error functions, respectively named Δ_1 , Δ_2 , Δ_3 , were defined as:

$$\left| \frac{\text{member on the right} - \text{member on the left}}{\text{member on the right}} \right| \quad (\text{III-23})$$

A solution consists in a set of four values z_1 , z_2 , z_3 , and r . The electrical lengths θ_1 , θ_2 , and θ_3 uniquely depend on the solution set. A set is solution of the circuit if the three delta error functions are simultaneously equal to 0. A careful study showed that this condition cannot be reached, except for the particular solution $\theta_2 = \theta_3 = 0$, e.g. without open stub neither resistance feeding lines, leading to the conventional Wilkinson power divider. As an example, Figure III.5 shows the delta error functions versus Z_1 for two sets of values, set 1 (in black): $Z_2 = 25 \, \Omega$, $Z_3 = 25 \, \Omega$, $R = 105 \, \Omega$ and set 2 (in red): $Z_2 = 25 \, \Omega$, $Z_3 = 49 \, \Omega$ and $R = 105 \, \Omega$, respectively.

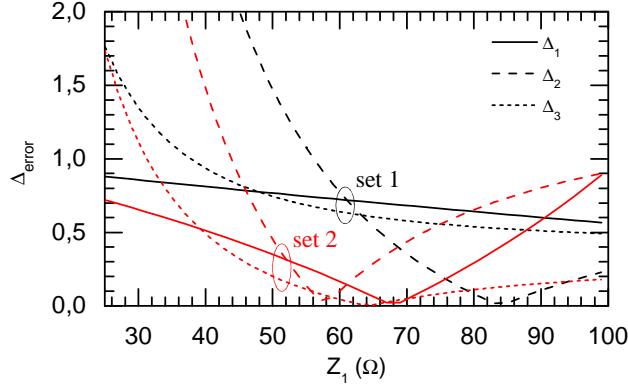


Figure III.5: Δ_{error} of (III-18), (III-20) and (III-22) for two sets of values.

For set 1, the delta error Δ_2 reaches 0 for $Z_1 = 84 \Omega$, whereas delta errors Δ_1 and Δ_3 are not equal to zero for the same characteristic impedance. In the same manner, considering set 2, Δ_1 , Δ_2 or Δ_3 are equal to 0 for three different values of Z_1 , e.g 67Ω , 57Ω and 65Ω , respectively. However, it is obvious that the average of the delta errors is smaller for Set 2 if Z_1 is chosen near 60Ω . Hence, even if a perfect set of characteristic impedances cannot be found, there exist some sets that enable to be close to the ideal solution. These “approximate solutions” can be obtained thanks to the use of a simple algorithm.

However a question remains which is how to rely the delta errors calculated from equations (III-6), (III-7) and (III-11) to the knowledge of power divider mismatch, isolation and insertion loss. A solution could be to link, in an algebraic way, the delta errors to some specific goals on the power divider S -parameters. Such relationship cannot be carried out easily. Another way could be to calculate directly the aforementioned S -parameters and to compare them to the power divider specifications, as a condition for the algorithm to end. A far simpler solution was used. As it is proved below, a single condition solely based on the scattering parameter S_{22} as close to zero as possible is sufficient to ensure a good matching at the three ports as well as a high isolation between the two output ports.

III.2.3.1 Demonstration of the good matching and isolation according to the value of S_{22}

Statement is valuable for any three ports network as long as (i) the symmetry condition between ports 2 and 3 is verified (balanced network) and (ii) there is no loss in the equivalent even-mode circuit (which means no resistive element in the even-mode circuit). Those conditions are fulfilled by the power divider given in Figure III.3. Due to condition (i) the latter can be redrawn as the four ports network in Figure III.16(a).

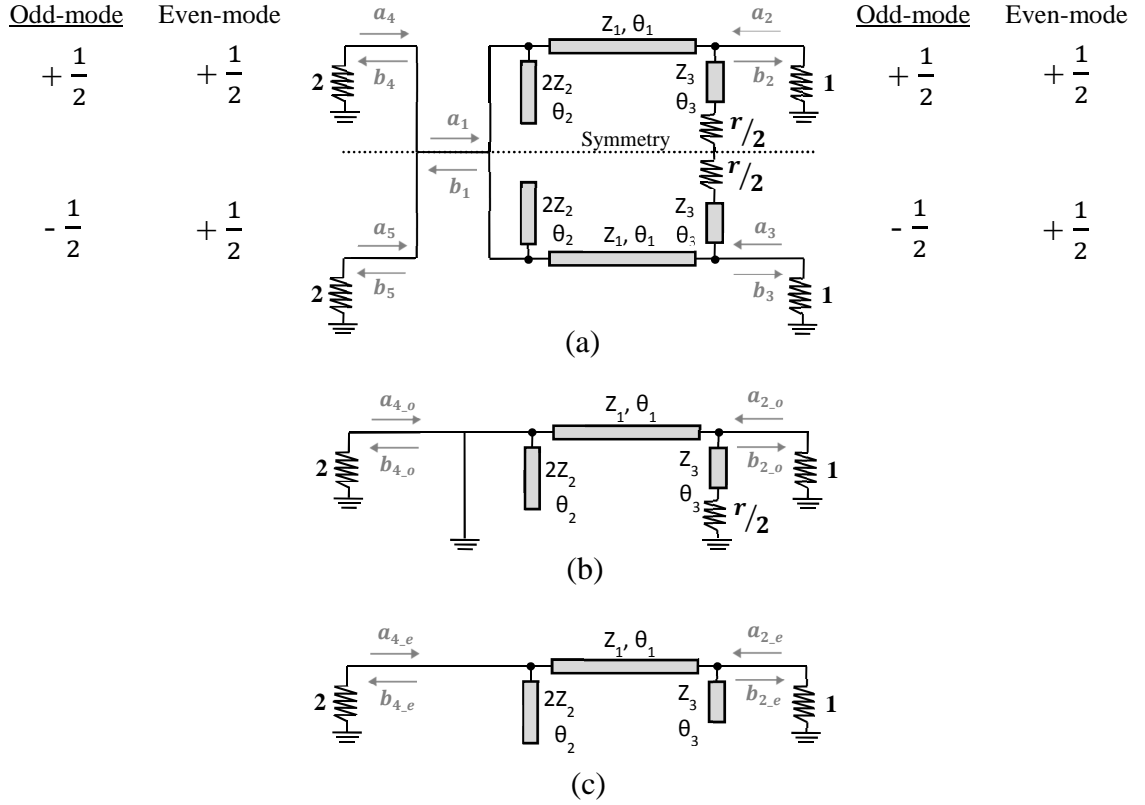


Figure III.6: a) Normalized representation as a four ports network of the power divider in Figure III.3, b) odd-mode schematic and c) even-mode schematic.

Based on those considerations, the network can be analysed by an even-/odd-mode approach. If an input power wave a_1 is considered at port 1, the following equations hold for the relationship between the power waves defined in Figure III.16, where “ e ” means even-mode “ o ” means odd-mode, respectively:

$$\begin{aligned}
 a_4 &= a_{4,e} + a_{4,o} & b_4 &= b_{4,e} + b_{4,o} \\
 a_5 &= a_{4,e} - a_{4,o} & b_5 &= b_{4,e} - b_{4,o} \\
 a_1 &= a_{1,e} + a_{1,o} & b_1 &= b_{1,e} + b_{1,o}
 \end{aligned} \tag{III-24}$$

Similarly, if an input power wave a_2 is considered at port 2, the following equations occur:

$$\begin{aligned}
 a_2 &= a_{2,e} + a_{2,o} & b_2 &= b_{2,e} + b_{2,o} \\
 a_3 &= a_{2,e} - a_{2,o} & b_3 &= b_{2,e} - b_{2,o}
 \end{aligned} \tag{III-25}$$

III.2.3.1.a Odd-mode analysis

As port 1 is shunted, see Figure III.6(b), it is obvious that no transmission may occur between ports 1 and 2. Consequently, the general form of the odd-mode scattering matrix $[S_o]$ is written as:

$$\begin{bmatrix} S_{11_o} & 0 \\ 0 & S_{22_o} \end{bmatrix} \quad (\text{III-26})$$

With no resistive element in the network, $|S_{11_o}| = |S_{22_o}|$ [12]. With the presence of a resistance in the network, as in the conventional Wilkinson power divider or in Figure III.6, necessarily $|S_{11_o}| \neq |S_{22_o}|$. Moreover, because of the shunt, power waves a_{1_o} and b_{1_o} are equal in the odd-mode to zero:

$$a_{1_o} = 0 \quad b_{1_o} = 0 \quad (\text{III-27})$$

III.2.3.1.b *Even-mode analysis*

The even-mode scattering matrix $[S_e]$ takes the form below:

$$\begin{bmatrix} S_{11_e} & S_{12_e} \\ S_{12_e} & S_{22_e} \end{bmatrix} \quad (\text{III-28})$$

The even-mode network being lossless, the two following equations hold:

$$\begin{aligned} |S_{22_e}| &= |S_{11_e}| \\ \text{and } S_{11_e}^2 + S_{12_e}^2 &= 1 \end{aligned} \quad (\text{III-29})$$

Moreover, power waves a_{1_e} and b_{1_e} may be expressed as:

$$a_{1_e} = \sqrt{2} \cdot a_{4_e} \quad b_{1_e} = \sqrt{2} \cdot b_{4_e} \quad (\text{III-30})$$

III.2.3.1.c *Discussion on the scattering parameters*

Using the equations (III-24) to (III-30) linking even, odd and global power waves, the demonstration given in Appendix-A leads to:

$$S_{11} = S_{11_e} \quad (\text{III-31})$$

$$S_{12} = \frac{S_{12_e}}{\sqrt{2}} = S_{13} = S_{21} = S_{31} \quad (\text{III-32})$$

$$S_{22} = S_{22_e} - S_{22_o} = S_{33} \quad (\text{III-33})$$

$$S_{23} = S_{22_e} + S_{22_o} = S_{32} \quad (\text{III-34})$$

In order to design a three ports device, a parametric study is often necessary. The convergence of the design process can be ensured by means of conditions on the scattering parameters. Various possibilities can be enforced.

1) Condition $|S_{11}| = 0$

This condition leads to $|S_{11_e}| = 0$ (III-31), implying $|S_{12_e}| = 1$ (III-29), and hence $S_{12} = 1/\sqrt{2}$ (III-32). This is sufficient as long as output ports matching is not required. However, such condition is not enough for the use of a power divider as a combiner where isolation is required.

2) Condition $|S_{22}| = 0$

Two solutions exist. The first one consists in equating S_{22_e} to S_{22_o} keeping them different from 0 (III-33), however this solution is not satisfactory for our power divider. Indeed, according to (III-34) if $S_{22_e} = S_{22_o} \neq 0$, S_{32} is not equal to 0 which means a bad isolation. The second solution is equivalent to having at the same time matching for both even- and odd-modes at port 2:

$$S_{22_o} = S_{22_e} = 0 \quad (\text{III-35})$$

Consequently:

- Matching at port 1 is realized:

Considering (III-29), $S_{22_e} = 0$ implies:

$$S_{11_e} = 0 \quad (\text{III-36})$$

Considering (III-31), $S_{11_e} = 0$ implies:

$$S_{11} = 0 \quad (\text{III-37})$$

- -3 dB ratio between ports 1 and 2 is reached:

Considering (III-29), $S_{11_e} = 0$ implies:

$$S_{12_e} = 1 \quad (\text{III-38})$$

Considering (III-32), $S_{12_e} = 1$ implies:

$$S_{12} = 1/\sqrt{2} \quad (\text{III-39})$$

- Perfect isolation is realized:

Considering (III-33), $S_{22_o} = S_{22_e} = 0$ implies:

$$S_{23} = 0 \quad (\text{III-40})$$

Hence, a matching condition on the scattering parameter S_{22} alone holds for the four conditions on S_{22} , S_{11} , S_{12} and S_{23} as long as the power divider stands symmetrical and lossless (except for the isolation resistance R).

III.2.3.2 Procedure for finding solutions

In practice, the algorithm described in Figure III.7 was used to find close solutions, based on the port 2 matching condition alone. Matlab software was used.

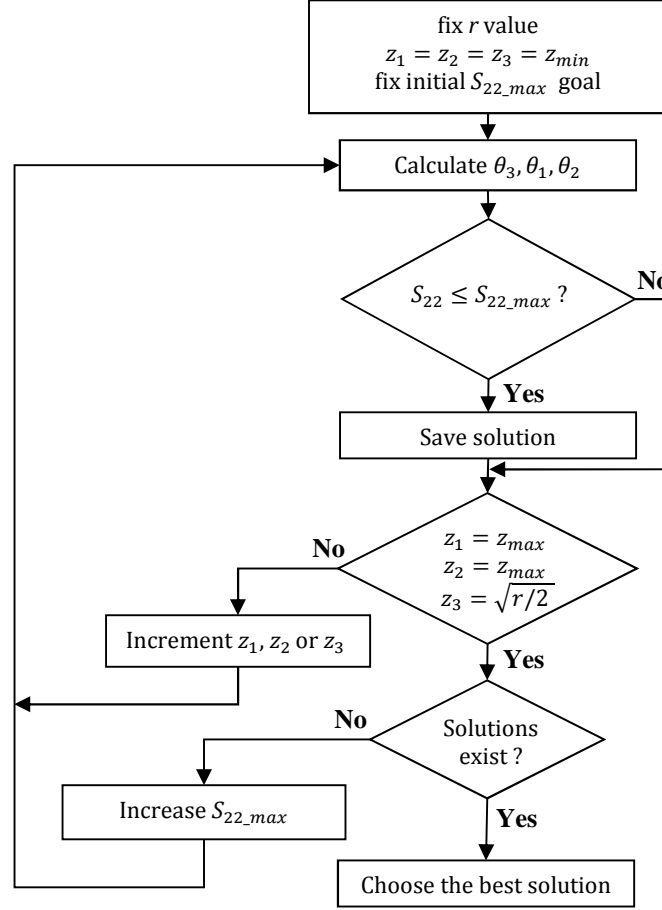


Figure III.7: Algorithm for finding solutions.

First, r must be fixed to the desired value and z_1 , z_2 and z_3 to the minimum achievable characteristic impedance given by the technology. Included in the three overlapping loops of z_1 , z_2 , and z_3 (symbolized with only one block in the algorithm), the three electrical lengths θ_3 , θ_1 , and θ_2 are calculated in this order, according to equations (III-18), (III-20) and (III-22). Then S_{22} is compared to the initial goal. Typically, it is a good choice to start the procedure with $S_{22_max} = -35$ dB. If after any combinations of z_1 , z_2 , and z_3 , S_{22} stays higher than S_{22_max} , this means that the goal is too ambitious. Consequently, S_{22_max} should be slightly increased. The poorer the conditions concerning S_{22_max} , the worst the isolation and matching of the power divider. In practice, the choice of S_{22_max} is deserved to the designer, depending on the specifications related to the application.

Finally, additional conditions concerning θ_i and/or z_i ranges, may lead to conditions on the device maximum size and/or quality factor for the TLs (in particular if integrated technologies are targeted). The designer thus can choose a compromise between the power divider electrical performance and size by electing the appropriate values of the characteristic impedances and electrical lengths.

III.3 Circuits design and experimental results

Two power dividers with two different values of R were fabricated as a proof-of-concept to illustrate and validate the method previously described. As shown in (III-21), r should be strictly bigger than the normalized value 2, e.g. $R > 100 \Omega$ when considering a $50\text{-}\Omega$ system characteristic impedance. One power divider has a value $R = 105 \Omega$ and another one $R = 150 \Omega$.

III.3.1 Power Divider with $R = 105 \Omega$

The targeted condition for S_{22} was fixed to -35 dB . The characteristic impedances' range of variation was fixed to $[25\text{-}100] \Omega$, except for Z_3 which is limited to 51Ω from (III-21). A step of 2Ω is a good compromise between time simulation and impedance resolution for the construction of the design graphs.

Figure III.8 shows the solutions in terms of electrical lengths θ_1 , θ_2 , and θ_3 , according to the characteristic impedances Z_1 , Z_2 , and Z_3 , respectively. Figure III.8(a) shows the electrical length θ_3 map versus Z_3 . θ_3 varies between 14° and 38° . Figure III.8(b) gives the electrical length θ_1 according to Z_1 and Z_3 . The colour scale indicates that the smaller the characteristic impedance Z_3 , the smaller the electrical length θ_1 . Consequently, in this example, a strong miniaturization could be reached with the choice of $Z_3 = 25 \Omega$ and $\theta_3 = 14.4^\circ$. With such a solution, several values for Z_1 and θ_1 are available. It may be noticed that the bigger Z_1 , the smaller θ_1 . $Z_1 = 81 \Omega$ appears to be a good compromise to avoid too high characteristic impedances, which leads to $\theta_1 = 57.7^\circ$. Lastly, Figure III.8(c) gives the electrical length θ_2 versus Z_1 and Z_2 , for various achievable values of Z_3 . Many possibilities exist for the pair (Z_2, θ_2) . Based on $Z_3 = 25 \Omega$ and $Z_1 = 81 \Omega$, a wide range remains possible but when taking into account design constraints this choice gets reduced. In particular, θ_2 should be chosen short enough to avoid parasitic coupling between the TLs (Z_3, θ_3) and (Z_2, θ_2) . $Z_2 = 39 \Omega$, leading to $\theta_2 = 35.2^\circ$ is a good couple.

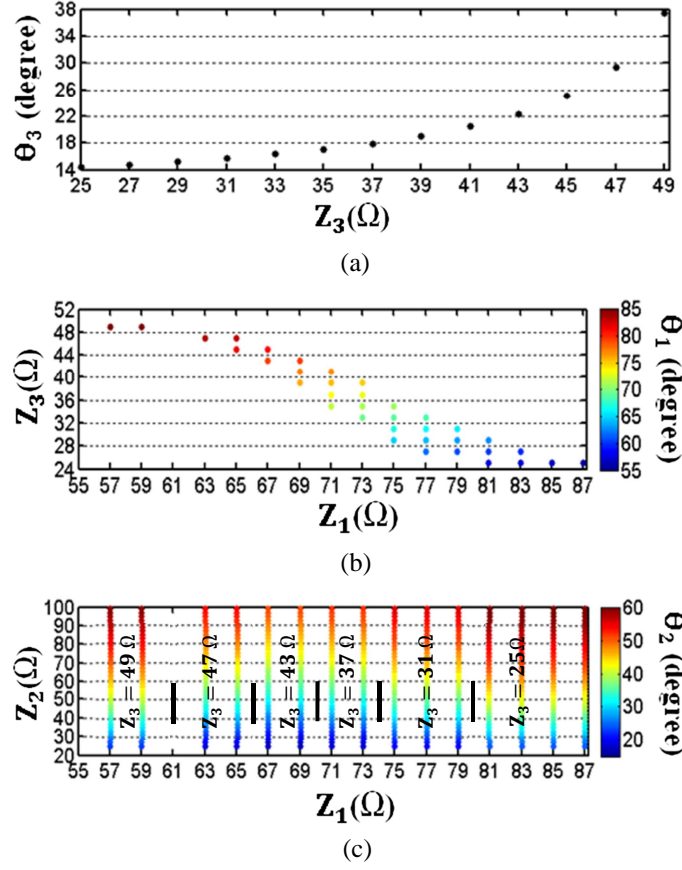


Figure III.8: Design graphs for $R = 105 \Omega$.

Calculi are based on theoretical equations only and do not consider junctions electrical models neither bends nor parasitic coupling that in practice contribute to degrade the performances. The electromagnetic simulation of the power divider with the chosen characteristic impedances and electrical lengths, including junctions, bends and coupling, showed that the working frequency was slightly shifted and the return loss a little bit degraded, consequently a tuning on these values was necessary. The final characteristic of the TLs after tuning are the following (original values are given between brackets): $Z_1 = 84 \Omega$ (81 Ω), $\theta_1 = 56^\circ$ (57.7°), $Z_2 = 39 \Omega$ (39 Ω), $\theta_2 = 30^\circ$ (35.2°), $Z_3 = 30 \Omega$ (25 Ω), $\theta_3 = 14.9^\circ$ (14.4°).

The circuits were fabricated on the dielectric substrate Rogers RO4003C, of relative permittivity 3.38 and thickness 813 μm . All circuits are working at the frequency of 2.45 GHz. A SOLT calibration was carried out on an 8720 Vector Network Analyzer. Figure III.9 compares the S -parameters obtained from electromagnetic simulations [Momentum by Agilent Technologies] and measurements, respectively. A very good agreement was obtained. While keeping the previous sets of (Z_i, θ_i) , the SMD resistance R placed in the fabricated circuit was measured equal to 100.2 Ω . As expected the power divider is very low loss with 0.13 dB of insertion loss only at 2.45 GHz, partially due to SMA RF connectors. The available bandwidth, defined by S_{11} below -20 dB, reaches 14 %, from 2.26 GHz to 2.6 GHz. Considering this bandwidth, the output port return loss S_{22} and

the isolation S_{32} are better than -24 dB, and reach -26 dB and -34 dB at 2.45 GHz, respectively. Remember that S_{22} was fixed to -35 dB as an input condition for the convergence of the design algorithm. Even if this value was reached in the optimization process in theory [Matlab], here again, since calculi do not take into account junctions models nor parasitic couplings, the return loss is degraded. Moreover, the value of R was 5 % below the right value. However, let's emphasize that -26 dB as a measured return loss constitutes excellent conditions for a large majority of applications.

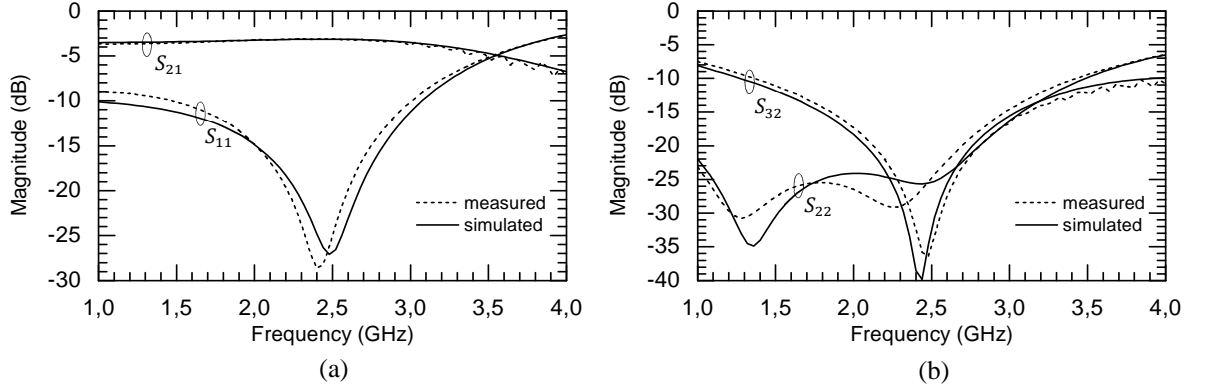


Figure III.9: Simulation [Agilent ADS Momentum™] and measurement results of the proposed topology with measured $R = 100.2 \Omega$ (theoretically 105Ω). $(Z_1, \theta_1) = (84 \Omega, 56^\circ)$, $(Z_2, \theta_2) = (39 \Omega, 30^\circ)$, $(Z_3, \theta_3) = (30 \Omega, 14.9^\circ)$. (a) Insertion loss and input return loss. (b) Isolation and output return loss.

Figure III.10 is a viewgraph of the fabricated power divider compared to the modified power divider early proposed in [80]. To design the latter, the value of R was fixed to 95Ω in order to get an electrical length of the TLs equal to 12.6° between the output ports and the resistance, which is close to the 14.9° of the topology presented here. The TLs' characteristic impedance was fixed to 69Ω , with an electrical length between ports 1 and 2 (or 3) equal to 102.6° ($90^\circ + 12.6^\circ$). These values lead to a surface of the proposed circuit that is 24 % smaller as compared to the one proposed in [80].

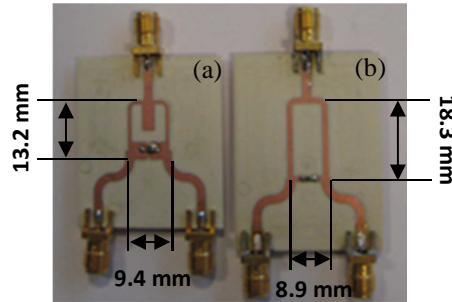


Figure III.10: Measured circuits. (a) Proposed design. (b) Power divider from [80].

To conclude, these results suggest that the proposed power divider is low loss, with really good matching and isolation. It is smaller and more flexible than the one proposed in [80] whilst keeping similar advantages such as the limitation of the parasitic coupling between the output ports thanks to the TLs connecting the resistance. In terms of simplicity,

miniaturization and performance, this design is also clearly well suited to further circuit integration considerations.

III.3.2 Power Divider with $R = 150 \Omega$

Another power divider was achieved and measured with R fixed to 150Ω . As for the previous one the maximum value of S_{22} was fixed to -35 dB for the initial design, the characteristic impedances still varied between 25Ω and 100Ω , and Z_3 was limited to 61Ω . Figure III.11 gives the graphs of the electrical lengths θ_1 , θ_2 , and θ_3 versus the characteristic impedances Z_1 , Z_2 , and Z_3 . The electrical length θ_3 varies between 44° and 69° with Z_3 , Figure III.11(a). Comparing the graphs in Figure III.8(a) and in Figure III.11(a) when R is fixed to 105 and 150Ω , respectively, we notice that when R increases the maximal reachable value of θ_3 increases and Z_3 needed to obtain this maximal value of θ_3 increases as well. With R equal to 500Ω , the maximal value of θ_3 is 77° for $Z_3 = 100 \Omega$. With higher resistance value, higher θ_3 can be obtained but Z_3 is beyond our characteristic impedances' range. The solution $\theta_3 = 49^\circ$, $Z_3 = 49 \Omega$, $\theta_1 = 60^\circ$ and $Z_1 = 65 \Omega$ enables high flexibility in terms of power divider shape with a relatively long TL connecting the output ports to the resistance. In counterpart, particular attention was paid on the electrical length θ_1 that should be longer than θ_3 to avoid meandering of the TL (Z_3, θ_3). The open circuit stub (Z_2, θ_2) was designed in a T shape in order to fit free space in the power divider loop. In order to get more flexibility and reduce the length of the stub, the TL, chosen as $Z_2 = 41 \Omega$ and $\theta_2 = 53^\circ$, was realized by a stepped-impedance structure, as shown in Figure III.12, with $Z_{2_1} = 125 \Omega$, $\theta_{2_1} = 3.5^\circ$, $Z_{2_2} = 35 \Omega$, and $\theta_{2_2} = 41^\circ$, respectively. Finally, the TL with the lower characteristic impedance was divided in two parallel TLs of similar electrical length but with a characteristic impedance multiplied by 2, so that Z_{2_2} becomes now equal to 70Ω . Here again a tuning was needed to adjust the performances of the power divider in order to take into account the junctions parasitics, bends and couplings. The final characteristics of the TLs after tuning are given herein with the original values between brackets: $Z_1 = 65 \Omega$ (65Ω), $\theta_1 = 58^\circ$ (60°), $Z_{2_1} = 130 \Omega$ (125Ω), $\theta_{2_1} = 5.8^\circ$ (3.5°), $Z_{2_2} = 88 \Omega$ (70Ω), and $\theta_{2_2} = 39^\circ$ (41°), $Z_3 = 51 \Omega$ (49Ω), $\theta_3 = 47^\circ$ (49°). Z_{2_1} can be considered as a high characteristic impedance, but such value is still achievable in a classical PCB technology and its shortness should not bring too much loss.

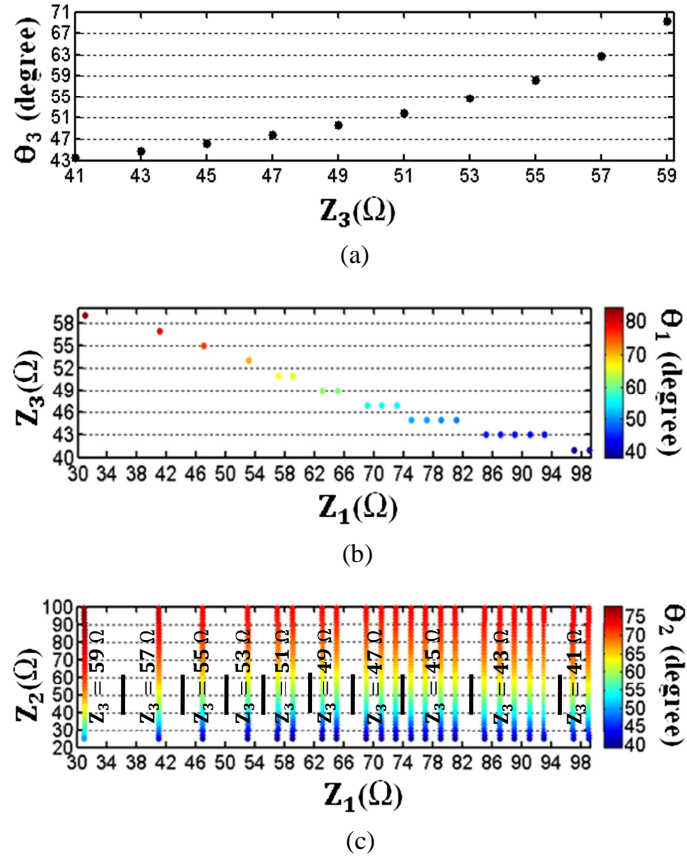


Figure III.11: Design graphs for $R = 150 \Omega$.

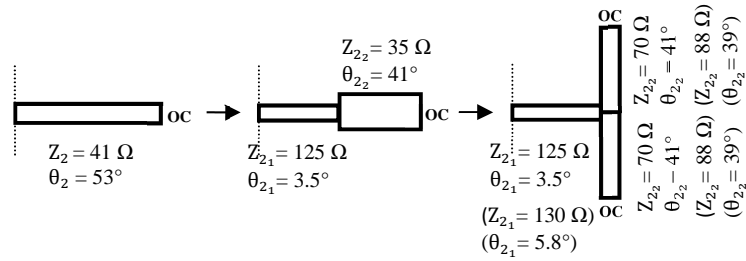


Figure III.12: Steps to design the open stub (Z_2, θ_2) in order to fit the free space in the power divider (before tuning and between brackets after tuning).

Figure III.13 gives a picture of this proposed power divider.

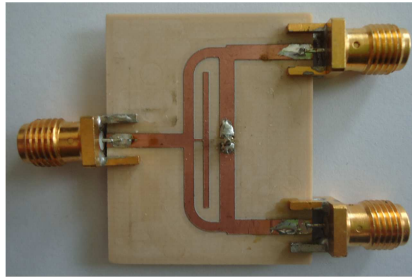


Figure III.13: Proposed design with $R = 150 \Omega$.

Figure III.14 compares the S -parameters obtained from electromagnetic simulations [Momentum] and measurements. The agreement between simulation and measurement results is very good. The insertion loss is 0.23 dB at 2.45 GHz and the bandwidth reaches 4.5 %, from 2.37 GHz to 2.48 GHz, see Figure III.14(a). The return loss at the output port S_{22} is better than -17 dB and the isolation S_{32} is better than -21 dB in the defined bandwidth. They reach -19 dB and -29 dB at 2.45 GHz, respectively, see Figure III.14(b). This power divider is only slightly smaller (6 %) than the one presented in [80] but its topology proves a huge shape flexibility which can, by the end, save much space in a global system. Here, the cost of such flexibility is a reduced bandwidth. The longer θ_3 , the narrower the bandwidth.

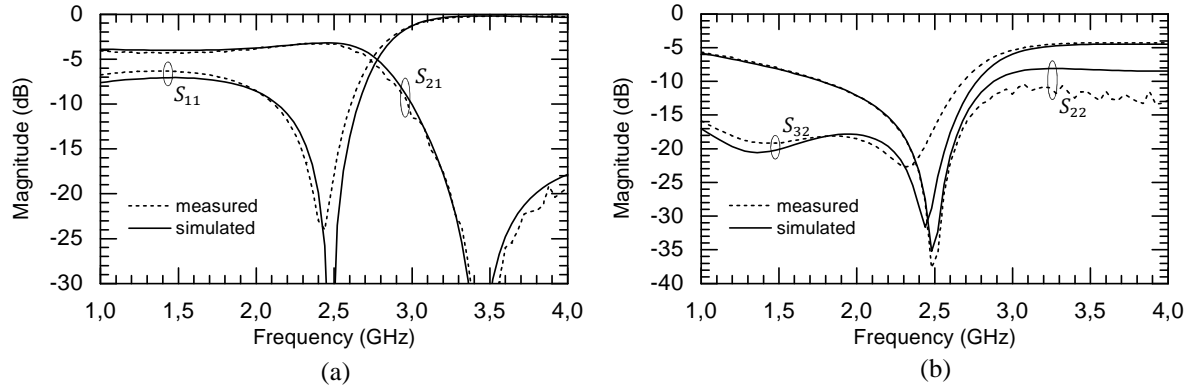


Figure III.14: Simulation [Momentum] and measurement results of the proposed topology with measured $R = 150 \Omega$. $(Z_1, \theta_1) = (65 \Omega, 58^\circ)$, $(Z_{21}, \theta_{21}) = (130 \Omega, 5.8^\circ)$, $(Z_{22}, \theta_{22}) = (88 \Omega, 39^\circ)$, $(Z_3, \theta_3) = (51 \Omega, 47^\circ)$.
 (a) Insertion loss and input return loss. (b) Isolation and output return loss.

An application of the fabricated power divider is illustrated in section III.5 where a 4-antenna feeding circuit was realized as a proof-of-concept. But before this, the influence and the potential in terms of harmonics suppression of the added TLs to our power divider are compared to the classical one.

III.4 Harmonics suppression

In [84] and [85] modified power dividers contain resistance feed lines and additional TLs or open stubs in order to suppress harmonics. These structures seem quite similar to ours, but they are exploited only for harmonics suppression and not for miniaturization or characteristic impedance flexibility. Their given procedures lead to power dividers with big area because of the several stubs of low characteristic impedances (equivalent to large widths) which make the meandering technique complex to apply. It is thus interesting to study the capability of our topology in spurious suppression.

In [84], the structure looks like the one presented in Figure III.3 but another open stub was added, named $(Z_D; \zeta)$, see Figure III.15. The electrical lengths δ (equivalent to θ_2 in our design), ψ (equivalent to θ_3), and ζ create three transmission zeros. The first step of

the design procedure in [84] consists in fixing their values according to the harmonics to suppress thanks to the formulas (III-41). In a second step, the other characteristic impedances and electrical lengths were chosen or calculated with extra formulas (given in [84]).

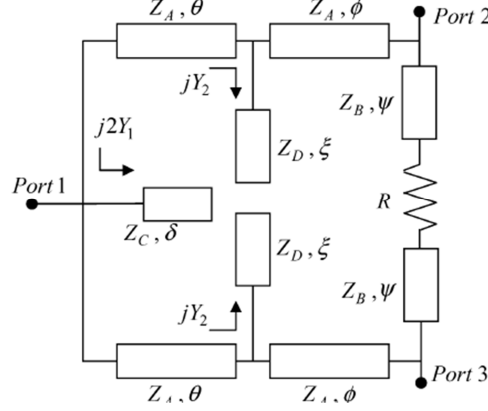


Figure III.15: Circuit configuration of the power divider proposed in [84] for spurious suppression.

$$\begin{aligned}
 f_1 &= \frac{\pi}{2\delta} \cdot f_0 \\
 f_2 &= \frac{\pi}{2\psi} \cdot f_0 \\
 f_3 &= \frac{\pi}{2\xi} \cdot f_0
 \end{aligned} \tag{III-41}$$

Figure III.16(a) shows the wideband ideal electric simulation of our power dividers with $R = 105 \, \Omega$, and Figure III.16(b) with $R = 150 \, \Omega$, respectively. Circuit simulations were performed with perfect TLs, perfect junctions and the TLs characteristics deduced from the optimization process. For the power divider with $R = 105 \, \Omega$ the transmission S_{21} shows two transmission zeros occurred at 6.26 GHz and 15.3 GHz, respectively. They correspond to the theoretical values calculated with (III-41), $f_1 = 6.26 \, \text{GHz}$ ($\delta = \theta_2 = 35.2^\circ$) and $f_2 = 15.3 \, \text{GHz}$ ($\psi = \theta_3 = 14.4^\circ$). For $R = 150 \, \Omega$ the two transmission zeros occurred at 4.16 GHz and 4.5 GHz which correspond to $f_1 = 4.16 \, \text{GHz}$ ($\delta = \theta_2 = 53^\circ$) and $f_2 = 4.5 \, \text{GHz}$ ($\psi = \theta_3 = 49^\circ$). So, as explained in [84] and demonstrated with our design, θ_2 and θ_3 create two predictable transmission zeros. This should be confirmed by electromagnetic simulations. Figure III.16(c) and (d) show the electromagnetic simulations [Momentum] of the two power dividers for $R = 105 \, \Omega$ and $R = 150 \, \Omega$, respectively. For the latters, junctions, bends and coupling were taken into account. In that case, with $R = 105 \, \Omega$ (see Figure III.16(c)), the resonances occurred at 6.8 GHz instead of $f_1 = 7.35 \, \text{GHz}$ ($\theta_2 = 30^\circ$ after tuning) and 15.8 GHz instead of $f_2 = 14.8 \, \text{GHz}$ ($\theta_3 = 14.9^\circ$ after tuning). For $R = 150 \, \Omega$ (see Figure III.16(d)), the resonances occurred at 3.4 GHz instead of $f_1 = 4.16 \, \text{GHz}$ (the open stub in T-shape after tuning is equivalent to $\theta_2 = 53^\circ$) and 4.9 GHz instead of $f_2 = 4.7 \, \text{GHz}$ ($\theta_3 = 47^\circ$ after tuning).

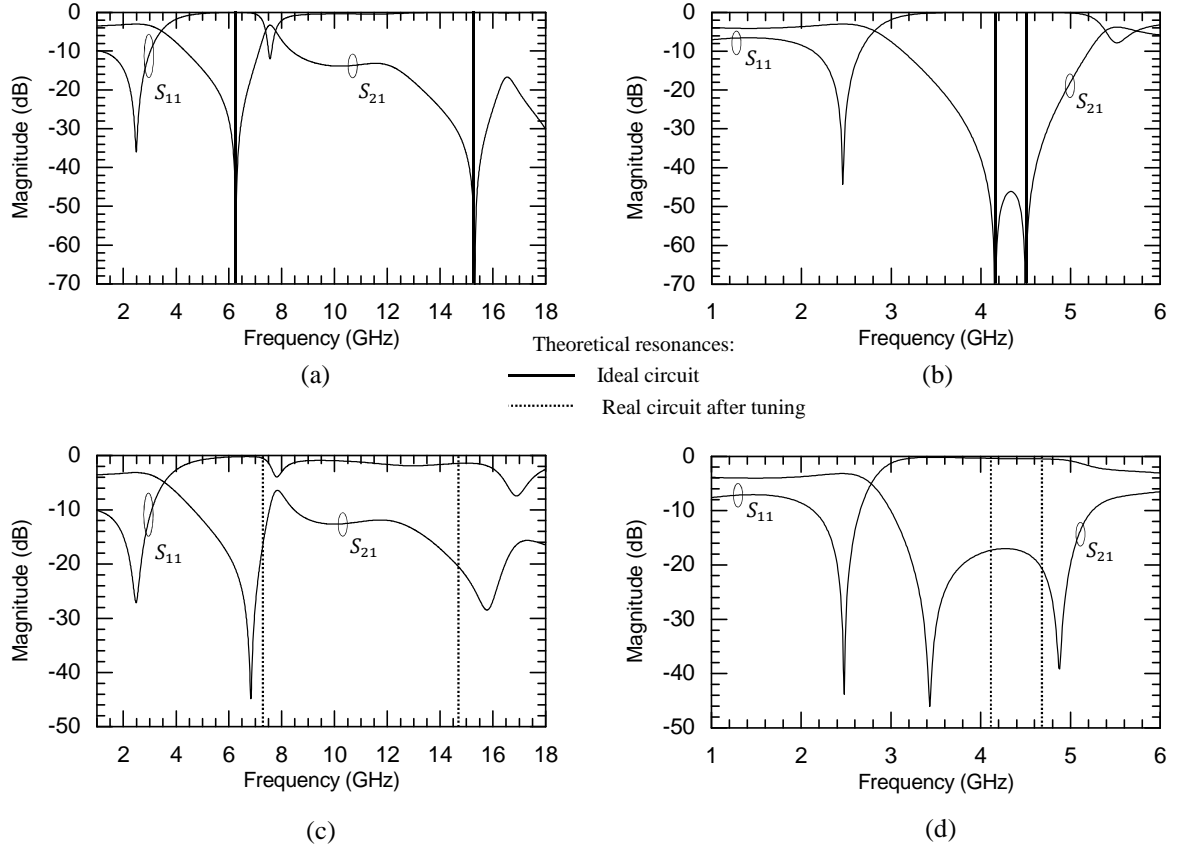


Figure III.16: Electric simulation of the power dividers with (a) $R=105\ \Omega$ and (b) $R=150\ \Omega$ and electromagnetic simulation on Momentum with (c) $R=105\ \Omega$ and (d) $R=150\ \Omega$.

The junctions, bends and unwanted coupling obliged us to tune the TLs parameters. The modifications of θ_2 and θ_3 had for consequence to change the resonance frequencies. Despite the values of the electrical lengths after tuning are used to calculate the theoretical resonances, a mismatch persists between the calculation and the electromagnetic simulation due to the parasites.

The electrical lengths θ_2 and θ_3 create transmission zeros that can be used for spurious suppression. In the case of strong miniaturization solution of the power divider as it has been achieved with $R = 105\ \Omega$, these electrical lengths are really small and induce resonances at much higher frequencies as compared to the working frequency harmonics. Hence the interest for harmonics suppression is low. However, when $R = 150\ \Omega$ is considered, it is possible to take profit of these resonances. The drawback of the proximity of the first resonance is a smaller bandwidth. With the purpose of harmonic suppression, first R must be fixed, then θ_2 and θ_3 can be calculated with (III-41). After that, the other parameters can be chosen thanks to the design graphs as presented before. An electromagnetic simulation is needed at the end to precisely tune the resonance frequencies.

III.5 Antennas array feeding network application

III.5.1 2.45 GHz working frequency

The power divider with $R = 150 \Omega$ was used as a 1:4 feeding network to be applied in a 4-antennas array. Two power dividers were connected in parallel at the outputs of a first one thanks to TLs, called (Z_4, θ_4) , in such a way that each output stays equidistant from its neighbours. Z_4 and θ_4 were fixed after a tuning procedure. The choice of a characteristic impedance Z_4 different from 50Ω offers the opportunity to slightly increase the bandwidth, as compared to the single power divider bandwidth. Z_4 and θ_4 were taken equal to 45Ω and 165° , respectively.

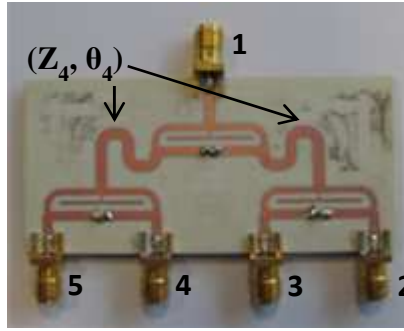


Figure III.17: 1:4 feeding circuit.

Figure III.17 shows the fabricated circuit and Figure III.18, the comparison between simulation and measurement results, respectively. The agreement is very good. The insertion loss is 0.48 dB above the ideal value of 6 dB at 2.45 GHz. The bandwidth, defined by S_{11} below -15 dB, reaches 15 %, from 2.26 GHz to 2.63 GHz, as shown in Figure III.18(a). In the considered bandwidth, the return loss at the output port S_{22} is better than -15 dB. The isolation S_{23} , which is the one between two outputs of the same power divider (i.e. between output ports 2 and 3, or 4 and 5, respectively) is better than -15 dB, while the isolation S_{24} which is the one between two outputs from different power dividers is better than -23 dB, as shown in Figure III.18(b). At 2.45 GHz, S_{11} , S_{22} , S_{23} and S_{24} are equal to -17 dB, -18 dB, -21 dB and -35 dB, respectively. It would be very easy to improve the network return loss thanks to the tuning of the TLs (Z_4, θ_4) . This would lead, in counterpart, to the reduction of the bandwidth.

Thanks to the particular shape of the proposed circuit, it is possible to save more surface area compared to what would be obtained with conventional Wilkinson type power dividers. It is easy to reach both flexibility in the topology and electrical performances. As in an antenna array the distance between the output ports is a major point to address, with our topology we can first fix this distance, then miniaturize the PD to match as far as possible the topology conditions whilst miniaturizing the device and finally play on (Z_4, θ_4) for the best compromise between bandwidth and input matching.

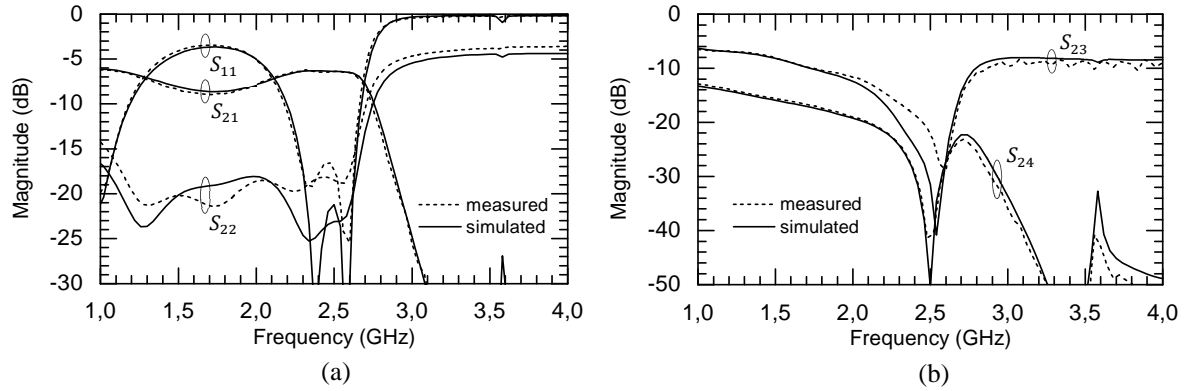


Figure III.18: Simulation and measurement results of the 1:4 feeding circuit at 2.45 GHz. (a) Magnitude of S_{21} , S_{11} and S_{22} . (b) Magnitude of S_{23} and S_{24} .

III.5.2 5.8 GHz working frequency

Another 1:4 feeding network with four-by-eight integrated slot-array antennas [86] was designed and fabricated at 5.8 GHz on the same dielectric substrate Rogers RO4003C, as shown Figure III.19. Before showing the measurement results of the full circuit, the feeding network alone is studied.

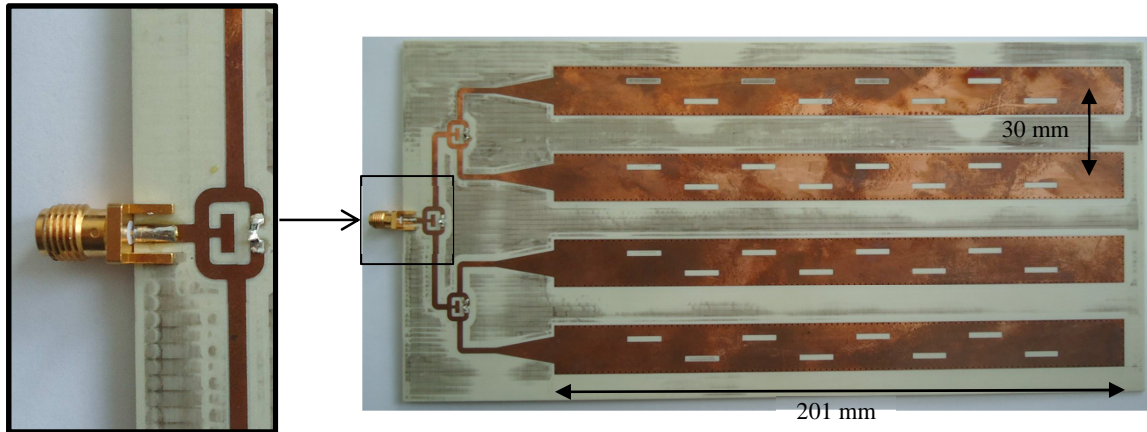


Figure III.19: Fabricated slot array antenna with its feeding network.

III.5.2.1 1:4 feeding network

The resistance R of the single power divider was fixed to 150 Ω . The design graphs in Figure III.11 were used once again. The solution with $\theta_3 = 52^\circ$, $Z_3 = 51 \Omega$, $\theta_1 = 66^\circ$, $Z_1 = 58 \Omega$, and the couple $\theta_2 = 53^\circ$, $Z_2 = 41 \Omega$, was chosen. Here again the open circuit stub (Z_2, θ_2) was designed in a T shape with stepped-impedance structure, as in Figure III.12. After tuning, the final TLs parameters became: $\theta_3 = 47^\circ$, $Z_3 = 58 \Omega$, $\theta_1 = 60^\circ$, $Z_1 = 56 \Omega$ and $Z_{2_1} = 75 \Omega$, $\theta_{2_1} = 14.7^\circ$, $Z_{2_2} = 59 \Omega$, and $\theta_{2_2} = 18.4^\circ$. Z_4 was taken equal to 50 Ω . Figure III.20 shows the comparison between electromagnetic simulation and measurement results of the 1:4 feeding circuit without the antennas. The insertion loss is 1 dB above the ideal value of 6 dB at 5.8 GHz. The bandwidth, defined by S_{11}

below -15 dB, is 9.3 %, between 5.46 and 6 GHz, as shown in Figure III.20(a), which is large enough for this application. In the considered bandwidth, the return loss at the output port S_{22} is better than -18 dB. The isolation S_{23} (between two outputs of the same power divider) is better than -15.8 dB, while the isolation S_{24} (between two outputs from different power dividers) is better than -20.5 dB, as shown in Figure III.20(b). At 5.8 GHz, S_{11} , S_{22} , S_{23} and S_{24} are equal to -17.2 dB, -20.1 dB, -23.9 dB and -25.8 dB, respectively.

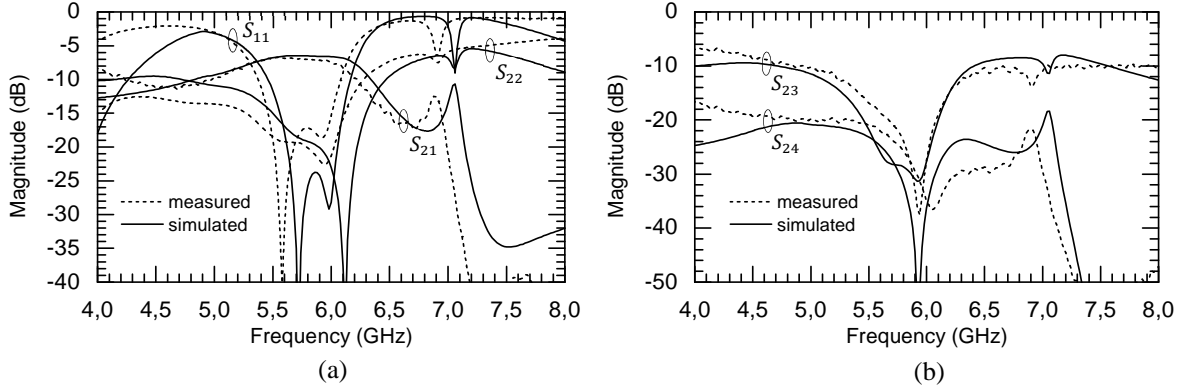


Figure III.20: Simulation and measurement results of the 1:4 feeding circuit at 5.8 GHz. (a) Magnitude of S_{21} , S_{11} and S_{22} . (b) Magnitude of S_{23} and S_{24} .

III.5.2.2 1:4 feeding circuit with antennas

In [86], a four-by-eight substrate integrated waveguide (SIW) slot array antenna was proposed at 10 GHz. Next, a two-by-eight was developed at 5.8 GHz in [87]. They are composed of longitudinal slots and via holes. The volume in the substrate integrated waveguide, delimited by the rows of the via holes (w) and the height of the substrate, acts as an equivalent rectangular waveguide. In our application a four-by-eight SIW slot array antenna at 5.8 GHz was fabricated and measured. 50 Ω microstrip feeding lines were used with tapered transitions to match impedances between the output ports of the power divider and SIW guides [88]. The dimensions of the antennas array given in Figure III.19 and in Figure III.21 were optimized with the 3D electromagnetic simulation software CST.

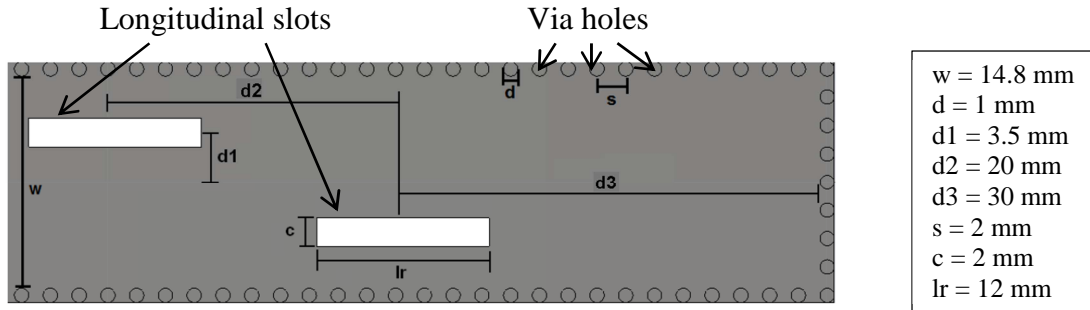


Figure III.21: Configuration of the on-substrate integrated slotted-waveguide synthesized using metallized via-hole arrays from [86].

The return loss of the SIW slot array antenna was measured from 4 to 7 GHz. The results are shown in Figure III.22. The return loss shows a 5.65 GHz working frequency instead of 5.8 GHz, which means a shift of 150 MHz. At 5.65 GHz it is -18 dB and less than -10 dB within a bandwidth of 43 MHz.

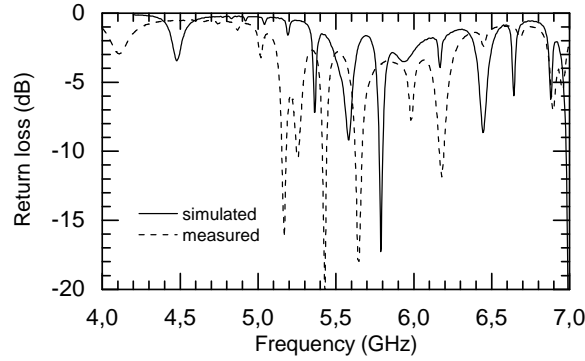


Figure III.22: Return loss of the 1:4 antennas array.

The measured E -plane pattern at 5.65 GHz is compared with the simulated pattern in Figure III.23(a), and the measured and simulated H -plane patterns in Figure III.23(b). At 0° the measured gain reaches 10.1 dB instead of 13.5 dB in simulation, and 10.3 dB instead of 13.5 dB for H -plane and E -plane, at 5.65 GHz, respectively.

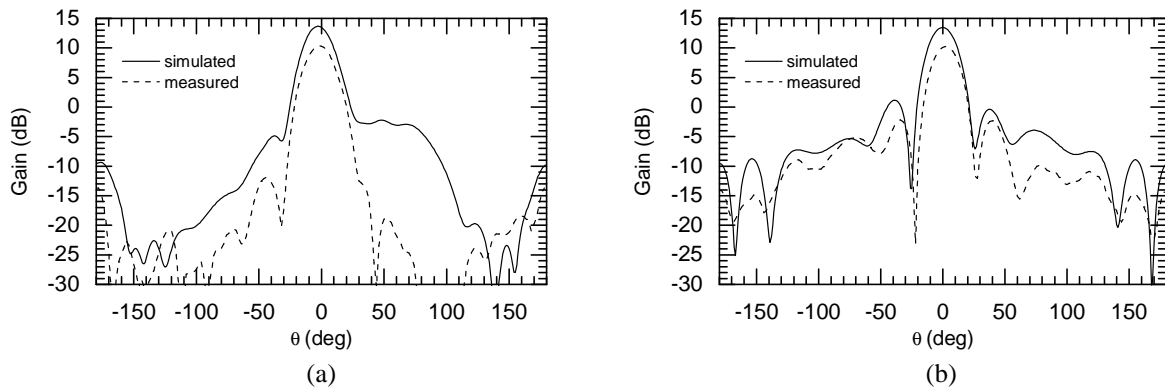


Figure III.23: Simulated and measured (a) E -plane and (b) H -plane radiation pattern at 5.65 GHz.

The measurement of the feeding circuit alone showed good results, with the expected working frequency and good matching, so the discrepancies of the full circuit are caused by the antennas array. They are certainly due to the inaccuracy of the fabrication process: indeed the via holes plating and slots dimensions are critical.

III.6 Millimetre-wave application

The study of the new power divider in PCB technology shows that such a circuit meets all the requirements needed for a silicon technology and is ready for integration. Thus it was designed in the 55 nm BiCMOS technology described in chapter II, for a

working frequency at 60 GHz. It is still under fabrication meanwhile the writing of this manuscript, so only the simulation results are presented herein.

III.6.1 Design and simulation

For the TL (Z_1, θ_1) between the input and output ports, S-CPW were used, whereas microstrip TLs were chosen for the open stub and the resistance feed lines because they are narrower. Here again the bends and junctions were realized with microstrips. The value of the resistance R was fixed to 105 Ω ; so the design graphs given in Figure III.8 were used to choose a solution. The resistance is a polysilicon type. Two ways for selecting a design were possible:

- Considering that the quality factor is quasi-constant for the microstrip TLs but that it depends on the characteristic impedance for the S-CPW, the optimal solution can be achieved by fixing first Z_1 with the characteristic impedance leading to the best quality factor of the S-CPW. Then, other parameters can be determined with the design graphs.
- The TLs' parameters can be simply fixed by the electrical lengths leading to the smallest component. In that case the characteristic impedances leading to the best quality factor S-CPW are not used. Moreover the characteristic impedance of microstrip lines is limited in integrated technologies.

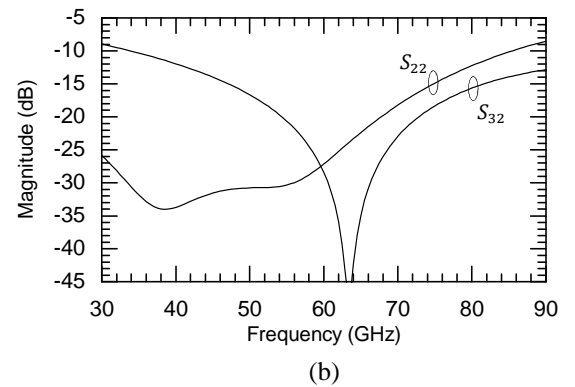
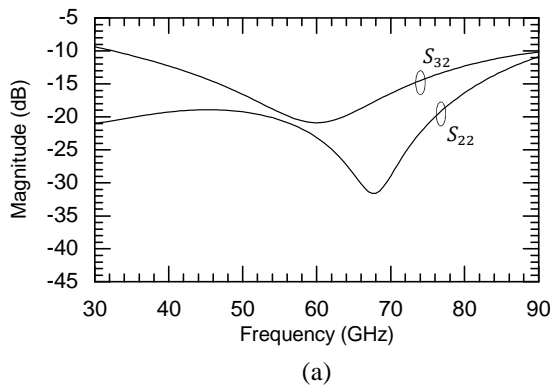
A study comparing these two methods showed that the second one leads to a smaller power divider area. Indeed, for lower Z_1 (better Q for S-CPWs), θ_1 and θ_3 increase (Figure III.8), and despite a higher Q , the total loss gets higher than with smaller θ_i with lower Q . Consequently, the second method was finally applied. This circuit was fabricated on the same chip than the branch-line coupler which will be presented in chapter IV. To avoid having too many different TLs to characterise, the same 26 Ω microstrip TL used in the branch-line coupler were used as the stub and the resistance feeding lines. Finally the selected solution was $Z_1 = 83 \Omega$, $\theta_1 = 59^\circ$, $Z_2 = 26 \Omega$, $\theta_2 = 24^\circ$, $Z_3 = 26 \Omega$ and $\theta_3 = 15^\circ$. Figure III.24(a) shows the schematic of the power divider and gives its dimensions. The 83 Ω characteristic impedance cannot be achieved with a microstrip TL in the 55 nm BEOL, so a value of 72 Ω was used. Because of this lower value, the length of the S-CPWs needed to be shortened by 5 μm (corresponding to 1°) to shift back the working frequency to 60 GHz while the microstrip stub was shortened by 13 μm (corresponding to 1.8°) in order to improve the input port matching. The simulation was carried out with equivalent TLs with the parameters given in chapter II, with perfect S-CPW/microstrip transitions, $R = 100 \Omega$, and without the 50 Ω feeding lines. The layout with the differential pads is given in Figure III.24(b) and the results are given in Figure III.25. At 60 GHz, the transmission coefficient S_{21} shows only 0.55 dB of added insertion loss above the 3 dB. The return loss at any port is lower than -28 dB. The isolation S_{32} is -26.6 dB. For an input port return loss S_{11} better than 20 dB, the bandwidth is 20 % (between 53 and 65 GHz), the

Ref./Tech.	Freq. (GHz)	Topology	Insertion loss (dB)	Return loss		Isolation (dB)	In 20 % bandwidth				Area (mm ²)
				S ₁₁ (dB)	S ₂₂ & S ₃₃ (dB)		Max. insertion loss (dB)	Return loss		Min. isolation (dB)	
								S ₁₁ (dB)	S ₂₂ & S ₃₃ (dB)		
[54]/90 nm CMOS	60	slow-wave elevated coplanar waveguide	-5.3	-8	-11	-12	-5.3	-6	-10	-11	0.051
[55]/90 nm CMOS	45	asymmetrical shunt- stub and meander-line	-3.9	-21	-15	-19	-4.2	<-13	-14	-15	0.06
[56]/0.13 μm BiCMOS	60	meander-line	-3.5	-19	-17	-22	-3.7	<-17	<-17	-18	0.12
[57]/0.18 μm SiGe BiCMOS	60	floating defected grounding structure and meander-line	-4.5	-	-16.5	-21	-4.3	-	-16.5	-19	0.09
This work	60	S-CPW, stub and resistor acces	-3.55	-28	-28	-26	-3.62	-25	-25	-19	0.104

Table III.1 : Comparison of the simulated power divider with the state-of-the-art.

III.6.2 Sensitivity to the resistance value

In CMOS technology, the polysilicon resistances as the one used here exhibit a variation of $\pm 20\%$ around the nominal value. It is thus important to verify the impact of such variation on the power divider performances. As the resistance determines only the isolation and the output ports matching, only S_{22} and S_{32} are modified with R . Figure III.26(a) and Figure III.26(b) shows S_{22} and S_{32} for the lowest and greatest possible values, 80 Ω and 120 Ω , respectively. Still in the bandwidth between 53 GHz and 65 GHz, determined with a return loss S_{11} better than 20 dB, the isolation is in the worst case better than 18 dB and S_{22} is better than 19.8 dB.

Figure III.26: Output port S_{22} and isolation S_{32} simulated at 60 GHz with (a) $R = 80\ \Omega$ and (b) $R = 120\ \Omega$.

The resistance variation degrades the isolation and the output ports matching but simulated results show still acceptable performances. The polysilicon resistance of 100 Ω has also been designed alone on the same chip in order to extract its exact value.

III.7 Conclusion

A new topology of power divider was studied. It leads to more flexibility and better compactness as compared to the classical Wilkinson power divider. Hence, it is well suited for a fabrication in silicon technology at millimetre-wave frequencies. Design rules were carried out thanks to design graphs, and a simple method of optimization.

Two power dividers were realized at 2.45 GHz in a PCB technology as proofs-of-concept, with different characteristics. They proved the high level of flexibility offered by the new developed topology. Measurement and simulation results were in very good agreement and proved the efficiency of the design method. The two 1:4 antenna arrays feeding network achieved thanks to the flexible power divider, can minimize the surface area of these feeding networks.

The simulation results and the surface area of the modified power divider designed at 60 GHz in the 55 nm BiCMOS technology confirmed that the new proposed topology is well suited for CMOS millimetre-wave power dividers. It ensures a low loss, full-matched and isolated component together with a small surface, thanks to the use of S-CPW with high quality factor. The measurement of this up-coming circuit should confirm the expectation.

If we keep in mind beam-steering application, efficient feeding circuits for antenna arrays can now be achieved and only reflection type phase shifters (RTPS) with high FoM have to be performed yet. In the next chapter two topologies of RTPS are provided, one in RF in PCB technology and another one at 60 GHz in CMOS.

Chapter IV : New topologies of Reflection Type Phase Shifter for high figure of merit

Phase shifters, used to adjust the phase of the wave, are widely used in radar phased array systems. They have to be compact, low loss, and low cost to enable consumer applications.

As explained in the first chapter, among the three main types of passive phase shifters which are the switched-network approach, the loaded transmission lines (TLs), and the reflection type (RTPS), only the last associates continuous and accurate phase shift with good matching. Also, it has been shown that reflection type phase shifters reaching 360° of phase shift and/or with really small insertion loss variation can be realized in printed circuit board technology (PCB). Concerning integrated technology, the literature barely provide RTPS with phase shift higher than 200° at 60 GHz, and seems totally void for phase shift of 360° . The referred devices exhibit high insertion loss leading to poor figures of merit (FoM). As already said in chapter I, the FoM is defined by the ratio of the maximal relative phase shift over the maximal insertion load.

$$FoM = \frac{\text{maximal relative phase shift (in } ^\circ \text{)}}{\text{maximal insertion loss (dB)}} \quad (IV-1)$$

In this chapter, three RTPSs with design method are proposed in PCB technology in order to reach high FoM. The reflection loads are easy to design, composed of one transmission line with varactors, and without extra lumped element. For proof of concept, one RTPS was realized to achieve a maximal phase shift of 200° with a maximal FoM, while the others were designed to reach 360° of phase shift, but with a lower FoM. Special attention is paid to the insertion loss in order to keep it as constant as possible whatever phase shift. The background principle is explained, the design procedure is given and circuits design and experimental results are described. A very good agreement between measurement and simulation results was achieved.

One RTPS in integrated technology was also designed at 60 GHz. Its reflection loads are based on a slow-wave coplanar waveguides (S-CPW) phase shifter with variable capacitors. The topology of this new phase shifter which is currently under study in our laboratory is explained. As the circuit is in-process, only the simulation results are presented. A phase shift of 341° is expected.

Finally, a new concept of reflection load for RTPS is suggested as a perspective, mixing digital and analog control to reach 360° of phase shift, high FoM and compactness.

IV.1 Study of the topologies

IV.1.1 Reflection load with one varactor

Figure IV.1 shows the schematic of the proposed RTPS, which consists of a 3-dB branch-line coupler loaded by two identical networks. The network is composed of a transmission line of characteristic impedance Z_1 and electrical length θ_1 , in series with a varactor of capacitance C and a resistance R representing the parasitic resistance of the varactor. Z_{IN} is the input impedance of each load. The branch-line coupler presents a port impedance Z_0 at ports 1 and 2 and a port impedance Z_T at the loaded ports. The relationships between the characteristic impedances of the transmission lines of the branch-line coupler and its ports impedances were given in the first chapter and are rewritten in Figure IV.1.

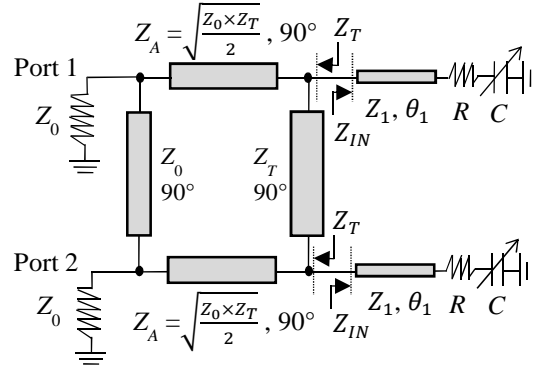


Figure IV.1: Proposed RTPS with only one varactor for each reflection load

Without considering the loss of the transmission lines nor R , Z_{IN} can be written as:

$$Z_{IN} = j \frac{-Z_1 + Z_1^2 C \omega \tan \theta_1}{Z_1 C \omega + \tan \theta_1} \quad (\text{IV-2})$$

Let's consider first an ideal capacitor, e.g. with an infinite capacitance range $[0; +\infty[$ and $R = 0 \Omega$, ideal transmission lines without losses, and Z_1 in the range $[0; +\infty[$. When the minimum value of the capacitor is faced, $C = 0$, the input impedance of the load, obtained from (IV-2), is:

$$Z_{IN \ C=0} = j \frac{-Z_1}{\tan \theta_1} \quad (\text{IV-3})$$

When the capacitor maximal value is looked at, $C = +\infty$, the input impedance of the load becomes:

$$Z_{IN \ C=+\infty} = j Z_1 \tan \theta_1 \quad (\text{IV-4})$$

It is easy to demonstrate from:

$$\Gamma = \frac{Z_{IN} - Z_T}{Z_{IN} + Z_T} \text{ and } S_{21} = j\bar{\Gamma} \quad (\text{IV-5})$$

already given in chapter I, that the relative phase-shifting is:

$$\Delta\varphi = 2 \left[\arctan\left(\frac{Z_{INmax}}{Z_T}\right) - \arctan\left(\frac{Z_{INmin}}{Z_T}\right) \right]. \quad (\text{IV-6})$$

where $Z_{INmin} = \text{Im}(Z_{IN C=+\infty})$ and $Z_{INmax} = \text{Im}(Z_{IN C=0})$. According to (IV-3), (IV-4) and (IV-6) the relative phase shift can be written as:

$$\Delta\varphi = 2 \left[\arctan\left(\frac{\frac{-Z_1}{\tan\theta_1}}{Z_T}\right) - \arctan\left(\frac{Z_1 \tan\theta_1}{Z_T}\right) \right] \quad (\text{IV-7})$$

In order to get a phase shift $\Delta\varphi = 360^\circ$ equations (IV.7) have to be checked:

$$\arctan\left(\frac{\frac{-Z_1}{\tan\theta_1}}{Z_T}\right) = \pm 90^\circ \text{ and } \arctan\left(\frac{Z_1 \tan\theta_1}{Z_T}\right) = \mp 90^\circ \quad (\text{IV-8})$$

leading to:

$$\frac{\frac{-Z_1}{\tan\theta_1}}{Z_T} = \pm\infty \text{ and } \frac{Z_1 \tan\theta_1}{Z_T} = \mp\infty \quad (\text{IV-9})$$

The first solution for (IV-9) is $Z_T = 0 \Omega$ with Z_1 and $\tan\theta_1$ having finite values different from 0, which means θ_1 different from 0° . The second solution is $Z_1 = +\infty$ with Z_T and $\tan\theta_1$ having finite values different from 0. As Z_T and Z_1 have a limited value fixed by the technology, a relative phase shift of 360° cannot be reached. Once Z_T and Z_1 are fixed, when plotting $\Delta\varphi$ given by (IV-7) as a function of $\tan\theta_1$, it can be shown that $\Delta\varphi$ varied between minimum and maximum values. By equalling to 0 the derivative of $\Delta\varphi$, the condition $\tan\theta_1^2 = 1$ is obtained. For θ_1 ranging between 0 and 180° the two solutions of this condition are $\theta_1 = 45^\circ$ and 135° . They correspond either to a maximum or a minimum value of $\Delta\varphi$. A study about the sign of the derivative of $\Delta\varphi$ showed that $\theta_1 = 45^\circ$ and 135° correspond to a maximum and a minimum value of relative phase shift in the case $Z_1 > Z_T$, respectively. It is the opposite when $Z_1 < Z_T$. $Z_1 > Z_T$ is the most attractive condition as the maximal relative phase shift is obtained with a shorter θ_1 , 45° instead of 135° .

The varactor capacitance variation is also limited, and a series parasitic resistance should be taken into account. Hence the practical results may differ from the theoretical ones previously presented for an ideal circuit. In order to point out the practical limitations, Figure IV.2 shows the performances of the RTPS versus Z_1 , with $\theta_1 = 45^\circ$, C in the range

0.45-2.72 pF with $R = 1 \Omega$, corresponding to practically available varactors, and with a conventional ideal branch-line coupler $Z_T = 50 \Omega$, at a working frequency equal to 2 GHz. The formulas necessary to calculate the insertion loss and the phase shift of the RTPS presented in Figure IV.1, and taking into account R , are given in (B-3), (B-4), (B-6) and (B-7) in the Appendix-B.

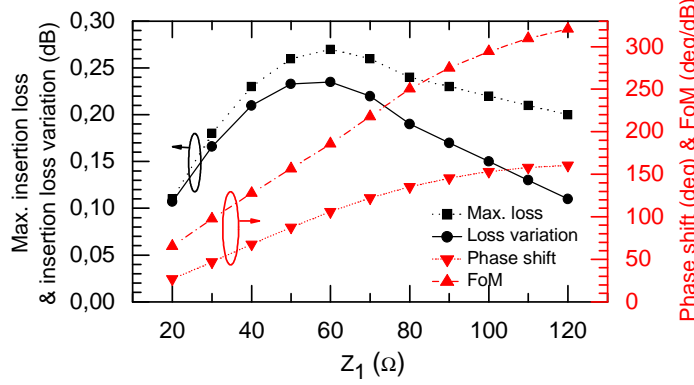


Figure IV.2: RTPS performances versus Z_1 with one varactor for each reflection load. $\theta_1 = 45^\circ$, $C [0.45-2.72]$ pF, $R = 1 \Omega$ and $Z_T = 50 \Omega$, at 2 GHz.

For the FoM calculation (IV-1), 0.3 dB of added losses were taken into account in order to consider the coupler insertion loss as estimated with ADS. Hence the FoM values are very realistic. As expected the phase shift increases with Z_1 (getting closer to the solution $Z_1 = +\infty$), whilst the maximal insertion loss, and so it is for the insertion loss variation, decrease after a maximum reached for 60 Ω . For $Z_1 = 120 \Omega$ the maximal insertion loss is quite low, leading to a high FoM of 318 $^\circ/\text{dB}$ for a phase shift of 160 $^\circ$. Figure IV.3 presents the performances of the RTPS versus θ_1 , with $Z_1 = 120 \Omega$, for the same varactor and Z_T than previously, at 2 GHz. For θ_1 between 0 and 360 $^\circ$, two points of maximum phase shift are obtained, one for $\theta_1 = 35^\circ$ and one for $\theta_1 = 215^\circ$ (e.g. $35^\circ + 180^\circ$), both leading to 168.6 $^\circ$ of phase shift. As the capacitance range variation is limited, equation (IV-7) determined with C in the range $[0; +\infty[$ is not valid anymore. Hence the condition $\theta_1 = 45^\circ$ with $Z_1 > Z_T$ leading to the highest phase variation is not strictly valid anymore. As a consequence, the optimal θ_1 is 35 $^\circ$ instead of 45 $^\circ$. Similarly, the two minimum relative phase shifts are reached for $\theta_1 = 125^\circ$ and 305 $^\circ$ (i.e. $125^\circ + 180^\circ$) instead of 135 $^\circ$ and 315 $^\circ$ (i.e. $135^\circ + 180^\circ$) as determined previously. Further, the maximal values of the insertion loss and relative phase shift are not reached for the same θ_1 . Consequently, θ_1 giving the maximal FoMs are slightly shifted as compared to the ones giving the maximal phase variation. Finally, the FoM is maximal for θ_1 equal to 45 $^\circ$ (same point which has been found in Figure IV.2) and 225 $^\circ$, and reaches 318 $^\circ/\text{dB}$ for 160 $^\circ$ of phase shift.

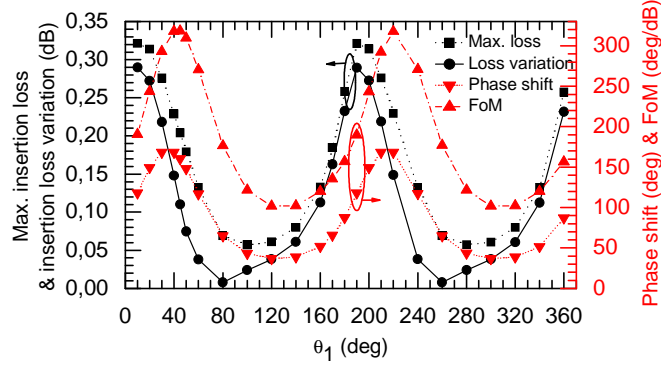


Figure IV.3: RTPS performances versus θ_1 with one varactor for each reflection load. $Z_1 = 120 \, \Omega$, $C [0.45-2.72] \, \text{pF}$, $R = 1 \, \Omega$ and $Z_T = 50 \, \Omega$, at 2 GHz.

In [21] it has been shown that by changing the output impedance Z_T , it is possible to increase the phase shift. Figure IV.4 shows the performances of the phase shifter versus Z_T , for $Z_1 = 120 \, \Omega$ and $\theta_1 = 45^\circ$, at 2 GHz.

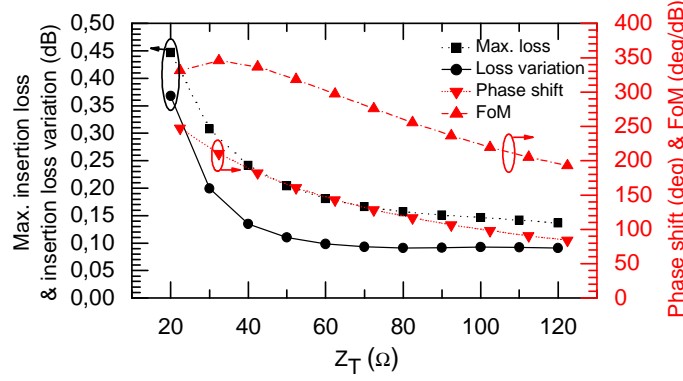


Figure IV.4: RTPS performances versus Z_T with one varactor for each reflection load. $Z_1 = 120 \, \Omega$, $\theta_1 = 45^\circ$, $C [0.45-2.72] \, \text{pF}$, $R = 1 \, \Omega$, at 2 GHz.

When Z_T decreases from $120 \, \Omega$ to about $40 \, \Omega$, the phase shift increases faster than the insertion loss. Hence a higher FoM is obtained. With Z_T below $40 \, \Omega$, it is possible to get phase shifts higher than 180° with a FoM higher than $300 \, ^\circ/\text{dB}$. For an optimal $Z_T = 30 \, \Omega$, the maximum FoM reaches $345 \, ^\circ/\text{dB}$ with a phase shift equal to 211° . As we can see from the theoretical then practical point of views presented in this section, Z_T , Z_1 and θ_1 have to be adjusted to reach a compromise between the maximal insertion loss, the insertion loss variation and the phase shift. For the chosen varactor the maximal phase shift that can be reached is limited to 247° . The purpose of the topologies presented in the next sections is to increase the phase shift.

IV.1.2 Reflection load with two varactors

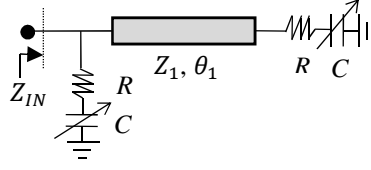


Figure IV.5: Proposed reflection load with two varactors

The previous topology gives really promising performances in terms of insertion loss, insertion loss variation, and FoM, but does not achieve 360° of phase shift needed in some applications. In order to get higher phase shift, another varactor was placed at the beginning of the load network, between the branch-line coupler output and the transmission line (Z_1, θ_1), as shown in Figure IV.5. The theoretical input impedance when considering ideal circuits, and neglecting R , can be written as:

$$Z_{IN} = j \frac{-Z_1 + Z_1^2 C \omega \tan \theta_1}{2Z_1 C \omega + \tan \theta_1 - Z_1^2 C^2 \omega^2 \tan \theta_1} \quad (\text{IV-10})$$

The structures proposed in [23] and [24] seem quite similar to ours. However, as shown in the first chapter, in [23], inductances and resistances were added and the varactors were connected in series with the transmission line. In [24], stubs were added between varactors and ground. Moreover, in both papers the electrical length of the transmission line was fixed to $\lambda/4$.

Considering an ideal capacitor, e.g. $R = 0 \, \Omega$ with a capacitance range $[0; +\infty[$, and an ideal transmission line, e.g. without losses and with Z_1 in the range $[0; +\infty[$, when the capacitor has the minimum value, $C = 0 \, \text{pF}$, the input impedance of the load obtained from (IV-10) is:

$$Z_{IN \, C=0} = j \frac{-Z_1}{\tan \theta_1} \quad (\text{IV-11})$$

When the capacitor has the maximal value, $C = +\infty$, the input impedance of the load is:

$$Z_{IN \, C=+\infty} = 0 \quad (\text{IV-12})$$

With the solutions (IV-11) and (IV-12) it seems that the maximal possible phase shift according to (IV-6) is 90° with $Z_1 = +\infty$ and θ_1 different from 0° . In practice, the variation of $\text{Im}(Z_{IN})$ with C is not monotonous as shown on Figure IV.6 so that the phase shift is greater than 360° , when considering an infinite variation of the capacitor. With a realistic variation of the capacitor, e.g. a varactor range of $0.45\text{-}2.72 \, \text{pF}$ as considered previously, the 360° phase shift cannot be reached, even after an optimization on Z_1 , θ_1 and Z_T . We will focus on that point more precisely by the following.

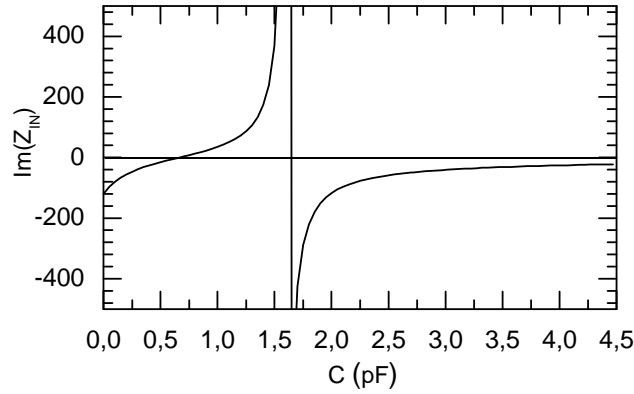


Figure IV.6: $\text{Im}(Z_{IN})$ versus C for reflection load with two varactors, $Z_1 = 120 \Omega$, $\theta_1 = 45^\circ$, $R = 0 \Omega$, at 2 GHz .

IV.1.3 Reflection load with three varactors

In order to get a 360° phase shift without complicating the topology of the load and with the same varactor without applying another bias voltage, a varactor was added in parallel of the second one, as shown in Figure IV.7. In that way, the value of the shunt capacitance is doubled.

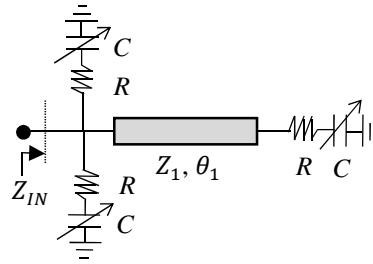


Figure IV.7: Proposed reflection load with three varactors

The input impedance of this load without considering R can be written as:

$$Z_{IN} = j \frac{-Z_1 + Z_1^2 C \omega \tan \theta_1}{3Z_1 C \omega + \tan \theta_1 - 2Z_1^2 C^2 \omega^2 \tan \theta_1} \quad (\text{IV-13})$$

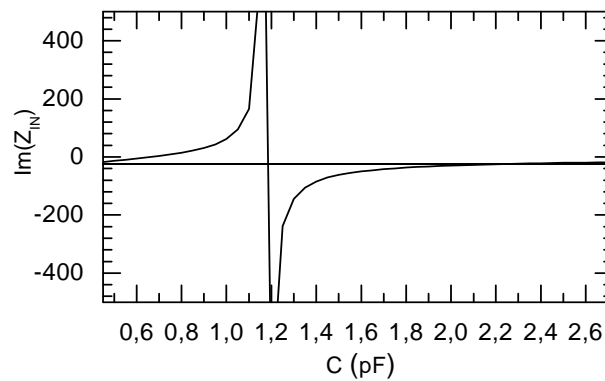


Figure IV.8: $\text{Im}(Z_{IN})$ versus C for reflection load with three varactors, $Z_1 = 120 \Omega$, $\theta_1 = 45^\circ$, $R = 0 \Omega$, at 2 GHz .

As for the load with two varactors, the variation of Z_{IN} with C is not monotonous, in Figure IV.8. Moreover, for the particular values of Z_1 , θ_1 and the variation of C chosen here, the extreme values of C lead to $Z_{IN\ c=0.45} \approx Z_{IN\ c=2.72} \approx -18$. Figure IV.9 shows the relative phase shift between the two extreme values of C with two and three varactors.

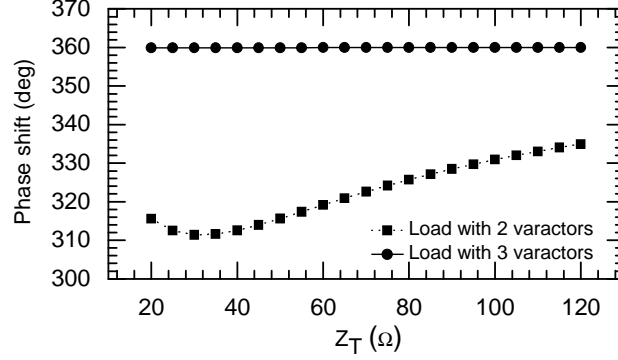


Figure IV.9: Relative phase shift of the RTPS versus Z_T with the loads of two or three varactors for each reflection load. $Z_1 = 120\ \Omega$, $\theta_1 = 45^\circ$, $C_{min} = 0.45\ \text{pF}$, $C_{max} = 2.72\ \text{pF}$, $R = 0\ \Omega$.

It is clear that the addition of a third varactor leads to a higher phase shift. The phase shift obtained with the reflection load with three varactors is equal to 360° , whatever the value of Z_T . This is due to $Z_{IN\ max} = \text{Im}(Z_{IN\ c=0.45}) \approx Z_{IN\ min} = \text{Im}(Z_{IN\ c=2.72})$, introduced in (IV-6). As we will see further, with other values of Z_1 , θ_1 it is possible to get phase shifts higher than 360° .

Figure IV.10 gives the RTPS return loss versus Z_T for the reflection loads with one and three varactors. The worst return loss in a 10 % bandwidth was considered. The lower Z_T leads to the worst return loss. With $Z_T = 20\ \Omega$, the return loss is 12.2 dB for the two kinds of reflection loads, whereas with $Z_T = 120\ \Omega$ it is 16.7 dB for the reflection load with one varactor and 17.4 dB with three varactors, respectively. This plot proves that the three varactors type reflection load allows the realization of a 360° phase shifter without scarifying the return loss, e.g. without any trade-off between the FoM and the return loss.

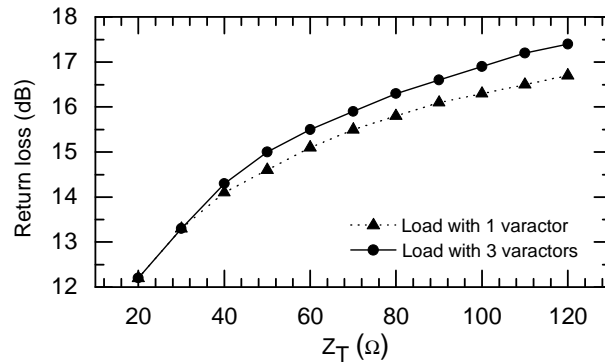


Figure IV.10: Worst return loss versus Z_T with loads carried out with one and three varactors for each reflection load. $Z_1 = 120\ \Omega$, $\theta_1 = 45^\circ$, $C [0.45-2.72]\ \text{pF}$, $R = 1\ \Omega$, at 2 GHz.

IV.2 Design procedure

The choice of the set of value θ_1 , Z_1 and Z_T results from a compromise between the maximal insertion loss, the insertion loss variation and the phase shift. An algorithm was used in order to select θ_1 , Z_1 and Z_T for each reflection load proposed here. It has been considered that the return loss should be always better than 10 dB in a 10 % bandwidth whatever the values of the parameters are. The algorithm is given in Figure IV.11.

First of all, a varactor has to be chosen which gives C_{min} , C_{max} and R . The limits of the characteristic impedance Z_1 , e.g. Z_{1min} and Z_{1max} , and the hybrid output impedance Z_T , e.g. Z_{Tmin} and Z_{Tmax} , are fixed by the technology. The insertion loss cannot be calculated only at the two extreme values of C because its variation may not be monotonous, so it has to be calculated for intermediate values. C_{step} was used as incremental value between C_{min} and C_{max} . Typically $C_{step} = 0.01$ pF is a good choice, with a good compromise between calculation time and accuracy. At the beginning, the maximal insertion loss IL_{max} , the maximal insertion loss variation ΔIL_{max} , the minimum phase shift $\Delta\phi_{min}$ and the working frequency $freq$ have to be fixed. The maximal phase shift is calculated with equations (B-3), (B-4), (B-6) and (B-7) for a load with one varactor and with equations (B-3), (B-5), (B-6), (B-7) for two or three varactors, respectively, given in Appendix-B. If the calculated phase shift is lower than the targeted one, one of the three parameters θ_1 , Z_1 or Z_T is incremented, otherwise the insertion loss is calculated for the intermediate values of C to deduce IL_{max} and ΔIL_{max} . If they are lower than the fixed criterions the solution is saved, else θ_1 , Z_1 or Z_T is incremented. If after all the combinations of θ_1 , Z_1 and Z_T any solution is found, this means that the goals are too ambitious and less constraints have to be applied in order to find a solution. At the end, the designer can select a solution among all the possible ones.

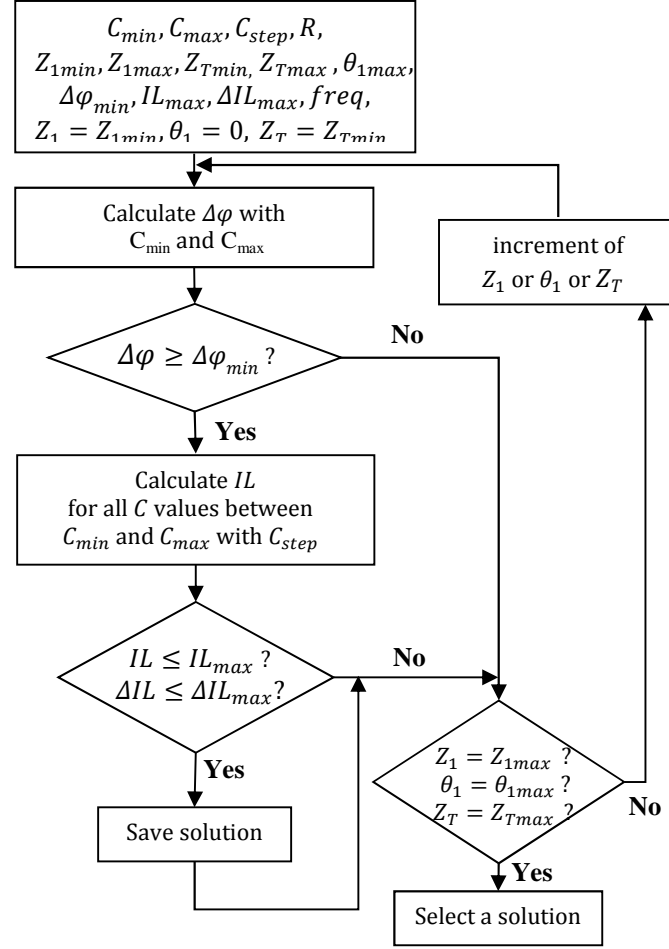


Figure IV.11: Algorithm for finding solutions

IV.3 Circuits design and experimental results in PCB

Three RTPS were fabricated to illustrate and validate the topologies and design methodology described in the last section, one with the reflection load presented in Figure IV.1, a second one with the reflection load presented in Figure IV.5 and cascaded with another phase shifter in order to reach 360° and finally a third one with the reflection load presented in Figure IV.7. In the three cases, the working frequency is 2 GHz and a SMD silicon hyperabrupt-junction varactor diode was used with $C_{min} = 0.45$ pF (20 V), $C_{max} = 2.72$ pF (0 V) and $R = 1 \Omega$. The technology limits the characteristic impedances of the microstrip transmission lines between 20 and 130Ω . The circuits were fabricated on Rogers RO4003 substrate, with relative effective permittivity 3.38 and thickness $813 \mu\text{m}$. All the measurements were carried out with a TRL calibration and the bias voltage was applied directly from the VNA through SMA connectors soldered on the board.

IV.3.1 Reflection load with one varactor

The optimisation procedure gives a maximal reachable phase shift of 270° with $Z_1 = 130 \Omega$, $\theta_1 = 35^\circ$ and $Z_T = 20 \Omega$. R leads to an amount of 0.59 dB of insertion loss and 0.53 dB of insertion loss variation. 0.3 dB of insertion loss were added in order to take into account the insertion loss of the branch-line coupler, leading to a total insertion loss equal to 0.89 dB. Hence the FoM of the RTPS was estimated to 303 °/dB. For a minimum 180° phase shift, a higher FoM with lower insertion loss could be reached. For example, an RTPS with $Z_1 = 116 \Omega$, $\theta_1 = 45^\circ$ and $Z_T = 30 \Omega$ achieves 211° of phase shift and gives the highest estimated FoM for a phase shift higher than 180° , with 346 °/dB. R adds 0.31 dB of insertion loss and only 0.2 dB of insertion loss variation.

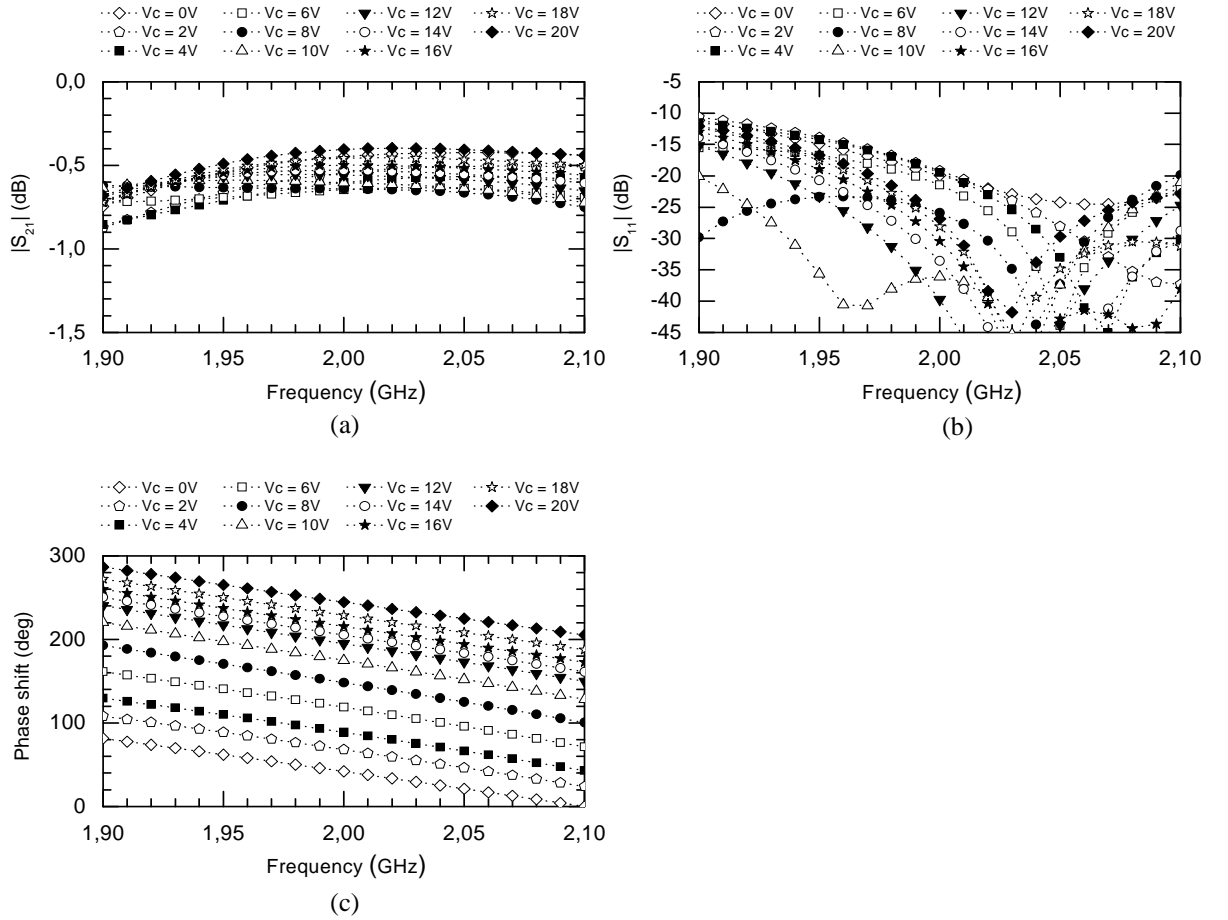


Figure IV.12: Simulated performances versus frequency, (a) insertion loss, (b) return loss, and (c) phase shift. Each reflection load is with one varactor, $Z_1 = 116 \Omega$, $\theta_1 = 45^\circ$ and $Z_T = 30 \Omega$.

Figure IV.12 shows the electrical simulation (with ADS) of this last RTPS, taking into account the losses due to the branch-line coupler. Simulations were carried out for the whole range of the varactors bias voltage, with a step of 2 V. The maximal insertion loss is 0.65 dB at 2 GHz, as shown in Figure IV.12(a), which is close to the estimated insertion loss in the FoM calculus (0.31 dB + 0.3 dB due to the branch-line), and the 0.25 dB of insertion loss variation also fits with the 0.2 dB theoretically calculated. The maximal

insertion loss is reached for a bias voltage of 6 V. As expected, the return loss is better than 10 dB over a 10 % bandwidth, as shown in Figure IV.12(b). It is better than 16 dB at 2 GHz. The reached phase shift is equal to 203° , as shown in Figure IV.12(c), and was reached for the maximum bias voltage of 20 V, as expected.

Figure IV.13(a) shows the viewgraph of the fabricated RTPS and Figure IV.13(b), (c) and (d) its measurement results. A very good agreement with the simulation results was obtained. As expected the RTPS is very low loss with 0.63 dB of maximal insertion loss and 0.18 dB of insertion loss variation. This means an average insertion loss of 0.54 dB with ± 0.09 dB of variation for 201° of phase shift at 2 GHz. The FoM of this RTPS is $318^\circ/\text{dB}$. The return loss reaches 22 dB at the working frequency and remains better than 10 dB over a 10 % bandwidth.

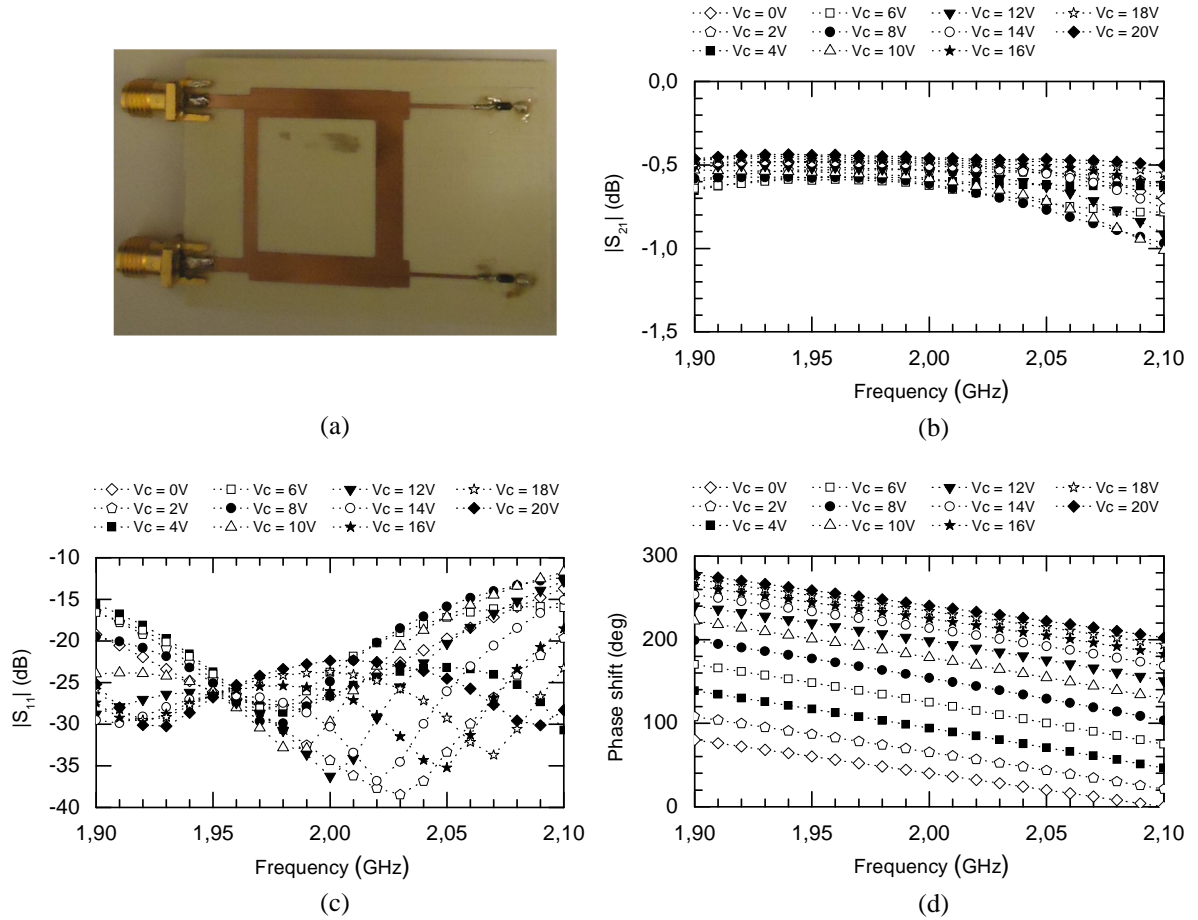


Figure IV.13: (a) Realized circuit. Measured performances versus frequency, (b) insertion loss, (c) return loss, and (d) phase shift. Each reflection load is with one varactor, $Z_1 = 116 \Omega$, $\theta_1 = 45^\circ$ and $Z_T = 30 \Omega$.

IV.3.2 RTPS with reflection load with two varactors cascaded with a Π -type phase shifter

The simplest method to get 360° of phase shift with the RTPS loaded with reflection loads with two varactors consists in cascading another phase shifter at the output port of the RTPS as shown in Figure IV.14(a). A simple Π -type phase shifter was chosen, as shown in

Figure IV.14(b). Both phase shifters, RTPS and Π -type, need to be optimized to the lowest insertion loss because they will be added in the global circuit. The Π -type phase shifter has to be built with the same varactor as for the RTPS in order not to complicate the bias voltage circuit and to have only one voltage control.

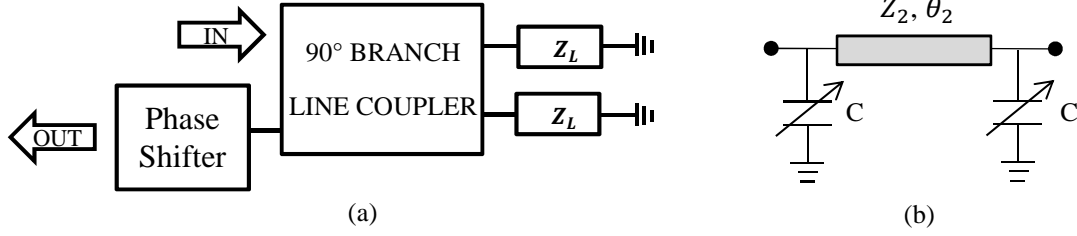


Figure IV.14: (a) RTPS cascaded with phase shifter. (b) Π -type phase shifter.

IV.3.2.1 Choice of the RTPS

The procedure presented in Figure IV.11 with the loads given in Figure IV.5, with the capacitor range 0.45-2.72 pF, $R = 1 \Omega$ and characteristic impedances ranging between 20 and 130 Ω , proposes a RTPS with 0.66 dB of insertion loss due to R and 0.6 dB of insertion loss variation, with $Z_1 = 130 \Omega$, $\theta_1 = 35^\circ$ and $Z_T = 20 \Omega$, at 2 GHz. The phase variation of such component is 335° . Figure IV.15 shows the electrical simulations (ADS) of this RTPS. The maximal insertion loss is 1.18 dB with 0.88 dB of insertion loss variation for 338° of phase shift at 2 GHz, leading to an expected FoM of 286 $^\circ/\text{dB}$. Comparing to the theoretical calculation with the loss due to R alone, 0.52 dB of insertion loss are added by taking into account the extra loss due to the TLs and junctions of the branch-line. The insertion loss variation is increased as well. The simulated (ADS) return loss in a 10 % bandwidth is better than 10 dB.

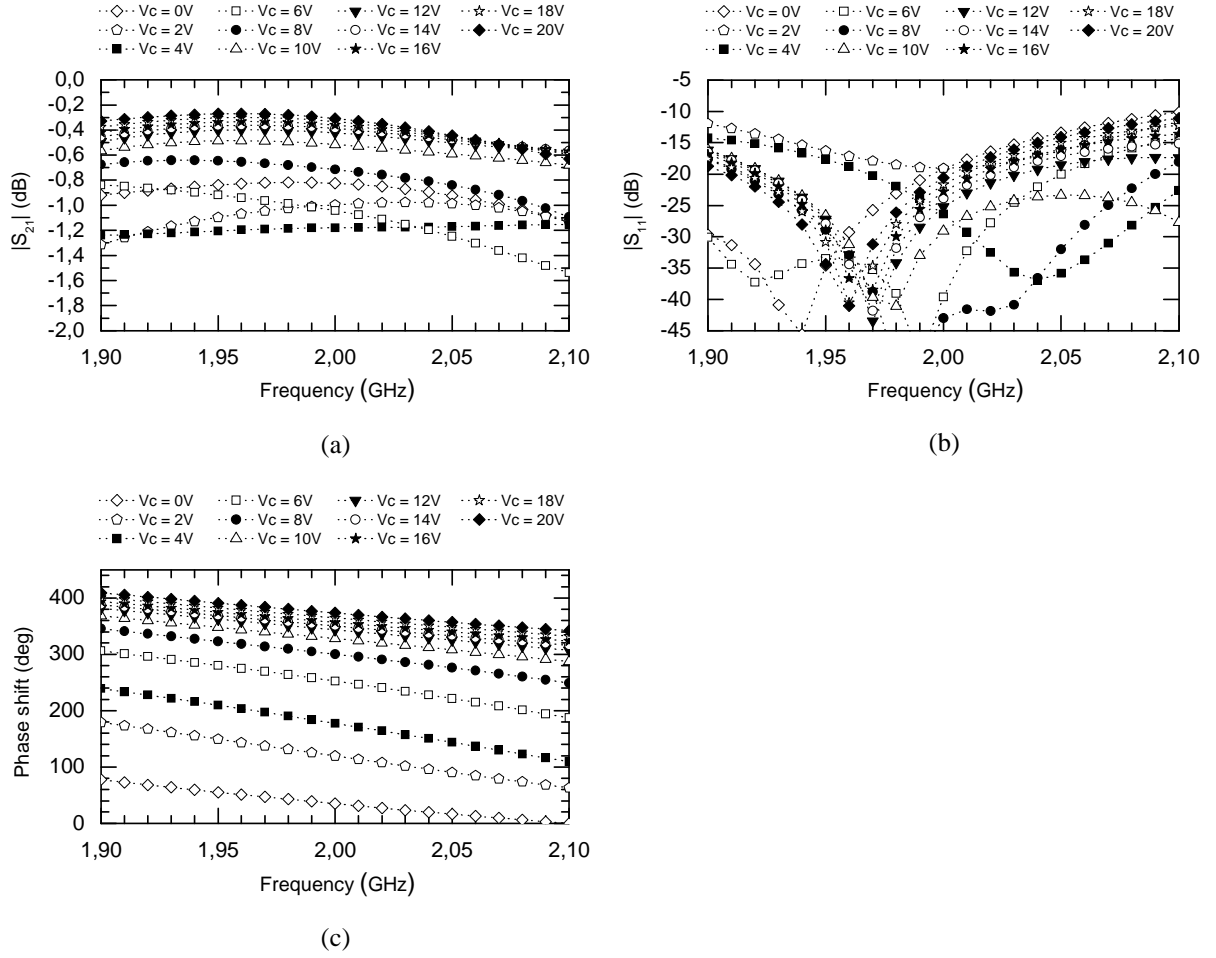


Figure IV.15: Simulated performances versus frequency. (a) Insertion loss, (b) return loss, (c) phase shift. Each reflection load is with two varactors. $Z_1 = 130 \Omega$, $\theta_1 = 35^\circ$ and $Z_T = 20 \Omega$.

IV.3.2.2 Optimization of the Π -type phase shifter

The characteristic impedance and the electrical length of the TL in the Π -type phase shifter, named (Z_2, θ_2) in Figure IV.14(b), has to be optimized to add minimal insertion loss, not to degrade the return loss and to complete the missing phase shift in order to reach 360° . Figure IV.16 shows the performances of the Π -type phase shifter optimized with $Z_2 = 130 \Omega$ and $\theta_2 = 20^\circ$ at 2 GHz and the same varactors as used previously. The phase shift is 82° . With the 338° of phase shift simulated with the previous RTPS, the added Π -type phase shifter will easily allow the designer to get 360° . The maximal insertion loss is 0.73 dB with 0.66 dB of insertion loss variation, a return loss of 17 dB in the worst case at 2 GHz, and 12 dB in the 10 % bandwidth. About 60 % of the phase variation is achieved between 0 and 2 V (among 20 V) which means a strong non-linearity. For this variation the level of insertion loss and insertion loss variation is high.

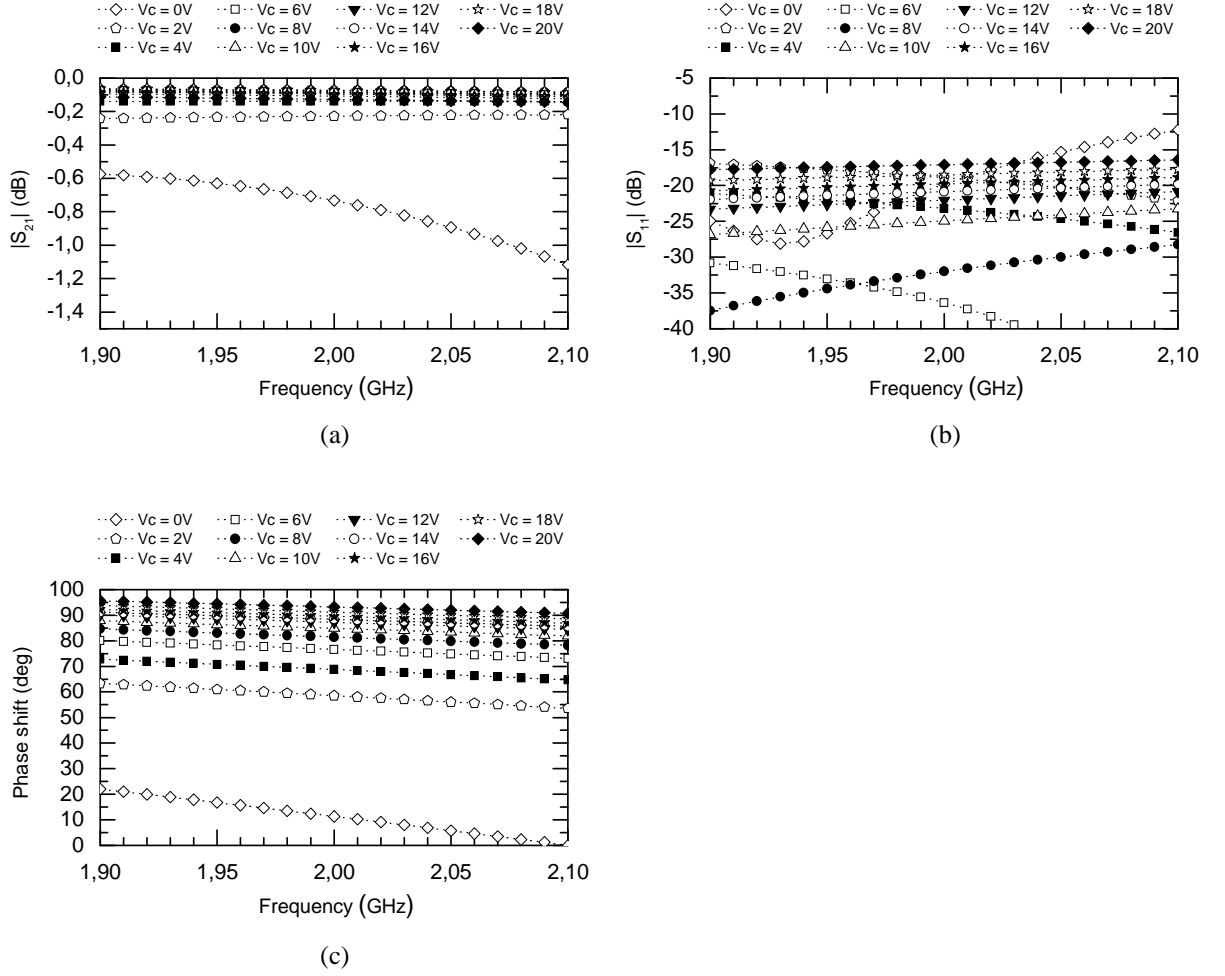


Figure IV.16: Simulated II-type phase shifter performances versus frequency. (a) Insertion loss, (b) return loss, (c) phase shift. $Z_2 = 130 \Omega$ and $\theta_2 = 20^\circ$.

IV.3.2.3 Simulation of the RTPS with the II-type phase shifter

The simulation results of the global phase shifter (RTPS cascaded with the II-type phase shifter) are shown in Figure IV.17. The maximal phase shift is 420° for a bias voltage between 0 and 20 V with a maximal insertion loss of 1.65 dB and 1.25 dB of insertion loss variation, leading to a FoM of $254^\circ/\text{dB}$. As no more than a full cycle is needed, for a bias ranging between 1 and 20 V, about 360° of phase shift is obtained with 1.3 dB of maximal insertion loss leading to a better FoM of $277^\circ/\text{dB}$. The insertion loss variation is reduced to 0.9 dB. Also, starting the bias voltage from 1 V instead of 0 V improves the worst matching over the 10 % bandwidth, from 6 dB to 9 dB.

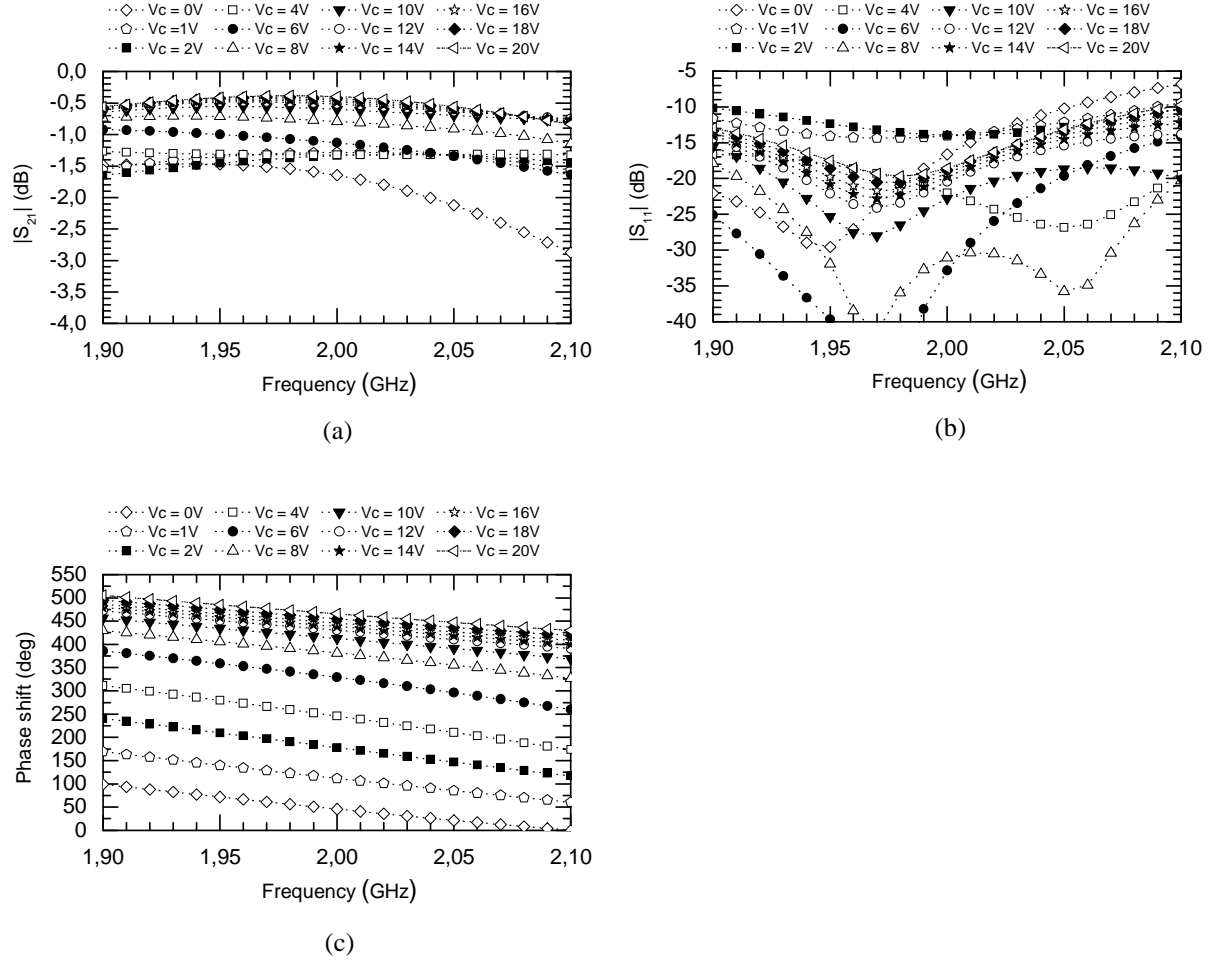


Figure IV.17: Simulated RTPS with II-type phase shifter performances versus frequency. (a) Insertion loss, (b) return loss, (c) phase shift. $Z_1 = 130 \Omega$, $\theta_1 = 35^\circ$ and $Z_T = 20 \Omega$, $Z_2 = 130 \Omega$ and $\theta_2 = 20^\circ$.

IV.3.2.4 Measurement results

The measured circuit is pictured in Figure IV.18(a) and its performances are given in Figure IV.18(b), (c) and (d). A maximal phase shift of 393° was obtained for a bias voltage ranging between 1.5 V and 20 V, as shown in Figure IV.18(d), with 1.97 dB of maximal insertion loss and 1.34 dB of insertion loss variation at 2 GHz, as shown in Figure IV.18(b). Below 1.5 V the insertion loss strongly increases. Between 1.8 V and 20 V, 362° of phase shift is achieved for 1.7 dB of maximal insertion loss and 1.12 dB of insertion loss variation, which means an average value of 1.14 ± 0.56 dB and a FoM of $213^\circ/\text{dB}$ at 2 GHz. The worst matching at the working frequency is 11.1 dB. It is only 6 dB in a 10 % bandwidth, as shown in Figure IV.18(c).

The technique consisting in cascading another phase shifter to the RTPS allows the phase shift to reach more than 360° leading to a FoM much higher than the state-of-the-art. However, the II-type phase shifter deteriorates the return loss of the global phase shifter which was an advantage of the RTPS as compared to the other phase shifters topologies.

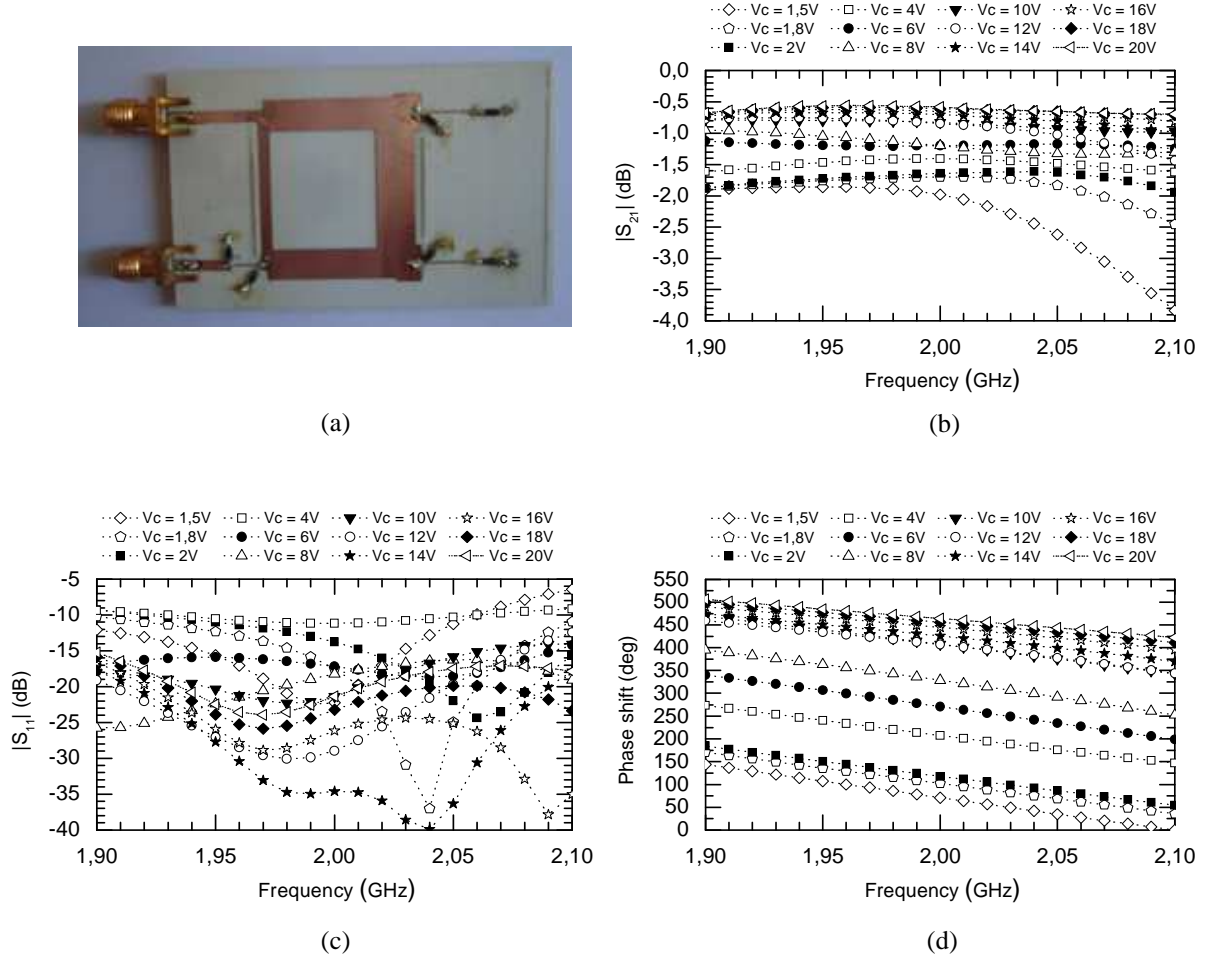


Figure IV.18: (a) Realized circuit. Measured performances versus frequency, (b) insertion loss, (c) return loss, and (d) phase shift. $Z_1 = 130 \Omega$, $\theta_1 = 35^\circ$ and $Z_T = 20 \Omega$, $Z_2 = 130 \Omega$ and $\theta_2 = 20^\circ$.

IV.3.3 Reflection load with three varactors

The purpose was to achieve a phase shift higher than 360° with the topology described in Figure IV.7. The design procedure led to a phase shift of 373° for 0.87 dB of insertion loss and 0.8 dB of insertion loss variation due to the resistance R , according to the theoretical formulas given in the Appendix-B, with $Z_1 = 120 \Omega$, $\theta_1 = 40^\circ$ and $Z_T = 30 \Omega$. Figure IV.19 shows the simulation results. The maximal insertion loss and insertion loss variation are 1.42 dB and 1.1 dB, respectively, as shown in Figure IV.19(a). The return loss is better than 11 dB over a 10 % bandwidth, see in Figure IV.19(b). The phase shift reaches 372° , Figure IV.19(c).

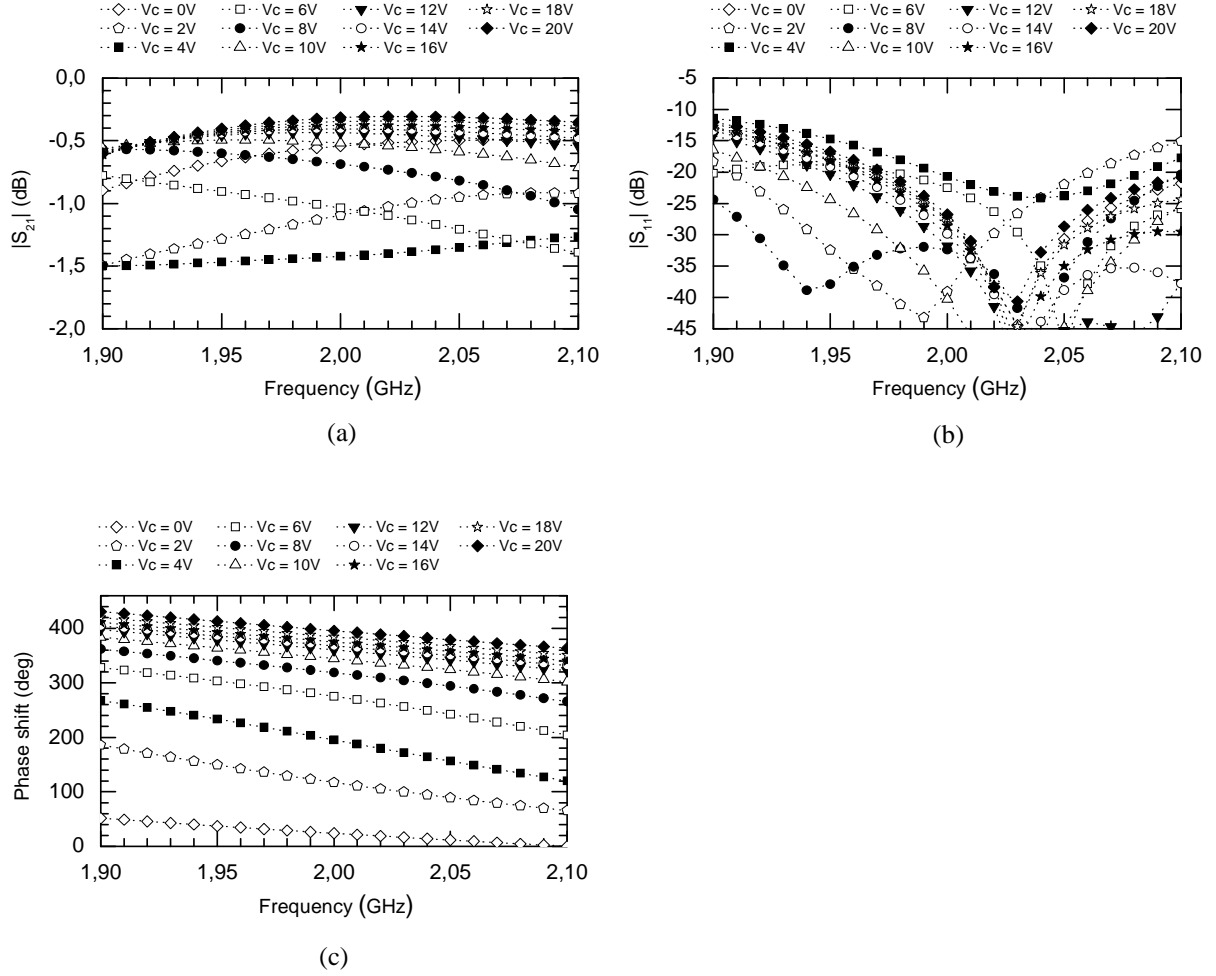


Figure IV.19: Simulated performances versus frequency, (a) insertion loss, (b) return loss, and (c) phase shift. 6 varactors. $Z_1 = 120 \Omega$, $\theta_1 = 40^\circ$ and $Z_T = 30 \Omega$.

Figure IV.20(a) shows the viewgraph of the fabricated RTPS and Figure IV.20(b), (c) and (d) its measurement results. Here again a very good agreement between measurement and simulation results was obtained. The insertion loss and insertion loss variation are 1.56 dB and 1.16 dB, respectively, at 2 GHz, as shown in Figure IV.20(b). This means an average insertion loss of 0.98 dB with ± 0.58 dB of variation for 385° of phase shift, as shown in Figure IV.20(d). The FoM of this device is $246^\circ/\text{dB}$. The return loss is 13.4 dB at the working frequency and better than 10.9 dB over a whole 10 % bandwidth, as shown in Figure IV.20(c). It is worth mentioning that the bias voltage varied from 0.5 to 20 V. It was not necessary to use a bias voltage lower than 0.5 V because a phase shift greater than 360° was reached anyway.

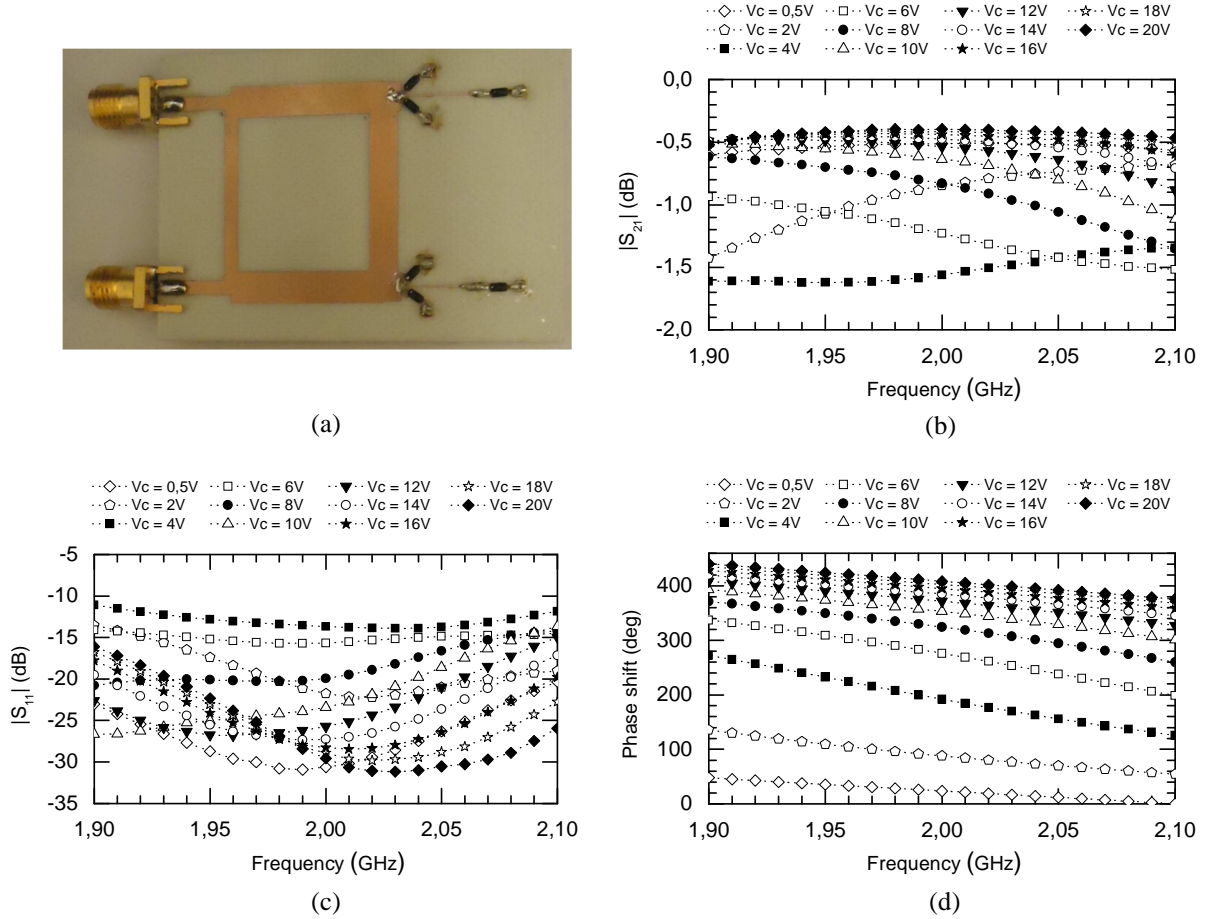


Figure IV.20: (a) Realized circuit. Measured performances versus frequency, (a) insertion loss, (b) return loss, and (c) phase shift. Each reflection load is with three varactors, $Z_1 = 120 \Omega$, $\theta_1 = 40^\circ$ and $Z_T = 30 \Omega$.

IV.3.4 Results synthesis

Total nb. of varactors /Topo. of the load	Average insertion loss (dB)		Insertion loss variation (dB)		Phase shift ($^\circ$)		Return loss over a 10 % BW (dB)		FoM ($^\circ$ /dB)	
	Simu. (ADS)	Meas- ment	Simu. (ADS)	Meas- ment	Simu. (ADS)	Meas- ment	Simu. (ADS)	Meas- ment	Simu. (ADS)	Meas- ment
2/Figure IV.1	0.525	0.54	± 0.125	± 0.09	203	201	10	10	312	318
6/Figure IV.5+II- type PS	0.85	1.14	± 0.45	± 0.56	360 [#]	362 ^{##}	9	6	277	213
6/Figure IV.7	0.87	0.98	± 0.55	± 0.58	372	385 [*]	11	10.9	262	246

[#]from 1V to 20V, ^{##}from 1.8V to 20V, ^{*}from 0.5V to 20V

Table IV.1: Sum up of the measured performances of the three achieved RTPS

Table IV.1 summarizes the simulated and measured results of the achieved RTPS at 2 GHz. Both fit really well for all the phase shifter. The simulated results are obtained thanks to circuit analysis on the basis of the topology characteristics determined by the

theoretical equations given in the Appendix-B and the design procedure explained previously.

The proposed RTPSs exhibit very high FoM. However, the second solution, consisting in cascading a RTPS with a Π -type phase shifter, leads to a lower FoM with higher insertion loss and bad return loss as compared to the third solution which uses 6 varactors too. Consequently, the last solution is better when a 360° phase shift is needed. For a phase shift lower than 200° , the first solution is more suitable, first because the FoM is much greater and also because only two varactors are needed which means a lower cost.

IV.4 RTPS in integrated technology

The insertion loss of the RTPS depends on the parasitic resistance of the varactor and on the loss of the circuit itself (transmission lines, junctions...). In [89], two RTPS were achieved at 2.45 GHz in a $0.18\ \mu\text{m}$ CMOS technology. For the first one, with a series-resonating load, it had been shown that 65 % of the 5.6 dB of insertion loss were due to the varactor load which had a minimal quality factor of 50. For the second RTPS, with a series-resonating load in Π -shape as shown in the first chapter, 86 % of the 11.9 dB of insertion loss were due to the varactors. The two varactors used in the load had minimal quality factors of 33 and 8. No similar analysis has been found at millimetre-wave frequency, but the high contribution of the varactor for the insertion loss should be even more important because of lower varactors quality factors at 60 GHz. In [90] varactors were used with a minimal quality factor of 15 at 60 GHz thanks to the use of differential poly/n-well MOS varactors having a better quality factor as compared to a single-ended varactor. However, even with such varactors the insertion loss is very high, 12.5 dB of maximal insertion loss for a 156° phase shift (as shown in the first chapter).

Here the purpose is to substitute the conventional reflection loads with varactors, by loaded line phase shifters carried out with S-CPW. In this case, it is possible to associate the performances of the loaded line phase shifter with the good matching of the RTPS.

IV.4.1 Topology of the reflection load based on a distributed loaded line phase shifter

The loaded line phase shifter was built with a S-CPW in which the capacitances between the ground and shielding strips can be periodically modified, as shown in Figure IV.21(a). The total physical length of the S-CPW was divided in eight similar segments where each segment is composed of ten groups of eight strips as shown in Figure IV.21(b). There is one variable capacitance per group of strips.

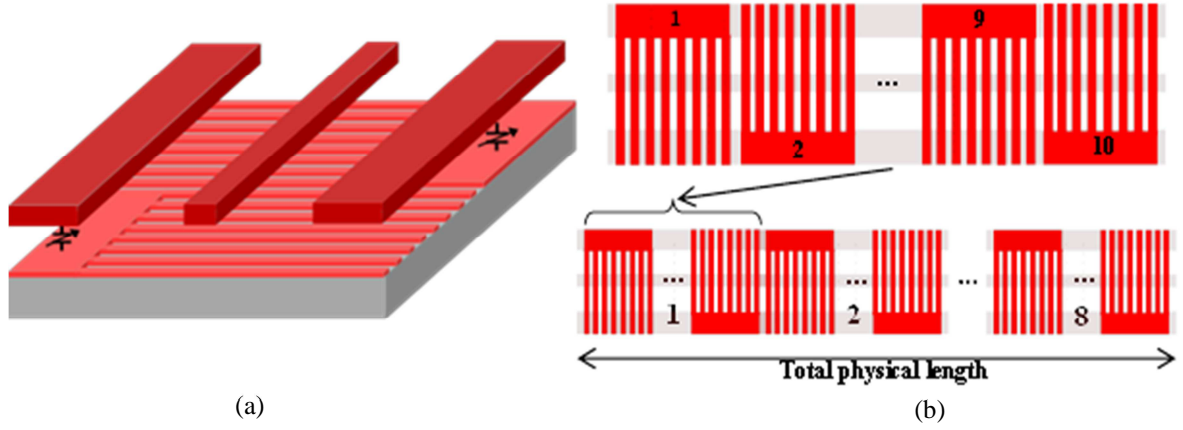


Figure IV.21: (a) Phase shifter based on capacitively switched S-CPW used as a reflection load. (b) Working principle.

All groups of strips in the segments are connected between them according to their position, e.g. all the groups number one are connected together, all the groups number two are connected together too and so on... Each capacitance has two states, one with a low value and one with a high value. This new type of loaded line phase shifter is currently under study and will lead to a patent demand, so for confidentiality reasons, no more information about how this two states capacitor is realized in practice can be given. The groups of finger are driven by a thermometer code, starting from zero to ten, leading to eleven configurations. Thanks to the variation of these capacitances, it is possible to modify the global capacitance of the transmission line, and hence to modify its relative effective permittivity ϵ_{reff} . As its physical length is fixed, when ϵ_{reff} increases, the phase of the S-CPW increases as well. The average characteristic impedance of this loaded line phase shifter is 22.5Ω . This loaded line phase shifter was simulated at 60 GHz in the 55 nm BiCMOS technology by STMicroelectronics. Its expected performances for the eight suitable configurations giving the best linearity, among eleven possible configurations, are shown in Figure IV.22.

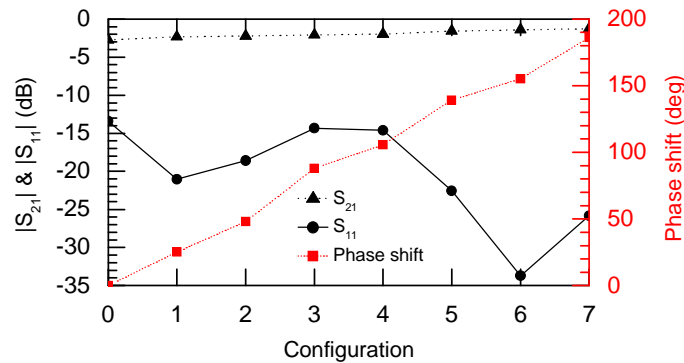


Figure IV.22: Simulated performances of the phase shifter for eight configurations at 60 GHz with a 22.5Ω system characteristic impedance.

By considering a 22.5Ω system characteristic impedance, the maximal phase shift is 186° for 2.74 dB of maximal insertion loss and 1.5 dB of insertion loss variation. The return loss is better than 14.3 dB at 60 GHz.

IV.4.2 Layout and simulation of the RTPS

The loaded line phase shifter based on S-CPW is terminated by a short circuit to serve as the loading network of the RTPS. The output ports impedance Z_T of the branch-line coupler was tuned to get the best compromise between the insertion loss, the insertion loss variation and the phase shift. The best choice was $Z_T = 27 \Omega$. The Z_0 ports impedance was kept equal to 50Ω . For these values of port impedance, the characteristic impedance of the two horizontal TLs and the vertical one between the loaded ports is 26Ω . For the vertical TL between the ports Z_0 , the characteristic impedance is 50Ω . The branch-line coupler was designed with S-CPW except the T-junctions which were designed with microstrip lines. The dimensions and simulated performances of these TLs have been given in the first chapter.

The layout of the RTPS is shown in Figure IV.23. The relative effective permittivity of the TLs varies according to the characteristic impedance. Consequently, the physical and electrical lengths of the S-CPW and microstrip TLs have to be adjusted in order to get a square shape for the branch-line coupler. The DC pads allow the variable capacitors to be controlled with the digital code.

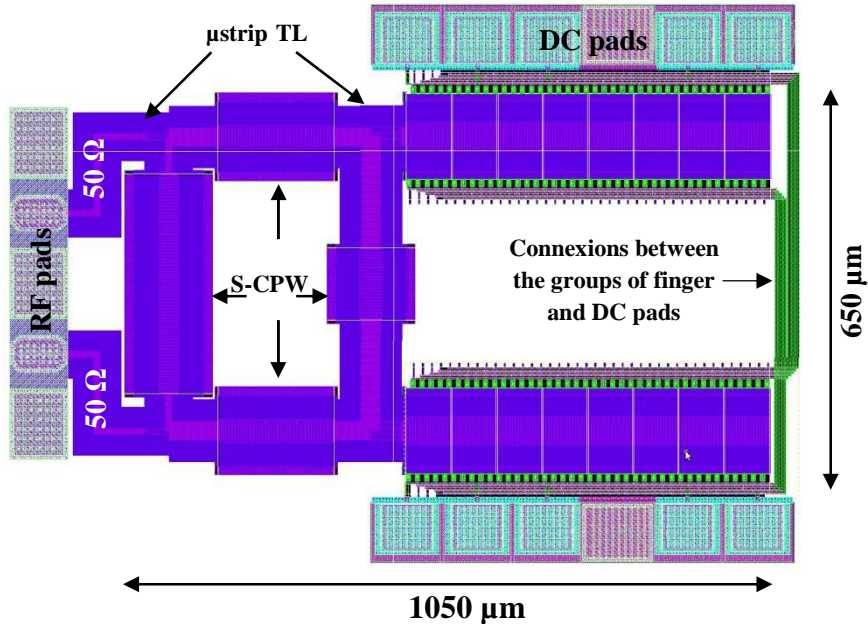


Figure IV.23: Layout of the RTPS in the BiCMOS 55 nm technology.

The simulation results, always for eight configurations at 60 GHz, are given in Figure IV.24. The maximal reachable phase shift is 341° with 6.44 dB of maximal insertion loss, 2.8 dB of insertion loss variation and a return loss better than 17.8 dB. This means an

average insertion loss of 5.04 dB with ± 1.4 dB of insertion loss variation. The expected FoM is 53 °/dB. With one more segment in the S-CPW phase-shifter, the RTPS could reach 360° of phase shift. The circuit covers an area equal to 0.68 mm^2 without taking into account the DC pads.

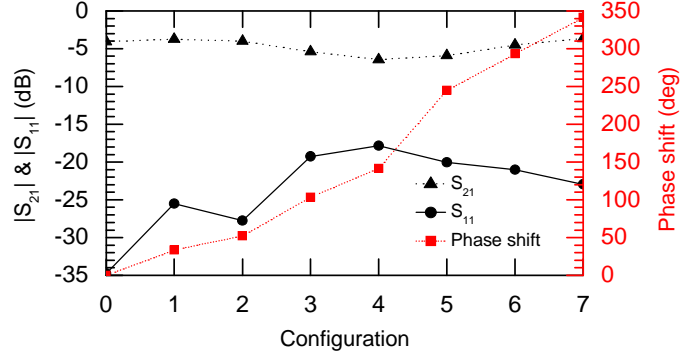


Figure IV.24: Simulated performances of the RTPS for eight configurations of the S-CPW phase shifter at 60 GHz.

IV.4.3 RTPS, loaded line phase shifter alone and state-of-the-art comparison

Another loaded line phase shifter based on S-CPW was designed and simulated with a phase shift around 360° , not to be used as a reflection load but to be compared with the proposed RTPS. The comparison of the simulated results with the state-of-the-art presented in Chapter I is given in Table IV.2. The loaded line phase shifter alone exhibits lower average insertion loss and insertion loss variation for a phase shift higher than 360° , consequently the FoM is higher. However, here again its structure obliges the ports impedance to be 22.5Ω , so if 50Ω ports connexions are required, matching networks have to be added, and so the area which is currently three times lower, and the insertion loss, will increase. Moreover, as expected, the return loss achieved by the loaded line phase shifter is not as good as the one achieved by the RTPS. The FoM of the proposed RTPS is more than twice higher as compared to the one of the other reflection type topologies.

Ref./Tech.	Freq. (GHz)	Architecture	Phase shift (°)	Average insertion loss (dB)	Insertion loss variation (dB)	Return loss (dB)	Return loss over a 10 % BW (dB)	Area (mm ²)	FoM (°/dB)
[65]/130nm SiGe	60	RT Varactor MOS	180	5.85	±1.65	-	-	0.18	24
[66]/quartz substrate	60	RT MEMS	135	4.25	±1.25	-14	-13	3.15	24.5
[67]/quartz substrate	60	SL MEMS	269.2	2.5	±0.5	-13	-12	4	89.7
[68]/90nm CMOS	60	SL without small-size capacitor	360	12.5	±2	<-10	<-10	0.28	24.8
[69]/quartz substrate	65	CPW Loaded MEMs	337	2.8	±0.8	-10	-10	9.45	93.6
[70]/65nm CMOS	60	Differential TL loaded MOS	156	9.25	±3.25	-13	-11	0.2	12.5
RTPS of this work	60	RT with loaded line phase shifter	341	5.04	±1.4	17.8	-	0.683	53
S-CPW phase shifter	60	Loaded line with a 22.5 Ω system	370	4.04	±1.27	10.6	-	0.234	70

Table IV.2: Comparison of the simulated performance of the RTPS with the S-CPW phase shifter and the state-of-the-art presented in Chapter I.

IV.5 Perspectives

Another type of reflection load is presented here and is currently under study for RF applications in the 1 GHz-10 GHz frequency range. Its schematic is given in Figure IV.25. It consists in basic LC cells, where C is a varactor and L a TL short enough to be considered as a lumped element at the working frequency. In Figure IV.25, two cells are drawn but the optimum number has to be fixed by an optimisation procedure. The LC cells are connected with two PIN diodes (PIN1 and PIN2) in parallel. The diodes have complementary voltage control, when PIN1 is ON, PIN2 is OFF, and vice versa. PIN1 is ended by a short-circuit and PIN2 by a load Z , which is consider so far as an infinite impedance.

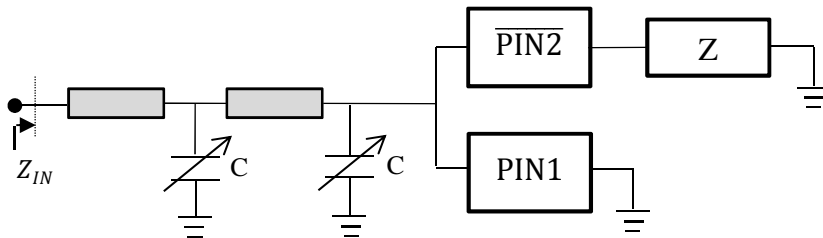


Figure IV.25: New proposed topology of reflection load.

The purpose of the PIN diodes is to switch the cells from either an open or a short circuit. This leads to a great difference of phase shift whereas the varactors allow a continuous and accurate phase shift variation. A first electrical simulation (not presented here) has shown that the two available relative phase shifts obtained with C , when the short and open circuits are successively switched, are not continuous: a gap in the phase shift appears between the two configurations. In the case where PIN1 is ON and PIN2 is OFF, the reflection load is short-circuited so Z_{IN} has the form:

$$Z_{IN} = jZ_c \tan(\theta) \quad (\text{IV-14})$$

whereas when PIN2 is ON and PIN1 is OFF, Z_{IN} has the form:

$$Z_{IN} = \frac{-jZ_c}{\tan(\theta)} \quad (\text{IV-15})$$

with Z_c and θ the parameters of the equivalent TL of the reflection load, without considering loss. It is obvious that the value Z_{IN} is really different between these two cases. Hence a gap appears in the phase shift. To get closer values of Z_{IN} , Z should have a pure imaginary finite value. Its value has to be optimized. This load can be achieved by a lumped or distributed element. With finely optimized LC cells and Z , 360° of phase shift with high FoM should be achieved.

The mix between digital control for high phase shift variation and analog control for accuracy makes this reflection load convenient in both PCB and integrated technology. For the latter, the varactors should be replaced by MEMS and PIN diodes built with transistors. For PCB technology, microstrip TLs should be used for LC cells instead of coplanar type usually used for loaded TLs. Indeed, really short TLs are expected, so with microstrip type TLs the varactors can be alternatively placed around the strip without touching each other. The varactors would be then connected to the ground through via holes.

IV.6 Conclusion

In all the topologies of RTPS, referenced in chapter I and using transmission lines with different manners, the authors fixed their electrical length to $\lambda/4$. In this chapter, it has been shown that this choice was not optimal, and for the devices optimised in a PCB technology a maximum of 45° of electrical length was used. In that case, a single transmission line in series with a varactor or between two or three varactors in parallel can lead to very high performances, as long as all the design parameters are optimized simultaneously.

A procedure was given in order to optimize the RTPS according to the minimal targeted phase shift, the maximal insertion loss and the insertion loss variation, depending on the chosen varactor and fabrication technology limits, and for a given return loss over a given bandwidth.

Concerning PCB technology, the first RTPS, with only one varactor for each reflection load, achieved a really high FoM of 318 °/dB for a maximal phase shift of 200° at 2 GHz. The second RTPS, with two varactors for each reflection load was optimized by simulation in order to get high FoM and phase shift close to 360°. However, it was not possible to reach 360° with this topology of reflection load with the chosen varactor. Hence, in order to get 360° of phase shift, a Π -type phase shifter was cascaded at the output port of the RTPS. The 213 °/dB of measured FoM for 362° of phase shift are really good but the return loss was sacrificed down to only 6 dB over a 10 % of bandwidth. Not to deteriorate the return loss and to keep the advantage of the RTPS comparing to other phase shifters topologies, a third RTPS with three varactors for each reflection load was achieved. It exhibited a phase shift higher than 360°, and a really high FoM of 246 °/dB was obtained. For the first and third RTPS the return loss over a 10 % bandwidth was better than 10 dB. The measured maximal phase shift, insertion loss and insertion loss variation showed very good agreement with the theoretical calculation prediction and electrical simulations, which demonstrates the efficiency of the proposed design procedure.

In silicon based integrated technology, a new type of phase shifter, based on S-CPW with variable capacitances between the grounds and floating strips, was used as a reflection load of a RTPS. Its purpose was to substitute for the varactors which have really low quality factor in integrated circuits, leading to a high level of insertion loss. The branch-line coupler was designed with S-CPWs in the 55 nm BiCMOS technology, with an impedance of 27 Ω at the loaded ports. The simulated phase shift of the RTPS is 341° for a FoM achieving 53 °/dB . For the S-CPW loaded line phase shifter alone, the simulated performances are better, with 370° of phase shift and a FoM of 70 °/dB. However, the major drawback of the latter is its structure which necessitates a system characteristic impedance of 22.5 Ω , far from the commonly used 50 Ω .

Finally a new concept of reflection load using digital and analog control was proposed in order to target a compact and accurate component, with high FoM for 360° of phase shift. This reflection load should be achievable in PCB technology as well as in integrated circuit.

Conclusion

Slow-wave coplanar waveguides were applied on several passive components to show their interest at millimetre-waves. Two baluns at the working frequency of 60 GHz, one with isolation based on a rat-race topology, and one without isolation based on a modified Wilkinson power divider, and a phase inverter alone, were realized and measured in a 65 nm CMOS technology. The measurement of the phase inverter proved that it is very large band. Moreover, it strongly reduces the area of the devices in which it takes place. However, concerning its simulation, more accuracy is needed for better prediction of the device performances. The areas of the rat-race and the modified Wilkinson power divider are 0.085 mm^2 and 0.1 mm^2 , respectively. Without RF probes connexion constraints, the area of the latter can be at least 25 % smaller. Both components showed a shift of the working frequency that could be easily adjustable, but in their working bandwidth the phase imbalance was $\pm 0.5^\circ$ in the worst case, which is excellent in comparison to the state-of-the-art. Then, a branch-line coupler and an in phase power divider without isolation were simulated at the working frequency of 60 GHz in a 28 nm CMOS technology. The simulation results were carried out with equivalent transmission lines characterized with the parameters Z_c , ϵ_{reff} and α of the simulated S-CPWs. Really good performances are expected for these compact devices.

Next, a new topology of in phase and isolated power divider was presented, leading to more flexibility and compactness. The input was loaded by a stub, and extra transmission lines for connecting the isolation resistance to the output ports were added. This component is perfectly suited to millimetre-wave frequencies. Two power dividers with different characteristics were realized in a PCB technology at 2.45 GHz as a proof-of-concept. They demonstrated the high level of flexibility and miniaturization. The simulation and measurement results are in very good accordance, showing the efficiency of the design method. Two 1:4 antenna arrays feeding networks were achieved at 2.45 and 5.8 GHz, respectively, in order to prove that thanks to the flexibility, the area of these feeding networks could be minimized. To confirm the efficiency of this new kind of power dividers in silicon technology, a component was designed at the working frequency of 60 GHz in a 55 nm BiCMOS technology with S-CPWs. It is currently being manufactured. The simulations results showed a low loss, full-matched and isolated component corresponding to the state-of-the-art.

Finally, two new topologies of reflection type phase shifters (RTPS) were presented, one for the RF band and one for the millimetre-wave one. As far as the RF band is concerned, the measurement results of a first version with only one varactor per reflection load exhibited a figure-of-merit of $318^\circ/\text{dB}$ for a maximum phase shift of 200° , which is much higher than the state-of-the-art. The insertion loss variation was only $\pm 0.09 \text{ dB}$. In

another version with three varactors per reflection load, the measurement results showed a phase shift reaching more than 360° with a figure-of-merit of 246 $^\circ/\text{dB}$, still much higher than the state-of-the-art. The insertion loss variation for this RTPS was ± 0.58 dB. For the two versions of RTPS the return loss was better than 10 dB over a 10 % bandwidth. The RTPS topology in the millimetre-wave band was based on a slow-wave coplanar waveguide loaded line phase shifter used as a reflection load. The design of this phase shifter was achieved thanks to the development of a new switched capacitor showing improved quality factor as compared with the varactors available in the design kit. Simulations, carried out in the 55 nm BiCMOS technology, demonstrated that 341° of phase shift could be reached with higher figure-of-merit than the state-of-the-art. The expected average insertion loss is 5.04 dB with ± 1.4 dB of insertion loss variation. The component is currently being manufactured.

Several short-term prospects can be drawn. The measurement results of the power divider and phase shifter up-coming in the 55 nm BiCMOS technology at the working frequency of 60 GHz should confirm the good expected performances. With a longer phase shifter in the reflection load of the RTPS, it would be possible to reach 360° of phase shift. Thanks to the new flexible power divider at 2.45 GHz and the new RTPS topology leading to a great figure-of-merit in RF, it will be also possible to build a beam-steering system for Wifi applications, at 2.45 GHz. Topologies are easily transferable to 5.8 GHz. Also, the substitution of the branch-line coupler by coupled lines in the RTPS is currently under study in both PCB and silicon technology, in order to increase the bandwidth and to reduce the area of the devices. Moreover, a novel type of reflection load mixing analog and digital phase shift control is also under development to further reduce the surface.

Mid-term prospects will concern the development of a complete beam-steering system by using the proposed devices in the millimetre-wave band. A hybrid integration of the antenna should be studied in order to get efficient and compact systems. A power balance approach will tell if power amplifier and low noise amplifiers should be added in the millimetre-wave front-end, after the transceiver. Differential phase shifters, which could be connected thanks to the developed baluns, could also be interesting in order to address the feeding of differential antenna arrays.

Finally, demonstrations should be now carried out at frequencies higher than 60 GHz in order to explore the potentialities of the 55 nm BiCMOS technology to address millimetre-wave imaging systems above 100 GHz.

Appendix-A

This appendix aims at demonstrating the formulas (III-31) to (III-34) of the S -parameters. According to the Figure III.6 we can write b_4 as:

$$b_4 = b_{4_e} + b_{4_o} = S_{11_e} \cdot a_{4_e} + S_{12_e} \cdot a_{2_e} + S_{11_o} \cdot a_{4_o} + S_{12_o} \cdot a_{2_o} \quad (\text{A-1})$$

From (III-24), it is easy to deduce:

$$a_{4_e} = \frac{a_4 + a_5}{2}, a_{2_e} = \frac{a_2 + a_3}{2}, a_{4_o} = \frac{a_4 - a_5}{2} \text{ and } a_{2_o} = \frac{a_2 - a_3}{2} \quad (\text{A-2})$$

Because of the shunt at the port 1:

$$S_{12_o} = 0 \text{ and } S_{11_o} = -1 \quad (\text{A-3})$$

So with (A-2) and (A-3), (A-1) can be rewritten as:

$$b_4 = S_{11_e} \cdot \left(\frac{a_4 + a_5}{2} \right) + S_{12_e} \cdot \left(\frac{a_2 + a_3}{2} \right) - \left(\frac{a_4 - a_5}{2} \right) \quad (\text{A-4})$$

and then as:

$$b_4 = \frac{S_{11_e} - 1}{2} \cdot a_4 + \frac{S_{11_e} + 1}{2} \cdot a_5 + \frac{S_{12_e}}{2} \cdot a_2 + \frac{S_{12_e}}{2} \cdot a_3 \quad (\text{A-5})$$

In the same way, b_5 can be expressed by:

$$b_5 = b_{5_e} + b_{5_o} = S_{11_e} \cdot a_{5_e} + S_{12_e} \cdot a_{3_e} + S_{11_o} \cdot a_{5_o} + S_{12_o} \cdot a_{3_o} \quad (\text{A-6})$$

It can be deduced from Figure III.6 that:

$$a_{3_o} = -a_{2_o} \text{ and } a_{5_o} = -a_{4_o} \quad (\text{A-7})$$

and that:

$$a_{4_e} = \frac{a_{1_e}}{\sqrt{2}} = a_{5_e} \quad (\text{A-8})$$

So that we can rewrite (A-6) as

$$\begin{aligned} b_5 &= S_{11_e} \cdot a_{4_e} + S_{12_e} \cdot a_{2_e} - S_{11_o} \cdot a_{4_o} - S_{12_o} \cdot a_{2_o} \\ &= S_{11_e} \cdot \left(\frac{a_4 + a_5}{2} \right) + S_{12_e} \cdot \left(\frac{a_2 + a_3}{2} \right) + \left(\frac{a_4 - a_5}{2} \right) \\ &= \frac{S_{11_e} + 1}{2} \cdot a_4 + \frac{S_{11_e} - 1}{2} \cdot a_5 + \frac{S_{12_e}}{2} \cdot a_2 + \frac{S_{12_e}}{2} \cdot a_3 \end{aligned} \quad (\text{A-9})$$

Then adding b_4 (A-5) and b_5 (A-9) we get:

$$b_4 + b_5 = S_{11_e} \cdot a_4 + S_{11_e} \cdot a_5 + S_{12_e} \cdot a_2 + S_{12_e} \cdot a_3 \quad (\text{A-10})$$

With (III-24) and (A-8), and as $a_{5_o} = -a_{4_o}$ (A-7), the addition of a_4 and a_5 can be simplified to:

$$a_4 + a_5 = a_{4_o} + a_{4_e} + a_{5_o} + a_{5_e} = \sqrt{2} \cdot a_{1_e} = \sqrt{2} \cdot a_1 \quad (\text{A-11})$$

In the same way:

$$b_4 + b_5 = \sqrt{2} \cdot b_1 \quad (\text{A-12})$$

We obtain from (A-10), (A-11) and (A-12):

$$b_1 = S_{11_e} \cdot a_1 + \frac{S_{12_e}}{\sqrt{2}} \cdot a_2 + \frac{S_{12_e}}{\sqrt{2}} \cdot a_3 \quad (\text{A-13})$$

Consequently, it is easy to conclude that:

$$\begin{aligned} S_{11} &= S_{11_e} \\ S_{12} &= S_{13} = \frac{S_{12_e}}{\sqrt{2}} \end{aligned} \quad (\text{A-14})$$

The three missing S -parameters can be calculated thanks to the equations at port 2 as the following:

$$b_2 = b_{2_e} + b_{2_o} = S_{22_e} \cdot a_{2_e} + S_{12_e} \cdot a_{4_e} + S_{22_o} \cdot a_{2_o} + S_{12_o} \cdot a_{4_o} \quad (\text{A-15})$$

With (A-2) and (A-3), (A-15) is written as:

$$b_2 = S_{22_e} \cdot \left(\frac{a_2 + a_3}{2} \right) + S_{12_e} \cdot \left(\frac{a_4 + a_5}{2} \right) - S_{22_o} \cdot \left(\frac{a_2 - a_3}{2} \right) \quad (\text{A-16})$$

Finally, (A-11) and (A-16) are combined to get:

$$b_2 = \frac{S_{12_e}}{\sqrt{2}} \cdot a_1 + \frac{S_{22_e} - S_{22_o}}{2} \cdot a_2 + \frac{S_{22_e} + S_{22_o}}{2} \cdot a_3 \quad (\text{A-17})$$

The three others S -parameters can be now obtained:

$$\begin{aligned} S_{21} &= \frac{S_{12_e}}{\sqrt{2}} \\ S_{22} &= \frac{S_{22_e} - S_{22_o}}{2} \\ S_{23} &= \frac{S_{22_e} + S_{22_o}}{2} \end{aligned} \quad (\text{A-18})$$

Appendix-B

This appendix aims to give the formulas to calculate the insertion loss and phase shift of the RTPS as described in Figure IV.1, with the reflective loads of Figure IV.1, Figure IV.5 or Figure IV.7. Ideal transmission lines and branch-line coupler were considered, but the varactor series resistance R was taken into account. Z_{IN} can be written as:

$$Z_{IN} = \frac{E + jF}{G} \quad (\text{B-1})$$

where E , F and G are variables depending on the load topology that are defined below. The reflection coefficient Γ can be written as:

$$\Gamma = \frac{Z_{IN} - Z_T}{Z_{IN} + Z_T} = \frac{E - G \times Z_T + jF}{E + G \times Z_T + jF} \quad (\text{B-2})$$

The transmission parameter S_{21} of a RTPS is by definition equal to $j\Gamma$, so the magnitude of S_{21} can be written as:

$$|S_{21}| = |\Gamma| = \sqrt{\frac{(E - G \times Z_T)^2 + F^2}{(E + G \times Z_T)^2 + F^2}} \quad (\text{B-3})$$

The phase shift is calculated with (IV-6) and (B-1). The equality of (IV-6) is not true anymore; it is about equal, exactly as it was the case in chapter I. This is due to the low value of R , leading to a real part of Z_{IN} quite negligible as compared to its imaginary part and as compared to Z_T . The variables E , F and G depend on the reflection load topology.

- For the reflection load in Figure IV.1:

$$\begin{aligned} E &= AC + BD \\ F &= AD - BC \\ G &= C^2 + D^2 \end{aligned} \quad (\text{B-4})$$

- For the reflection loads in Figure IV.5 and Figure IV.7:

$$\begin{aligned} E &= ACR_2^2 + BDR_2^2Q_2^2 + A^2R_2 + ACR_2^2Q_2^2 + BDR_2^2 \\ &\quad + B^2R_2 \\ F &= -BCR_2^2 + ADR_2^2Q_2^2 - A^2R_2Q_2 - BCR_2^2Q_2^2 + ADR_2^2 \\ &\quad - B^2R_2Q_2 \\ G &= (CR_2 - DR_2Q_2 + A)^2 + (CR_2Q_2 + DR_2 + B)^2 \end{aligned} \quad (\text{B-5})$$

In both cases, the parameters A , B , C and D can be written as:

$$\begin{aligned}
 A &= Z_1^2 R_1^2 - Z_1^2 R_1^2 Q_1^2 + Z_1^4 \tan^2 \theta_1 \\
 B &= 2Z_1^2 R_1^2 Q_1 \\
 C &= Z_1^2 R_1 + Z_1^2 R_1 \tan^2 \theta_1 + 2Z_1 R_1^2 Q_1 \tan \theta_1 \\
 D &= Z_1^2 R_1 Q_1 \tan^2 \theta_1 + Z_1 R_1^2 Q_1^2 \tan \theta_1 - Z_1 R_1^2 \tan \theta_1 \\
 &\quad + Z_1^2 R_1 Q_1 + Z_1^3 \tan \theta_1
 \end{aligned} \tag{B-6}$$

with R_1 and R_2 the parasitic resistances, and Q_1 and Q_2 the quality factor of the varactors at the end of the transmission line (Z_1, θ_1) and at the output port of the branch-line coupler, respectively. In Figure IV.5, $R_2 = R_l$ and $C_2 = C_l$ while in Figure IV.7, $R_2 = \frac{1}{2} R_l$ and $C_2 = 2C_l$. The quality factor is defined as:

$$Q_n = \frac{1}{R_n \cdot C_n \cdot \omega} \tag{B-7}$$

References

- [1] A.-L. Franc, “Lignes de propagation intégrées à fort facteur de qualité en technologie CMOS—Application à la synthèse de circuits passifs millimétriques,” Thesis, University of Grenoble, July 2011.
- [2] X. Tang, “Apport des lignes à ondes lentes S-CPW aux performances d’un front-end millimétrique en technologie CMOS avancée,” Thesis, University of Grenoble, Oct. 2012.
- [3] E. J. Wilkinson, “An N-way hybrid power divider,” *IEEE Trans. Microw. Theory and Tech.*, vol. 8, pp. 116-118, Jan. 1960.
- [4] L. I. Parad and R. L. Moynihan, “Split-tee power divider,” *IEEE Trans. Microw. Theory and Tech.*, vol. 13, pp. 91-95, Jan. 1965.
- [5] H. Liu, Z. Li, and X. Sun, “Compact defected ground structure in microstrip technology,” *Electron. Lett.*, vol. 41, no. 3, pp. 132-134, Feb. 2005.
- [6] F. Tao, X. Jun, W. M. Yan, “Design of 1:3 unequal Wilkinson power divider with defected ground structure,” *Microwave and Millimeter Wave Technology (ICMMT), 2010 International Conference on*, pp. 646-648, May 2010.
- [7] J.-X. Chen and Q. Xue, “Novel 5:1 unequal Wilkinson power divider using offset double-sided parallel-strip lines,” *IEEE Microw. Wireless Components Letters*, vol. 17, no. 3, pp. 175–177, 2007.
- [8] M. Moradian and H. Oaraizi, “Application of grooved substrates for design of unequal Wilkinson power dividers,” *Electron. Lett.*, vol. 44, no. 1, pp. 32-33, Jan. 2008.
- [9] T. Yang, J.-X. Chen, and Q. Xue, “Novel Approach to the Design of Unequal Power Divider with High-Dividing Ratio,” *IEEE Microw. Wireless Components Letters*, vol. 51, no. 5, pp. 1240–1243, May 2009.
- [10] M. Strackx, K. Janssen, E. D’Agostino, G.A.E. Vandenbosch, P. Reynaert, P. Leroux, “Ultra-wideband antipodal Vivaldi antenna array with Wilkinson power divider feeding network,” *Ultra-Wideband (ICUWB), 2011 IEEE International Conference on*, pp.1-4, 14-16 Sept. 2011.
- [11] C.-H. Ko, K. M. J.Ho, and G. M. Rebeiz, “An Electronically-Scanned 1.8–2.1 GHz Base-Station Antenna Using Packaged High-Reliability RF MEMS Phase Shifters,” *IEEE Trans. Microw. Theory Tech.*, vol. 61, no. 2, pp. 979–985, Feb. 2013.
- [12] Pozar D. M., *Microwave Engineering*, 3rd ed. New York: Wiley, 2005.
- [13] H.-R. Ahn and I.Wolff, “Arbitrary power division branch-line hybrid terminated by arbitrary impedances,” *Electron. Lett.*, vol. 35, no. 7, pp. 572-574, April 1999.

- [14] D.-H. Kim and J.-S. Rieh, "CMOS 138 GHz low-power active mixer with branch-line coupler," *Electronics Letters*, vol. 48, no. 10, pp. 554-555, May 2012.
- [15] W. A. Tyrrel, "Hybrid circuits for microwaves," *IEEE Proc. Inst. Radio Eng.*, vol. 35, no. 11, pp. 1294-1306, Nov. 1947.
- [16] C. Y. Pon, "Hybrid ring directional couplers for arbitrary power division," *IEEE Trans. Microw. Theory Tech.*, vol. 9, pp. 529-535, Nov. 1961.
- [17] M. K. Mandal and S. Sanyal, "Reduced-Length Rat-Race Couplers," *IEEE Trans. Microw. Theory Tech.*, vol. 55, no. 12, pp. 2593-2998, Dec. 2007.
- [18] W. Zhao, Y. Zhang, M. Zhan, "Design and performance of a W-band microstrip rat-race balanced mixer," *Microw. and Millim Wave Technology (ICMMT)*, 2010 International Conference on, pp.713-716, 8-11 May 2010.
- [19] O. García-Pérez, V. González-Posadas, L. E. García-Muñoz, and D. Segovia-Vargas, "Noise-Figure Measurement of Differential Amplifiers Using Non ideal Baluns," *IEEE Trans. Microw. Theory Tech.*, vol. 58, no. 6, pp. 1658-1664, June 2011.
- [20] R. H. Hardin, E. J. Downey, and J. Munushian, "Electronically-variable phase shifters utilizing variable capacitance diodes," *Proc. Inst. Radio Eng.*, vol. 48, no. 5, pp. 944-945, May 1960.
- [21] C.-S. Lin, S.-F. Chang, C.-C. Chang, and Y.-H. Shu, "Design of a Reflection-Type Phase Shifter With Wide Relative Phase Shift and Constant Insertion Loss," *IEEE Trans. Microw. Theory Tech.*, vol. 55, no. 9, pp. 1862-1868, Sep. 2007.
- [22] J.-C. Wu, T.-Y. Chin, S.-F. Chang, and C.-C. Chang, "2.45-GHz CMOS Reflection-Type Phase-Shifter MMICs With Minimal Loss Variation Over Quadrants of Phase-Shift Range," *IEEE Trans. Microw. Theory Tech.*, vol. 56, no. 10, pp. 2180-2189, Oct. 2008.
- [23] C.-S. Lin, S.-F. Chang, and W.-C. Hsiao, "A Full-360 Reflection-Type Phase Shifter With Constant Insertion Loss," *IEEE Microw. Wireless Comp. Lett.*, vol. 18, no. 2, pp. 106-108, Feb. 2008.
- [24] T.-W. Yoo, J.-H. Song and M.-S. Park, "360° reflection-type analogue phase shifter implemented with a single 90° branch-line coupler," *Electron. Lett.*, vol. 33, no. 3, pp. 224-226, Jan. 1997.
- [25] K.-O. Sun, H.-J. Kim, C.-C. Yen, and D. van der Weide, "A Scalable Reflection Type Phase Shifter With Large Phase Variation," *IEEE Microw. Wireless Comp. Lett.*, vol. 15, no. 10, pp. 647-648, Oct. 2005.
- [26] D. Kim, Y. Choi, M. G. Allen, J. S. Kenney, and D. Kiesling, "A Wide-Band Reflection-Type Phase Shifter at S-Band Using BST Coated Substrate," *IEEE Trans. Microw. Theory Tech.*, vol. 50, no. 12, pp. 2903-2909, Dec. 2012.

- [27] A. M. Abbosh, "Compact Tunable Reflection Phase Shifters Using Short Section of Coupled Lines," *IEEE Trans. Microw. Theory Tech.*, vol. 60, no. 8, pp. 2465-2472, Aug. 2012.
- [28] H.-R. Ahn and T. Itoh, "Compact impedance-transforming 3-dB three-port power dividers with modified asymmetric impedance transformers (MCCTs)," *IEEE MTT-S Int. Microw. Symp. Dig.*, pp. 1-4, 2011.
- [29] C.-H. Tseng, and C. H. Wu, "Compact planar Wilkinson power divider using π -equivalent shunt-stub-based artificial transmission lines," *Electron. Lett.*, vol. 46, no. 19, pp. 1327-1328, Sep. 2010.
- [30] C.-H. Wu, and C.-H. Tseng, "A compact branch-line coupler using π -equivalent shunt-stub-based artificial transmission lines," *Asia-Pacific Microw. Conf. Dig.*, pp. 802-805, 2010.
- [31] C.-H. Tseng, and H.-J. Chen, "Compact rat-race coupler using shunt-stub-based artificial transmission lines," *IEEE Microw. Wireless Comp. Lett.*, vol. 18, no. 11, pp. 734-736, Nov. 2008.
- [32] M. H. Awida, A. M. E. Safwat, and H. El-Hennawy, "Compact rat-race hybrid coupler using meander space-filling curves," *Microw. Opt. Technol. Lett.*, vol. 48, no. 3, pp. 606-609, March 2006.
- [33] H. Ghali and T. A. Moselhy, "Miniaturized fractal rat-race, branch-line, and coupled-line hybrids," *IEEE Trans. Microw. Theory Tech.*, vol. 52, no. 11, pp. 2513-2520, Nov. 2004.
- [34] S. March, "A wideband stripline hybrid ring," *IEEE Trans. Microw. Theory Tech.*, vol. 16, no. 6, pp. 361, June 1968.
- [35] M.-H. Mutgulescu, E. Penard, and I. Zaquine, "Design formulas for generalised 180° hybrid ring couplers," *Electron. Lett.*, vol. 30, no. 7, pp. 573-574, March 1994.
- [36] C.-H. Ho, L. Fan, and K. Chang, "New uniplanar coplanar waveguide hybrid-ring couplers and magic-T's," *IEEE Trans. Microw. Theory Tech.*, vol. 42, no. 12, pp. 2440-2448, Dec. 1994.
- [37] C.-Y. Chang, and C.-C. Yang, "A Novel Broad-Band Chebyshev-Response Rat-Race Ring Coupler," *IEEE Trans. Microw. Theory Tech.*, vol. 47, no. 4, pp. 445-462, April 1999.
- [38] T. T. Mo, Q. Xue, and C. H. Chan, "A broadband compact microstrip rat-race hybrid using a novel CPW inverter," *IEEE Trans. Microw. Theory Tech.*, vol. 55, no. 1, pp. 161-167, Jan. 2007.
- [39] J.H. Kim, D.W. Woo, G.Y. Jo, and W.S. Park, "Microstrip Phase Inverter using Slotted Ground," *IEEE Antenna and Propagation Society International Symposium(APSURS)*, pp.1-4, 2010.

- [40] M. K. Chirala, and B. A. Floyd, "Millimetre-wave lange and ring-hybrid couplers in a silicon technology for E-band applications," *IEEE MTT-S Microw. Symp. Dig.*, pp. 1547-1550, 2006.
- [41] M. C. Scardelletti, G. E. Ponchak, and T. M. Weller, "Miniaturized Wilkinson Power Dividers Utilizing Capacitive Loading," *IEEE Microw. Wireless Comp. Lett.*, vol. 12, no. 1, pp. 6-8, Jan. 2002.
- [42] J. Wu, E. Li, and G.-f. Guo, "Microstrip Power Divider with Capacitive Stubs Loading for Miniaturisation and Harmonic Suppression," *Microwave Technology Computational Electromagnetics (ICMTCE)*, 2011 IEEE International Conference on, pp. 237-239, 2011.
- [43] S.-C. Jung, R. Negra, and F. M. Ghannouchi, "A Design Methodology for Miniaturized 3-dB Branch-Line Hybrid Couplers Using Distributed Capacitors Printed in the Inner Area," *IEEE Trans. Microw. Theory Tech.*, vol. 56, no. 12, pp. 2950-2953, Dec. 2008.
- [44] J. Wang, B.-Z. Wang, Y.-X. Guo, L. C. Ong, and S. Xiao, "Compact slow-wave microstrip rat-race ring coupler," *Electron. Lett.*, vol. 43, no. 2, pp. 111-113, Jan. 2007.
- [45] J.-T. Kuo, J.-S. Wu, and Y.-C. Chiou, "Miniaturized rat race coupler with suppression of spurious passband," *IEEE Microw. Wireless Comp. Lett.*, vol. 17, no. 1, pp. 46-48, Jan. 2007.
- [46] H.-R. Ahn, and T. Itoh, "Compact Impedance-Transforming 3-dB Three-Port Power Dividers with Modified Asymmetric Impedance Transformers (MCCTs)," *IEEE MTT-S Microw. Symp. Dig.*, pp. 1-4, 2011.
- [47] H.-R. Ahn, and T. Itoh, "New Isolation Circuits of Compact Impedance-Transforming 3-dB Baluns for Theoretically Perfect Isolation and Matching," *IEEE Trans. Microw. Theory Tech.*, vol. 58, no. 12, pp. 3892-3902, Dec. 2010.
- [48] T. Hirota, A. Minakawa, and M. Muraguchi, "Reduced-size branch-line and rat-race hybrids for uniplanar MMIC's," *IEEE Trans. Microw. Theory Tech.*, vol 38, no. 3, pp.270-275, March 1990.
- [49] H. P. Hsu, "On The General Relation Between α and Q (Correspondence)," *IEEE Trans. Microw. Theory Tech.*, vol. 11, pp. 258-258, 1963.
- [50] A.-L. Franc, E. Pistono, G. Meunier, D. Gloria, and P. Ferrari, "A Lossy Circuit Model Based on Physical Interpretation for Integrated Shielded Slow-Wave CMOS Coplanar Waveguide Structures," *IEEE Trans. Microw. Theory Tech.*, vol. 61, no. 2, pp. 754-763, Feb. 2013.
- [51] A. L. Franc, E. Pistono, N. Corrao and P. Ferrari, "Compact high rejection notch and DBR designed with slow-wave transmission lines," *Proc. Asia-Pacific Microw. Conf.*, pp. 1146-1149, Dec. 2010.

- [52] X. Tang, E. Pistono, P. Ferrari, and J.-M. Fournier, "Enhanced Performance of 60-GHz Power Amplifier by using Slow-wave Transmission Lines in 40 nm CMOS Technology," *International Journal of Microwave & Wireless Technology*, vol. 4, pp. 93-100, Feb. 2012.
- [53] A.-L. Franc, E. Pistono, N. Corrao, D. Gloria, and P. Ferrari, "Compact high-Q, low-loss mmW transmission lines and power splitters in RF CMOS technology," *IEEE MTT-S Microw. Symp. Dig.*, pp. 1-4, June 2011.
- [54] C.-Y. Kuo, A. Y.-K. Chen, C. Li, and C.-H. Luo, "A mm-Wave Stub-Loaded ECPW Wilkinson Power Divider/Combiner in 90 nm CMOS," *IEEE Microw. Wireless Comp. Lett.*, vol. 22, no. 12, pp. 627-629, Nov. 2012.
- [55] W.-F. Liang, W. Hong, and J.-X. Chen, "A Q-Band Compact Wilkinson Power Divider Using Asymmetrical Shunt-Stub in 90nm CMOS Technology," *Proc. Asia-Pacific Microw. Conf.*, pp. 974-976, Dec. 2012.
- [56] H. Ding, K. Lam, E. Mina, J. Rascoe, D. Jordan, A. Zeeb, and B. Gaucher, "On-Chip Millimeter-Wave Library Device-Scalable Wilkinson Power Divider/Combiner," *Proc. Elect. Comp. and Tech. Conf. (ECTC)*, vol.56, pp. 1246-1251, June 2007.
- [57] K. Ma, S. Mou, Y. Lu, L. K. Meng, K. S. Yeo, "A 60GHz defected ground power divider using SiGe BiCMOS technology," *SoC Design Conference (ISOCC)*, pp. 1-4, 2011.
- [58] H. Ding, G. Wang, K. Lam, D. Jordan, A. Zeeb, A. Bavisi, E. Mina, and B. Gaucher, "Modeling and Implementation of On-Chip Millimeter-Wave Compact Branch Line Couplers in a BiCMOS Technology," *37th European Microwave Conference*, pp. 458-461, Oct. 2007.
- [59] I. Haroun, J. Wight, C. Plett, A. Fathy, and D.-C. Chang, "Experimental Analysis of a 60 GHz Compact EC-CPW Branch-Line Coupler for mm-Wave CMOS Radios," *IEEE Microw. Wireless Comp. Lett.*, vol. 20, no. 4, pp. 211-213, April 2010.
- [60] C.-Y. Kuo, A.Y.-K. Chen, C.-M. Lee and C.-H. Luo, "Miniature 60 GHz slow-wave CPW branch-line coupler using 90 nm digital CMOS process," *Electronics Letters*, vol. 47, no. 16, pp. 924-925, Aug. 2011.
- [61] H.-K. Chiou, and T.-Y. Yang, "Low-Loss and Broadband Asymmetric Broadside-Coupled Balun for Mixer Design in 0.18- μ m CMOS Technology," *IEEE Trans. Microw. Theory Tech.*, vol. 56, no. 4, pp. 835-848, April 2008.
- [62] C.-H. Liu, C.-Y. Hsu, H.-R. Chuang, and C.-Y. Chen, "A 60-GHz millimetre-wave CMOS Marchand balun using 0.18- μ m CMOS technology," *Microw. Opt. Technol. Lett.*, vol. 51, no. 3, pp. 766-770, Mar. 2009.

- [63] H. Ding, K. Lam, G. Wang, and W. H Woods, "On-chip Millimeter Wave Rat-race Hybrid and Marchand Balun in IBM 0.13um BiCMOS Technology," *Proc. Asia-Pacific Microw. Conf.*, pp. 1-4, 2008.
- [64] G. Felic and E. Skafidas, "An Integrated Transformer Balun for 60 GHz Silicon RF IC Design," *Int. Symp. on Signals, Systems and Electronics*, pp. 541-542, July 2007.
- [65] M. Tsai and A. Natarajan, "60 GHz passive and active RF-path phase shifters in silicon," *Proc. IEEE Radio Freq. Integr. Circuits Symp.*, pp. 223-226, 2009.
- [66] H.-T. Kim, J.-H. Park, J. Yim, Y.-K. Kim, and Y. Kwon, "A Compact V-Band 2-Bit Reflection-Type MEMS Phase Shifter," *IEEE Microw. Wireless Comp. Lett.*, vol. 12, no. 9, pp. 324-326, Sep. 2002.
- [67] S. Gong, H. Shen, and N. S. Barker, "A 60-GHz 2-bit Switched-Line Phase Shifter Using SP4T RF-MEMS Switches," *IEEE Trans. Microw. Theory Tech.*, vol. 59, no. 4, pp. 894-900, April 2011.
- [68] Y.-C. Chiang, W.-T. Li, J.-H. Tsai, T.-W. Huang, "A 60GHz Digitally Controlled 4-bit Phase Shifter with 6-ps Group Delay Deviation," *MTT-S Int. Microw. Symp. Dig.*, pp. 1-3, June 2012.
- [69] H.-T. Kim, J.-H. Park, S. Lee, S. Kim, J.-M. Kim, Y.-K. Kim, and Y. Kwon, "V -Band 2-b and 4-b Low-Loss and Low-Voltage Distributed MEMS Digital Phase Shifter Using Metal-Air-Metal Capacitors," *IEEE Trans. Microw. Theory Tech.*, vol. 50, no. 12, pp. 2918-2923, Dec. 2002.
- [70] Y. Yu, P. Baltus, A. van Roermund, D. Jeurissen, A. de Graauw, E. van der Heijden, R. Pijper, "A 60 GHz digitally controlled phase shifter in CMOS," *Proc. European Solid-State Circuits Conf. (ESSCIRC)*, pp. 250-253, 2008.
- [71] D. Kaddour, H. Issa, A.-L. Franc, N. Corrao, E. Pistono, F. Podevin, J.-M. Fournier, J.-M. Duchamp and P. Ferrari, "High-Q slow-wave coplanar transmission lines on 0.35 μm CMOS process," *IEEE Microw. Wireless Compon. Lett.*, vol. 19, no. 9, pp.542-544, Sep. 2009.
- [72] A. L. Franc, E. Pistono, D. Gloria, and P. Ferrari, "High-Performance Shielded Coplanar Waveguides for the Design of CMOS 60-GHz Bandpass Filters," *IEEE Trans. Electron Devices*, vol. 59, no. 5, pp. 1219-1226, May 2012.
- [73] X.-L. Tang, A.-L. Franc, E. Pistono, A. Siligaris, P. Vincent, P. Ferrari and J.-M. Fournier, "Performance improvement versus CPW and loss distribution analysis of slow-wave CPW in 65 nm HR-SOI CMOS technology," *IEEE Trans. Electron Devices*, vol. 59, no. 5, pp.1279 -1285, May 2012.

- [74] T. Quémerais, “Conception et étude de la fiabilité des amplificateurs de puissance fonctionnant aux fréquences millimétriques en technologies CMOS avancées,” Thesis at Université de Grenoble, Oct. 2010.
- [75] M. Mangan, S. P. Voinigescu, Y. Ming-Ta, and M. Tazlauanu, “De-embedding transmission line measurements for accurate modeling of IC designs,” *IEEE Trans. Electron Devices*, vol. 53, no. 2, pp. 235-241, Feb. 2006.
- [76] N. Seller, “Contribution à l’étude, au développement et à la réalisation d’oscillateurs à contrôle numérique en technologie silicium avancée,” Thesis at Université de Bordeaux, Dec. 2008.
- [77] K. J. Herrick and L. P. B. Katehi, “W-band micromachined circuit combining networks,” *IEEE Trans. Microw. Theory Tech.*, vol. 50, no. 6, pp. 1647–1651, Jun. 2002.
- [78] S. Horst, S. Bhattacharya, M. M. Tentzeris, and J. Papapolymerou, “Monolithic low cost Ka-band Wilkinson power dividers on flexible organic substrates,” *Electron. Compon. Technol. Conf.*, pp. 1851–1854, Jun. 2007.
- [79] C.-Y. Kuo, A. Y.-K. Chen, C. Li, and C.-H. Luo, “A mm-Wave Stub-Loaded ECPW Wilkinson Power Divider/Combiner in 90 nm CMOS,” *IEEE Microw. Wireless Components Letters*, vol. 22, no. 12, pp. 627–629, Dec. 2012.
- [80] S. Horst, R. Bairavasubramanian, M. M. Tentzeris and J. Papapolymerou, “Modified Wilkinson Power Dividers for Millimeter-Wave Integrated Circuits,” *IEEE Trans. Microw. Theory Tech.*, vol. 55, no. 11, pp. 2439-2446, Nov. 2007.
- [81] S. Okamura, X. Wang, K. Takahashi, M. Tahara, and I. Sakagami, “A General Model of Modified Wilkinson Power Dividers with Additional Transmission Lines,” *Proc.2011 IEEE European Microw. Conf. (EuMC)*, pp. 834-837, Oct. 2011.
- [82] H.-R. Ahn, “Modified Asymmetric Impedance Transformers (MCCTs and MCVTs) and Their Application to Impedance-Transforming Three-Port 3-dB Power Dividers,” *IEEE Trans. Microw. Theory Tech.*, vol. 59, no. 12, pp. 3312-3321, Dec. 2011.
- [83] Fano, R. M., “Theoretical limitations on the broadband matching of arbitrary impedances,” *J. Franklin Institution*, vol. 249, pp. 57–83, pp. 139–155, Jan./Feb. 1950.
- [84] K.-K. M. Cheng and W.-C. Ip, “A Novel Power Divider Design With Enhanced Spurious Suppression and Simple Structure,” *IEEE Trans. Microw. Theory Tech.*, vol. 58, no. 12, pp. 3903-3908, Dec. 2010.
- [85] M.G. Kim, J.S. Kim and R. Mittra, “Modified Wilkinson power divider for suppression of nth harmonics,” *Electronics Letters*, vol. 48, no. 24, Nov. 2012.
- [86] L. Yan, W. Hong, G. Hua, J. Chen, K. Wu, and T. J. Cui, “Simulation and Experiment on SIW Slot Array Antennas,” *IEEE Microw. Wireless Components Letters*, vol. 14, no. 9, pp. 446–448, Sep. 2004.

- [87] A. Niembro, E. Pistono, T.-P. Vuong, “SIW slot array antennas for a TollTag application at 5.8 GHz,” *Antenna Technology and Applied Electromagnetics (ANTEM), 15th International Symposium on*, pp. 1-3, June 2012.
- [88] D. Deslandes and K. Wu, “Integrated microstrip and rectangular waveguide in planar form,” *IEEE Microw. and Wireless Components Letters*, vol.11, no.2, pp.68-70, Feb. 2001.
- [89] J.-C. Wu, T.-Y. Chin, S.-F. Chang, and C.-C. Chang, “2.45-GHz CMOS Reflection-Type Phase-Shifter MMICs With Minimal Loss Variation Over Quadrants of Phase-Shift Range,” *IEEE Trans. Microw. Theory Tech.*, vol. 56, no. 10, pp. 2180–2189, Oct. 2008.
- [90] Y. Yu, P. Baltus, A. van Roermund, D. Jeurissen, A. de Graauw, E. van de Heijden and R. Pijper, “A 60 GHz digitally controlled phase shifter in CMOS,” *Proc. European Solid-State Circuits Conf. (ESSCIRC)*, pp.250-253, Sept. 2008.

Publications

- During PhD :

François Burdin, Florence Podevin, and Philippe Ferrari “Diviseur de puissance Flexible et Miniaturisé”, *18èmes Journée Nationales Microondes (18th French national conference on microwave)*, Paris, France, May 15-17, 2013. **Best student paper award.**

François Burdin, Zyad Iskandar, Florence Podevin, and Philippe Ferrari, “Conception d’un « Reflection Type Phase Shifter » à très fort Facteur de Mérite”, *18èmes Journée Nationales Microondes (18th French national conference on microwave)*, Paris, France, May 15-17, 2013.

Anne-Laure Franc, Florence Podevin, Emmanuel Pistono, Gustavo Rehder, Ariana Serrano, **François Burdin**, Xiaolan Tang, Jean-Michel Fournier, and Philippe Ferrari, “Slow-wave transmission lines for millimeter-wave integrated circuits: State-of-the-art and Prospects”, *Nanofunction ESSDERC/ESSCIRC Workshop on Novel Material Devices and Technologies for High Performance on-chip applications*, **invited paper**, Bordeaux, France, Sept. 9, 2012.

François Burdin, Florence Podevin, Benjamin Blampey, Nicolas Corrao, Emmanuel Pistono, and Philippe Ferrari, “Millimeter-wave Rat-race Balun in a CMOS 65nm Technology with Slow-wave Transmission Lines and Innovative Topology”, *PIERS Proceedings*, pp. 808-812, Moscow, Russia, Aug. 19-23, 2012.

François Burdin, Florence Podevin, Anne-Laure Franc, Emmanuel Pistono, Daniel Gloria, and Philippe Ferrari, “Miniaturized low-loss millimeter-wave rat-race balun in a CMOS 28 nm technology”, *Proc. of the IEEE MTT-S International Microwave Workshop Series on Millimeter Wave Integration Technologies*, pp. 73-76, Sitges, Spain, Sept. 15-16, 2011.

François Burdin, Zyad Iskandar, Florence Podevin, and Philippe Ferrari, “A 2.45 GHz high Figure-of-Merit Reflection Type Phase Shifter”, *accepted in PIERS Proceedings*, Stockholm, Sweden, Aug. 12-15, 2013.

François Burdin, Zyad Iskandar, Florence Podevin, and Philippe Ferrari, “Design of Simple Reflection Type Phase Shifters With High Figure-Of-Merit until 360°”, *submitted to IEEE Transactions Microwave Theory Techniques*.

François Burdin, Florence Podevin, and Philippe Ferrari, “Flexible and Miniaturized Power Divider”, *submitted to EuMA International Journal of Microwave and Wireless Technologies (IJMWT)*.

François Burdin, Florence Podevin, Nicolas Corrao, and Philippe Ferrari, “Compact Balun with phase inverter based on S-CPW in a 65 nm technology”, *submitted to IEEE Electron Device letters*.

▪ During three months internship at IMEP-LAHC :

Emmanuel Pistono, Hana Maouche, **François Burdin**, and Philippe Ferrari, “New topology of short-circuited quarter wavelength resonator filters”, *2009 International Workshop on Microwave Filters*, Toulouse, France, Nov. 16-18, 2009.

François Burdin, Emmanuel Pistono, and Philippe Ferrari, “Tunable compact filters based on stub-loaded parallel-coupled resonators”, *2010 Mediterranean Microwave Conference, invited paper*, pp. 110-113, Guzelyurt, Cyprus, Aug. 25-27, 2010.

François Burdin, Emmanuel Pistono, and Philippe Ferrari, “Parallel-coupled Stub-loaded Resonators Compact Size Tunable Filter”, *Asia-Pacific Microwave Conference Proceedings (APMC2010)*, pp. 147-150, Yokohama, Japan, Dec. 7-10, 2010.